Microstructure Evolution in Pearlitic Rail Steel due to Rail/Wheel Interaction

Jun WU

Microstructure Evolution in Pearlitic Rail Steel due to Rail/Wheel Interaction

Dissertation

for the purpose of obtaining the degree of doctor
at Delft University of Technology
by the authority of the Rector Magnificus prof. dr. ir. T.H.J.J. van der Hagen
chair of the Board for Doctorates
to be defended publicly on
Monday 17 December 2018 at10:00 o'clock

by

Jun WU

Master of Engineering, Shanghai University, Shanghai, China
born in Zhejiang, China

This dissertation has been approved by the

promotors: Prof. dr. ir. Jilt Sietsma and Prof. dr. ir. Roumen H Petrov

Composition of the doctoral committee:

Rector Magnificus	chairperson
Prof. dr .ir. J. Sietsma	Delft University of Technology, promotor
Prof. dr. ir. R. H. Petrov	Delft University of Technology, promotor
Independent members:	
Prof. dr. M. J. Santofimia Navarro	Delft University of Technology
Prof. dr. ir. H. De Backer	Ghent University
Prof. dr. ir. S. Hertelé	Ghent University
Dr. ir. R. H. Vegter	SKF, the Netherlands
Prof. dr. Z. Li	Delft University of Technology

The research described in this thesis was carried out in the Department of Materials Science and Engineering of the Delft University of Technology, the Netherlands.

This research was carried out under project number 11247 - C38A07, STW.

The doctoral research has been carried out in the context of an agreement on joint doctoral supervision between Ghent University, Belgium and Delft University of Technology, the Netherlands.

Keywords: white etching layer, brown etching layer, rail/wheel contact, frictional heat, martensite, retained austenite, laboratory simulation, phase field simulation,

ISBN 978-94-6366-114-0

An electronic version of this dissertation is available at

https://repository.tudelft.nl/.

Table of Content

Chapter 1 Introduction

1.1 Rolling contact fatigue in rails

Railway is no doubt the backbone land transportation form and plays a key role in the global society and economic development. The Union Internationale des Chemins de fer (in English is International Union of Railways, UIC) commented railway as with unparalleled potential for achieving a sustainable development for the twenty-first century [1,2]. Besides the unique capability and efficiency in handling large passenger/freight flow, railway is eco-friendly, economical, safe and traffic congestion free. Furthermore, railway has become an irreplaceable transportation form and has been contributing significantly to the national and global economies. For example, the report published in 2014 [3] claimed that the UK has been benefiting a yearly £ 9.3bn Gross Value Added (GVA) from railway transportation. In addition to the direct economic contribution, the rail transport development has an indirect impact on the society and environment, e.g. increasing employment in rail supply chain industries and less CO_2 emission in comparison with other land transport means.

The steel rail track is the critical component of the railway system and it is the direct carrier and the bearer of the loads from the running trains. The degradation of steel rail track is the main source for the railway maintenance and rail track replacement [4]. The interim rail track maintenance, especially when unexpectedly, may cause undesirable traffic interruptions and such maintenance is typically costly. Durable and maintainable rail tracks will thus be crucial in ensuring the sustainability of the rail infrastructure and the railway system.

The dominant damage form in the rails is the rolling contact fatigue (RCF) [4–6], the removal of which accounts for the majority of the rail track maintenance plans. The high loads from the trains and the tractive/braking force lead to plastic deformation in the rail surface [5,7]. Plastic strain accumulates during the subsequent wheel passages and cracks will consequently form. The cracks tend to propagate further toward the rail center and can lead to the catastrophic rail cross-section fracture, if not removed by maintenance work in time [5,7].

The dominance of plastic deformation in RCF formation can become secondary upon the presence of a superficial microstructure alternation in rail steels, classically named as white etching layer (WEL) [5,8–11]. WEL is typically 2 – 3 times harder, e.g. up to 1100 HV, than the matrix pearlitic microstructure in the rail steels, typically in the range of 220 HV – 440 HV in literature. As a result, WEL is considered to be brittle. Laboratory twin-disc tests show that premature RCF initiates due to the fracture of WEL and cracks which formed in the pearlite area adjacent to WEL [12]. The subsequent Finite Element Method (FEM) simulation [13] reveals that RCF cracks form in the pearlite near the WEL is due to more extensive plastic strain accumulation in pearlite during the loading.

The root causes for the WEL formation are usually proposed from the microstructure characterizations while a comprehensive hypothesis fails to be reached. A main controversy among the proposed hypotheses is regarding how the cementite can be dissolved during the WEL formation since the cementite in the initial pearlitic microstructure is not observed in WEL [9,11]. It is well known that the equilibrium carbon concentration in cementite is 6.7 wt% and is much higher than the carbon solubility in ferrite, e.g. maximum 0.025 wt% at 727 °C in Fe-C system. As a result, trapping sites for the amount of carbon from the dissolved cementite need to be provided and interpreted in the proposed hypotheses for WEL formation.

One of the most widely accepted hypotheses is that the WEL consists of martensite because the rail surface is so significantly heated that the pearlite to austenite transformation occurs during the wheel/rail contact. The ultrafast quenching after wheel passages enables austenite to transform to martensite. This hypothesis can be supported by the recognition of lattice tetragonality from a body-centered cubic (BCC) crystal structure and the identification of retained austenite from synchrotron XRD measurements [14,15]; the nano-twinning martensitic substructures recognized by TEM [11,14]. More importantly, identification of manganese diffusion in the WEL [11], compared with the manganese distribution in the bulk pearlite, is a convincing validation of significant temperature increases. It is well known that long distance manganese diffusion typically requires a high temperature, e.g. above 800 °C. Such high temperature is well above the eutectoid point for the given rail steel compositions, enabling fully transformation of the initial pearlitic microstructure to austenite.

The other major hypothesis for WEL formation is the significant grain refinement due to severe plastic deformation from the train wheels. TEM works of Baumann [8] and Lojkowski et al. [16] identify WEL as a structure consisting of nanocrystalline ferrite and without the presence of cementite. The grain size in the WEL is measured to be less than 50 nm. Frictional temperature increase calculation by Baumann

[8] shows that the temperature increase up to austenitizing temperature under the loading condition of the characterized rail steel is impossible. Combined with the observation of deformation characteristics in the pearlite zones beneath the WEL, Baumann [8] proposed that the WEL forms via the severe plastic deformation. The carbon from the dissolved cementite is argued to be accommodated by the high-density dislocations formed during the train loading. It is reported that carbon has a higher binding energy with dislocations in ferrite, 0.75 – 0.78 eV, than the binding energy of carbon in cementite, about 0.5 eV, e.g. in [17]. As cited in [18], a dislocation density of 5×10^{12} - 10^{13} m^{-2} can accommodate a maximum carbon concentration of 4.5 at% and a similar dislocation density is quantified in WEL [14]. Furthermore, the severe plastic deformation will cause significant grain refinement, which can provide extra grain boundary areas to accommodate the carbon from the dissolved cementite.

It can be seen that the origin of WEL formation depends on and can vary significantly with different loading conditions of the rail steels. Microstructure characterizations on the WEL are crucial for exploring its root cause. Based on the understanding from the microstructure study, it will be possible to simulate and consequently predict the formation of WEL. An insight for designing more WEL-resistant rail steels may be subsequently obtained.

1.2 This thesis

The aim of the thesis is to achieve a sound understanding of the WEL formation in the Dutch rail steels and to provide insight into the design of more WEL-resistant steels. WEL has been widely observed in the Dutch rail steels and metallurgy studies frequently report RCF crack initiation at the WEL [10,19,20]. Due to the very fine microstructures in the WEL, advanced characterization techniques are required to identify the microstructures in the WEL. The laboratory and theoretical simulations of WEL formation process, under known conditions, are able to provide supporting evidence and insight into the characteristics during WEL formation.

The content of the thesis is arranged as follows:

Chapter 2 gives a literature overview on the microstructural causes for the rolling contact fatigue (RCF) damage in rail steels. A general introduction of microstructure control of steels for railway application is first given and their performance in rail track and in laboratory tests are discussed. A subsequent discussion of the detrimental effects, due to the presence of the so-called ‘weak sites’, on the RCF performance of rail steels is further provided. The important role of so-called white etching layer (WEL) is specifically stressed.

Chapter 3 describes the microstructures in an R260 Mn grade rail steel, showing surface damage after service, in addition to the principles and configurations of different techniques used for the experimental research presented in this thesis: microhardness; optical and scanning electron microscopy (OM and SEM); X-ray diffraction (XRD), electron backscatter diffraction (EBSD) and transmission Kikuchi

diffraction (TKD) in SEM; transmission electron microscopy (TEM); Atom Probe Tomography (APT). A thermo-mechanical simulator, for simulating the WEL phenomenon, is also introduced in the chapter.

Chapter 4 presents a characterization work on the microstructures in the white etching layer (WEL) observed in an R260 Mn grade rail steel, from micrometer to nanometer scales. Retained austenite in WEL is identified by electron backscatter diffraction (EBSD), transmission Kikuchi diffraction (TKD) and X-ray diffraction (XRD). EBSD and TKD quantify grains in the WEL with a size range of the order of magnitude of 10^{-8} – 10^{-5} m. Transmission electron microscopy (TEM) identifies complex heterogeneous microstructure morphologies in the WEL: nano-twinning substructure with high dislocation density in WEL close to rail surface and untransformed cementite and dislocations in WEL close to the pearlite matrix. The study with atom probe tomography (APT) shows heterogeneous elemental distributions through the WEL thickness. Accordingly, WEL is considered to be martensite with gradually changing microstructure. The experimental findings are well supported by the temperature calculation from the shape analysis of the manganese profile from APT measurements. The deformation characteristics in WEL and the pearlite beneath are discussed based on the EBSD and TKD measurements. The WEL is consequently proposed to form via combined consequence of temperature increase and plastic deformation.

In ***Chapter 5,*** WEL formation by martensitic transformation in R260Mn grade pearlitic rail steel was simulated by fast heating and quenching experiments. Simultaneous deformation and fast heating were performed in some of the tests to study the role of plastic deformation on the martensite formation. Microstructural characteristics of the simulated WEL and WEL observed in a field rail specimen are characterized by microhardness measurements, optical microscopy, scanning electron microscopy and electron backscatter diffraction. Microstructures of the two WELs are compared and similarities in morphology are identified. Plastic deformation is found to promote the formation of martensite in the simulated WEL, by comparing the fraction of martensite in the tests with and without deformation at the same temperature. Numerical simulation shows the possible temperature rise up to austenitizing temperatures. Combining comparisons of experimental simulation with the observation of WEL in the rail and the thermodynamic calculations, the hypothesis for WEL formation via martensitic transformation is supported.

In ***Chapter 6*** the pearlite – austenite transformation during (ultra-)fast heating is simulated by the multi-phase-field approach, in order to study the white etching layer formation (WEL) in rail steels. The ferrite and cementite lamellae in the pearlite microstructure are individually resolved and artificial martensite is introduced to represent the conditions when austenite already forms in the previous wheel passage. The insight into the WEL formation is obtained by studying the pearlite to austenite transformation with heating rates of 10 °C/s and 2000 °C/s. It is indicated that pearlite to austenite transformation during continuous heating is the mixed mode of diffusion-controlled and interface-controlled characteristics. An increased heating rate from 10 °C/s to 2000 °C/s shifts the austenite formation towards the interface-

controlled characteristics. The carbon concentration and the corresponding mechanical property of martensite in a single WEL block can be significantly different and depend on the loading condition.

Finally, in ***Chapter 7***, another type of WEL, named as brown etching layer (BEL) [20], was characterized by microhardness, optical microscopy (OM), scanning electron microscopy (SEM), and electron backscatter diffraction (EBSD). The BEL is named after its brownish color observed in the optical microscope after etching with 2-4%Nital. The observed BEL exhibits most of the morphological features as the classical WEL and is identified as another possible important source for RCF initiation. Moreover, cracks associated with BEL are found to grow considerably deeper towards the rail depth, comparing with the cracks caused by the WEL that mostly propagate at a limited depth only or cause spalling [12,21]. These results indicate the possibly more detrimental role of BEL in the RCF development in rails than WEL. Consequently, more extensive rail grinding is needed to completely remove the cracks caused by BEL, leading to possible premature rail removals and more frequent new rail replacements. Therefore, the study of the formation mechanism of the BEL is of practical concern and importance.

The characterized BEL is compared with WEL reported in the literature and also WEL studied in the current thesis. The following conclusions can be drawn: *(i)* BEL consists of white and brown sublayers with distinctly different mechanical properties; *(ii)* BEL forms via combined martensite phase transformation and plastic deformation; *(iii)* The white sublayer is proposed as martensite and the brown sublayer is the tempered martensite due to temperature rise below the austenite transformation temperature.

References

[1] UIC, 2014. A global vision for railway development, available at https://uic.org/IMG/pdf/global_vision_for_railway_development.pdf, accessed in October 2016.

[2] UIC, 2013, Challenge 2050 - the Rail Sector Vision, available at http://www.cer.be/publications/charters-and-agreements/challenge-2050-rail-sector-vision, accessed in October 2016.

[3] Oxera, 2015, What is the contribution of rail to the UK economy? available at https://www.oxera.com/getmedia/802a4979-8371-4063-ad24-8a81ed6c8f82/Contribution-of-rail-to-the-UK-economy-140714.pdf.aspx?ext=.pdf accessed in October 2016.

[4] Ekberg A, Paulsson B, 2010, Concluding technical report – Innotrack, available at http://publications.lib.chalmers.se/records/fulltext/129645/local_129645.pdf, accessed in October 2015.

[5] Daniel W, Kerr M, Daniel AW, 2013, Final Report on the Rail Squat Project R3-105, available at http://www.railcrc.net.au/object/PDF/get/download/id/r3105_final_report_updated, accessed August 2015.

[6] Magel EE, 2011, Rolling Contact Fatigue: A Comprehensive Review, available at https://nparc.nrc-cnrc.gc.ca/eng/view/fulltext/?id=2629e321-fe89-4eda-8531-662d35dbca8a, accessed in August 2015.

[7] Li, Z. 13 - Squats on railway rails BT - Wheel–Rail Interface Handbook. Woodhead Publishing, 2009: 409–436.

[8] Baumann G, Fecht HJJ, Liebelt S. Formation of white-etching layers on rail treads. Wear 1996;191:133–40.

[9] Lojkowski W, Millman Y, Chugunova SI, Goncharova I V., Djahanbakhsh M, Bürkle G, et al. The mechanical properties of the nanocrystalline layer on the surface of railway tracks. Mater Sci Eng A 2001;303:209–15.

[10] Wu J, Petrov RH, Naeimi M, Li Z, Dollevoet R, Sietsma J. Laboratory simulation of martensite formation of white etching layer in rail steel. Int J Fatigue 2016;91:11–20.

[11] Takahashi J, Kawakami K, Ueda M. Atom probe tomography analysis of the white etching layer in a rail track surface. Acta Mater 2010;58:3602–12.

[12] Carroll RI, Beynon JH. Rolling contact fatigue of white etching layer: Part 1. Crack morphology. Wear 2007;262:1253–66.

[13] Carroll RI, Beynon JH. Rolling contact fatigue of white etching layer: Part 2. Numerical results. Wear 2007;262:1267–73.

[14] Österle Rooch, H., Pyzalla, A., Wang, L. W, Investigation of white etching layers on rails by optical microscopy, electron microscopy, X-ray and synchrotron X-ray diffraction. Mater Sci Eng A 2001;303:150–7.

[15] Wang Pyzalla, A., Stadlbauer, W., Werner, E. A. L, Wang L, Pyzalla A, Stadlbauer W, Werner EA. Microstructure features on rolling surfaces of railway rails subjected to heavy loading. Mater Sci

Eng A 2003;359:31–43.

[16] Lojkowski W, Djahanbakhsh M, Bürkle G, Gierlotka S, Zielinski W, Fecht HJ. Nanostructure formation on the surface of railway tracks. Mater Sci Eng A 2001;303:197–208.

[17] Buono VTL, Gonzalez BM, Andrade MS. Kinetics of strain aging in drawn pearlitic steels. Metall Mater Trans A 1998;29:1415–23.

[18] Zhang HW, Ohsaki S, Mitao S, Ohnuma M, Hono K. Microstructural investigation of white etching layer on pearlite steel rail. Mater Sci Eng A 2006;421:191–9.

[19] Steenbergen M, Dollevoet R. On the mechanism of squat formation on train rails – Part I: Origination. Int J Fatigue 2013;47:361–72.

[20] Li S, Wu J, Petrov RH, Li Z, Dollevoet R, Sietsma J. "Brown etching layer": A possible new insight into the crack initiation of rolling contact fatigue in rail steels? Eng Fail Anal 2016;66:8–18.

[21] Clayton P, Allery MBP. Metallurgical Aspects of Surface Damage Problems in Rails. Can Metall Q 1982;21:31–46.

Chapter 2 Microstructural damage in rails: a literature review

Abstract:
This chapter addresses a literature overview on the microstructural causes for the rolling contact fatigue (RCF) damage in rail steels. A general introduction of microstructure control of steels for railway application is first given and their performance in rail track and in laboratory tests are discussed. A subsequent discussion of the detrimental effects, due to the presence of the so-called 'weak sites', on the RCF performance of rail steels is further provided. The important role of white etching layer is specifically stressed.

2.1 Introduction

The rolling contact fatigue (RCF) damage in rail steels is significantly affected by the loading conditions, imposed by the running trains. The passing trains exert complicated and dynamic stresses on the underneath rails and RCF cracks will occur at sites where suffer maximum stresses, e.g. [1,2]. The RCF crack initiation and propagation are, meanwhile, determined by the microstructures in the rail steel and the corresponding mechanical properties [3–7]. It is specifically pointed out that microstructure study is essential in understanding the root cause of RCF and the subsequent design of more RCF-resistant rail steels [8,9].

There are mainly three types of microstructures used in the rail steels: pearlite [5,7,8,10–14], austenite [13,19–21] and bainite [5,7,8,10–18]. The pearlite consisting of alternating ferrite and cementite lamellae, Fig. 2.1(a), is the microstructure in the rail steels covering the major rail track network. The combination of soft ferrite and hard cementite ensures the good combination of wear and fatigue performance of the rails. Steels with an austenite microstructure are used in steels for railway switches and crossings, Fig. 2.1(b), and is mainly referred to as the Hadfield high manganese steel [13,19–25]. This type of steel has an excellent combination of wear resistance, rapid work hardening, high ductility and good weldability [13,19,21,26]. More recently, a 'carbide-free' bainite microstructure has been shown to be a promising alternative to the pearlite and austenite steels [27]. The carbide-free bainite typically consists of nanometer-sized ferrite laths, Fig. 2.1(c), contributing to a tensile strength of 1320 – 2500 MPa [18,28–30]. In addition, the fracture toughness of the carbide-free bainite, 150 $MPam^{1/2}$, is also much higher than that of pearlite, which barely exceeds 95 $MPam^{1/2}$ [31]. The concept of alloy design of the carbide-free bainite will be not illustrated here and can be referred to e.g. [17,28,32,33].

Besides the promising development of new steels for railway applications, the current understanding of RCF damage in pearlitic rails remains insufficient [8,9]. The subsequent improvements in predicting the RCF damage evolution in rails will be essential to optimize the rail track maintenance plans. Such progress requires an exploration into the damage mechanisms in the microstructure aspect. The literature review in this chapter will focus on the pearlite microstructure in the rail steels and its related damage characteristics. A review of the microstructure control for producing the pearlite microstructure for rails will be first given. The subsequent sections explain the RCF damage evolution in this type of rail steel and the negative role of the microstructural 'weak sites' in the rail steels will be illustrated.

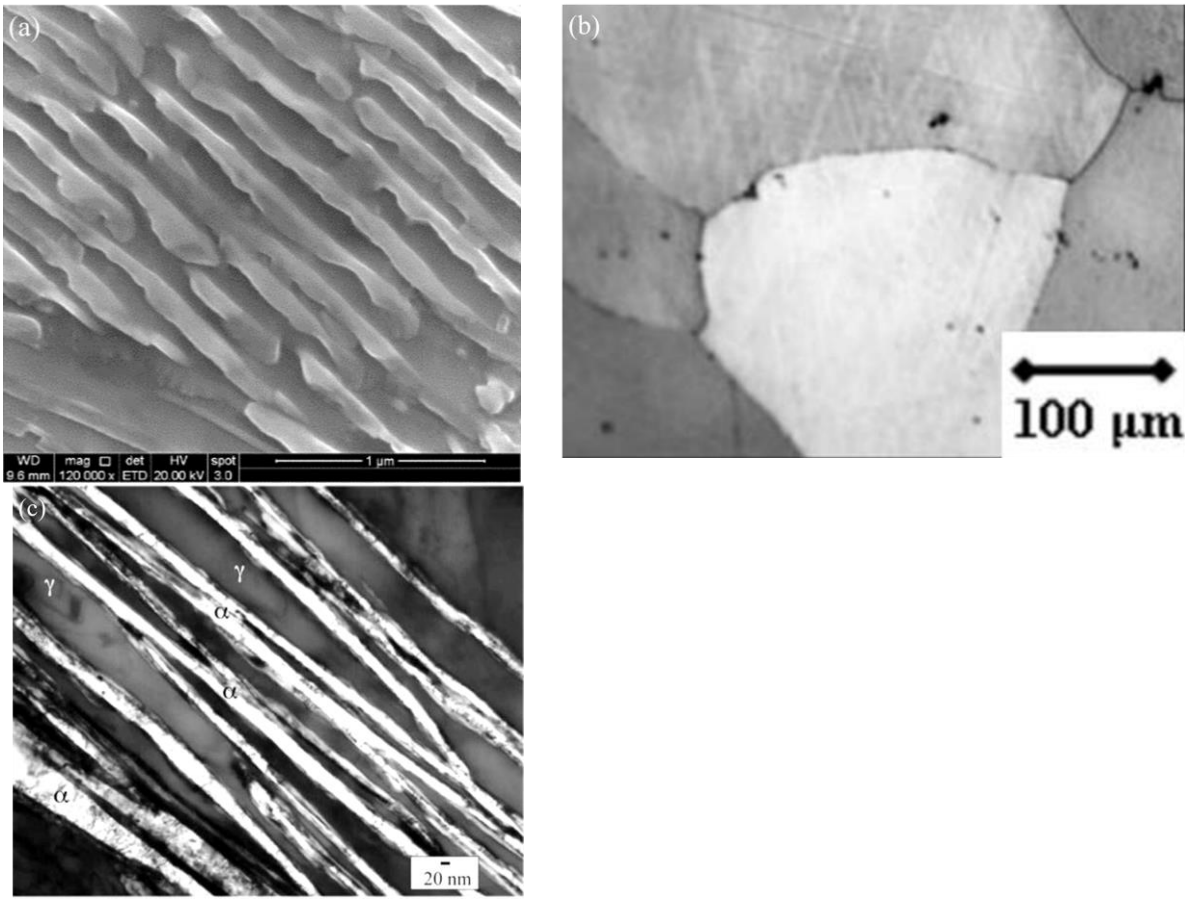

Fig. 2.1: (a) An SE-SEM image of a full pearlite microstructure in a Dutch R260Mn grade rail steel from this thesis work; (b) an optical micrograph of high manganese austenite steel from [25];(c) TEM micrograph of a carbide-free bainite in [17]. γ refers to retained austenite and α is ferrite.

2.2 Pearlite in rail steels

A general overview of pearlite microstructure formation can be explained by the equilibrium iron-carbon phase diagram in Fig. 2.2, calculated by the Thermo – Calc® software package [34]. The carbon concentration at the vertical dotted line in the same figure is randomly chosen for illustration purpose. According to Fig. 2.2, there are three stages for the phase transformations for the selected carbon concentration within the plotted temperature range: (1) At temperatures higher than the A_3, the steel has a fully austenitic microstructure, γ; (2) Austenite (γ) transforms to ferrite (α) between A_1 and A_3. The Gibbs free energy of the α phase (G^{α}) is lower than that of the γ (G^{γ}), providing a driving force for the phase transformation to occur. The ferrite forms at the austenite grain boundaries, classically named as pro-eutectoid (PE) ferrite. The changes of the fractions of austenite and ferrite can be estimated by the lever rule, e.g. in [35]; (3) When the temperature reaches A_1, namely the eutectoid temperature, the simultaneous eutectoid decomposition of $\gamma \rightarrow \alpha + \theta$ occurs, in which θ is the cementite phase. The mixed pearlite and PE ferrite microstructure will remain at temperatures below the A_1 temperature, since no

other equilibrium phase transformations will occur. For steels with a eutectoid carbon concentration, the PE ferrite is not expected. The schematic drawings in Fig. 2.2 illustrate the microstructure evolution together with temperature changes along the dotted line.

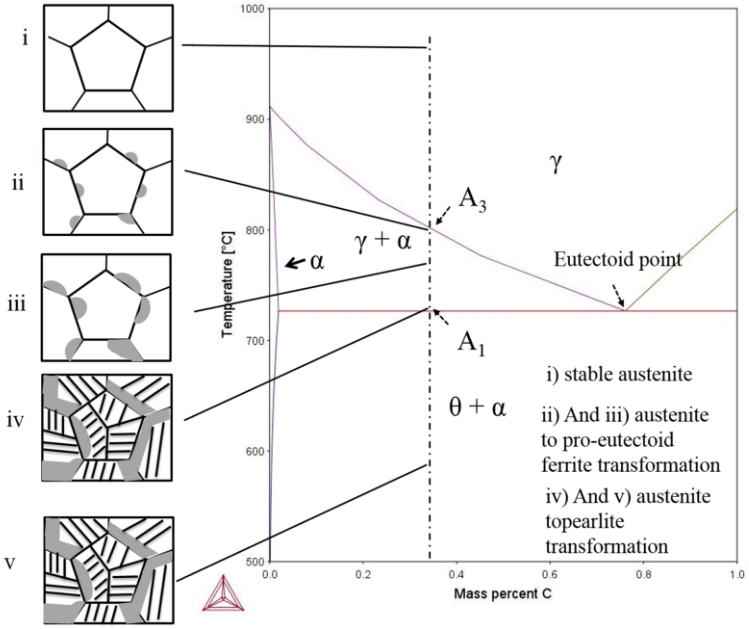

Fig. 2.2: Equilibrium iron-carbon phase diagram simulated by Thermo-Calc [34]

Table 2.1 is a reproduced table of the compositional ranges and the mechanical properties of the rail steels in the European Norm En13674 -1, 2011 [36]. It can be seen that carbon, manganese and silicon are the major alloying elements in the steels. The carbon varies from 0.38 wt% in the low R220 grade to 1.07 wt% for the high R400 HT grade. The additions of silicon and manganese are beneficial for strengthening the pearlite microstructure and also for refining the pearlite cementite spacing [12,37]. The impurity elements, such as sulfur and phosphor, are minimized, to ensure the optimal mechanical properties. The 'HT' and 'LHT' refer to heat treated and low alloy heat treated respectively, which requires a controlled cooling procedure to produce the refined microstructure [36]. It is worthwhile mentioning that steel grades R370 CrHT and R400 HT are newly added in the norm in [36], indicating the composition design trend of the pearlitic rail steels.

The strength of the pearlite steel is mainly determined by the cementite interlamellar distance, *d*, which is a measure of the distance between adjacent cementite lamellae. A Hall-Petch equation is frequently used to predict the yield strength from the interlamellar distance [38]:

$$\sigma = \sigma_0 + kd^{-0.5} \qquad (2.1)$$

in which σ is the yield strength of the pearlitic steel, and σ_0 and k are constants.

Taleff et al. [39] identify the complementary contributions of solid solution strengthening by alloying elements and pearlite colony size to the total strength of the pearlite steel, besides d. A modified equation from equation (2.1) is proposed as:

$$\sigma = (\sigma_0)_{ss} + 460{d_p}^{-0.5} + 145(\sqrt{2}d)^{-0.5} \qquad (2.2)$$

The subscript *ss* refers to the contribution of solid solution hardening; the term d_p is the pearlite colony size and d is again the cementite interlamellar distance. The $\sqrt{2}d$ term is introduced to account for the average distance between cementite spheroidites. The unit of the included microstructural features in equation (2.1) and (2.2) is μm and the unit for the strength is MPa.

Table 2.1 The chemical compositions of different rail grades, reproduced from [36]

Steel grade	in mass %							min Rm, MPa	min elongation %	Centerline running surface hardness, HV
	C	Si	Mn	Cr	P max	S max	V max			
R200	0.38/0.62	0.13/0.60	0.65/1.25	0.15 max	0.04	0.04	0.03	680	14	200/240
R220	0.50/0.60	0.20/0.60	1.00/1.25	0.15 max	0.025	0.03	0.03	770	12	220/260
R260	0.53/0.82	0.13/0.62	0.65/1.75	0.15 max	0.03	0.03	0.03	880	10	260/300
R260 Mn	0.53/0.77	0.13/0.62	1.25/1.75	0.15 max	0.03	0.03	0.03	880	10	260/300
R320 Cr	0.58/0.82	0.48/1.12	0.75/1.25	0.75/1.25	0.025	0.03	0.20	1080	9	320/360
350 HT	0.70/0.82	0.13/0.60	0.65/1.25	0.15 max	0.025	0.03	0.03	1175	9	350/390
R350 LHT	0.70/0.82	0.13/0.60	0.65/1.25	0.30 max	0.025	0.03	0.03	1175	9	350/390
R370 CrHT	0.68/0.84	0.38/1.02	0.65/1.15	0.35/0.65	0.025	0.025	0.03	1280	9	370/410
R400 HT	0.88/1.07	0.18/0.62	0.95/1.35	0.3 max	0.025	0.025	0.03	1280	9	400/440

2.3 RCF damage in pearlite rail steels

The rail steel fails due to repeated alternating stresses from the running trains. The response of the rail steels to the load from passing train wheels can be illustrated in Fig. 2.3 [40]. When the local load is lower than the yield strength of the rail steel, no plastic strain will occur in the material. Plastic material flow will start and the steel is strain-hardened when stress exceeds the yield strength. Meanwhile, a protective residual stress is generated. The combined work hardening and the residual stress can suppress the further plastic material flow and the rail materials will behave alike elastically during the subsequent cycles. These processes are called the elastic shakedown. A further increase in stress to above the elastic shakedown limit can cause repeated cyclic plastic strain during each wheel rolling, leading to the forming of the so-called plastic shakedown. When the stress exceeds the plastic shakedown limit, plastic strain continues to increase and the so-called ratchetting occurs, causing a net change of plastic strain after each wheel passage. The local rail material will fail when its plasticity

exhausts, leading to the formation of RCF defects in the rail surface. The plastic shakedown and ratcheting are the two common responses in the rail steels [40].

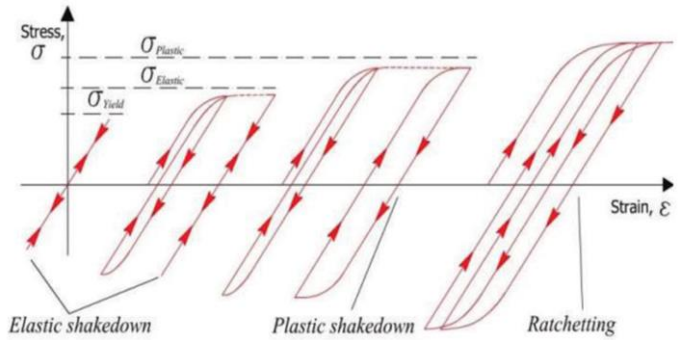

Fig. 2.3: The principal material response to the external cyclic loadings in rail steels [40]

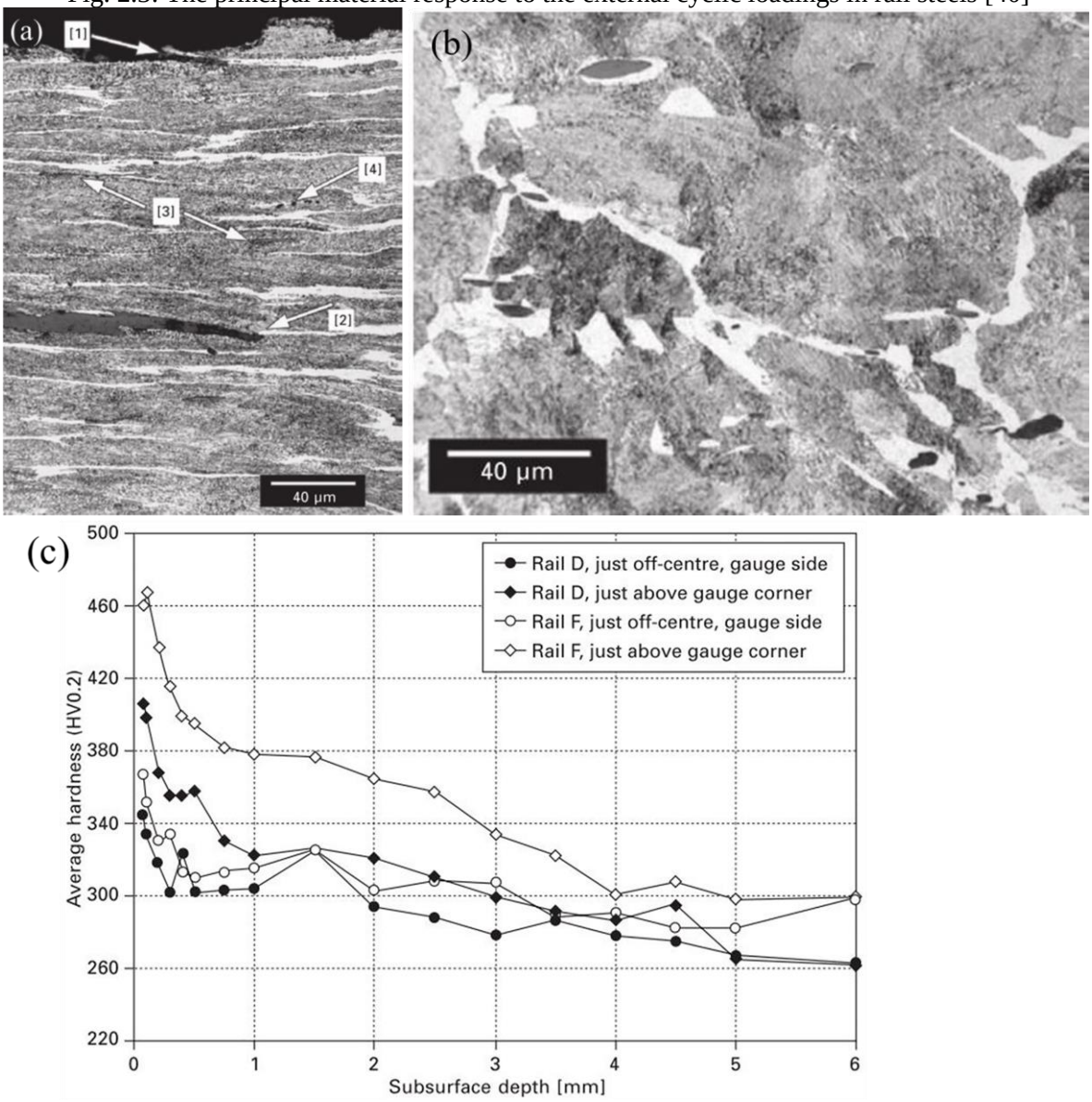

Fig. 2.4: Optical micrographs of microstructure on the surface (a) and the rail core (b) in the cross-section of a loaded rail piece[10]. The hardness measurements in (c) reveal work-hardening in the surface region. The "steel D" and "steel F" is equivalent to the R200 and R260 grade rail steels in the Table. 2.1 respectively.

The loads from the train wheels have their consequence on the microstructure in the underneath rail steels. Figs. 2.4(a) and (b) show the optical micrographs of the cross-sections of a loaded rail piece, at rail surface and rail center respectively [10]. The studied rail steel is a British BS11 grade with a carbon concentration of 0.4/0.5 wt%. As a result, grain boundary ferrite is expected according to Fig. 2.2 and can be well identified by the light/white appearance in the optical micrographs in Figs. 2.4(a) and (b). By comparing the two regions, it can be seen that the rail surface has been plastically deformed and the grain in the region become flattened. The hardness measurements in Fig. 2.4(c) identify an increased hardness in the surface region due to work hardening. Cracks eventually form in the surface zones.
The formation of RCF damage will be facilitated if the below undesirable microstructural 'weak sites' present in the rail steel, compared with the RCF formed in steels with a fully pearlitic microstructure. These 'weak sites' assist crack formation in the pearlite steel, leading to premature crack initiation.

2.4 The microstructural 'weak sites' in rail steels

2.4.1 Pro-eutectoid ferrite

Pro-eutectoid (PE) ferrite presents in steels with carbon concentration less than the eutectoid point in Fig. 2.2, and is usually used in rail steels for less severely loaded tracks, e.g. for trams. A close correlation between RCF cracks and PE ferrite is revealed in the metallographic studies on a field loaded rail pieces by Eden et al. [41]. The nanoindentation measurements identify up to 33% increased hardness in PE ferrite while the hardness increase in the adjacent pearlite is less than 8% when compared to the original material. This indicates that the PE ferrite is more extensively deformed and consequently accumulates more strain during the train passages. Accordingly, premature cracks can form in the PE ferrite. A supportive twin-disc test was done on a BS11 grade rail steel [42], in which specimens corresponding to different RCF development stages were characterized. Again, they confirm the crack initiation at PE and indicate an improved RCF lifetime in the specimen with less FE.

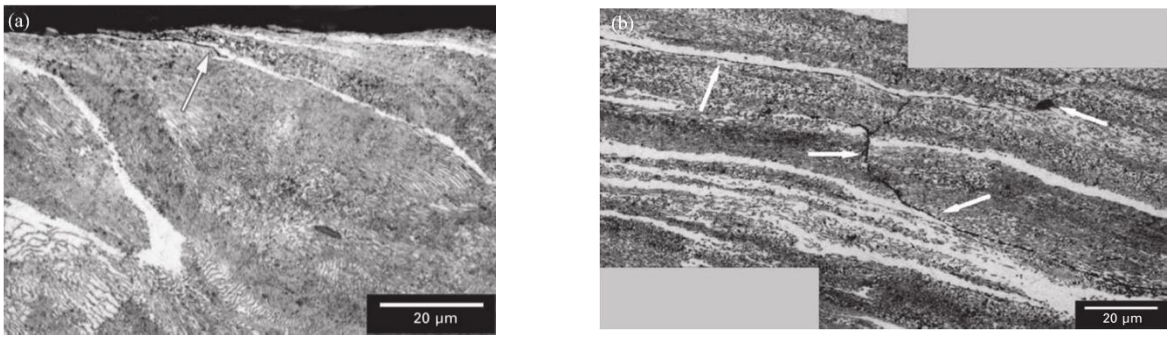

Fig. 2.5: (a) Crack initiation in a pro-eutectoid ferrite, as indicated by the white arrow; (b) cracks jumping between the subsurface cracks, formed in the pro-eutectoid ferrite [10]

2.4.2 Intermetallic inclusions

The detrimental effect of intermetallic inclusions on the fatigue behavior of engineering components has been well-recognized, see e.g. [43–46]. The intermetallic inclusions form during solidification and are

very difficult to be completely excluded during the casting. The inclusions have a significant difference in the thermal expansion coefficient with the steel matrix, and the intermetallic inclusions do not have a coherent connection with steel matrix. The incoherent boundary can hinder the dislocation movement during deformation, causing stress concentration. As loading continues, the inclusions or the inclusion/matrix boundaries will break and cavities form, which further leads to an earlier fatigue crack initiation. In some cases, the bearing components, for example [47,48] the brittle aluminum oxide (Al_2O_3 type), can even cause a structural change in the surrounding matrix, being typically 30 – 50 % harder than the matrix. The structure change is considered to embrittle the material and its premature fracture can cause surface flaking.

2.4.3 White etching layer (WEL)

White etching layer (WEL) is the most mysterious phenomenon in rail surface, comparing with the above discussed PE ferrite and intermetallic inclusions. The latter two can be well expected from the steel chemistry while WEL forms only during rail service time. The detrimental role of WEL will become more important if the PE and intermetallic inclusions are eliminated/minimized, via the metallurgical route. Furthermore, there are no clear correlations of WEL to any steel chemical compositions, i.e. with a ferrite-pearlite [49] or a fully lamellar pearlitic microstructure [50–52], nor to track sites, e.g. normal rail tracks or underground rails [53]. In short, WEL is a common observation in all pearlitic rails.

WEL causes premature RCF damage initiation. WEL can be well recognized by to its white color appearance under the optical microscope, Figs. 2.6(a) – (c), or gray color appearance under SEM, Fig. 2.6(d), after etching by 2 – 10 % Nital (solution of Nitric acid in ethanol) [11,49–51,54–56]. The Vickers hardness measurements typically reveal a hardness of 650 HV – 1200 HV in WEL, which corresponds to two to three times the hardness of the matrix pearlite (typical hardness of pearlite is between 220 – 440 HV). Cracks associating with WEL are frequently observed in loaded rail pieces. In addition, cracks can occur in the pearlite zones near the WEL, e.g. in Fig. 2.6(c) from the current study and Ref [57]. The simulations in [58,59] show shortened crack initiation time in rail steels when WEL is present, compared with the ones without WEL. Due to fact that WEL forms at the very early stage of the rail lifetime, the RCF damage initiation can be consequently facilitated due to the presence and the fracture of WEL. The worldwide observations of crack initiation by WEL [60–63] indicate that WEL is a universal issue.

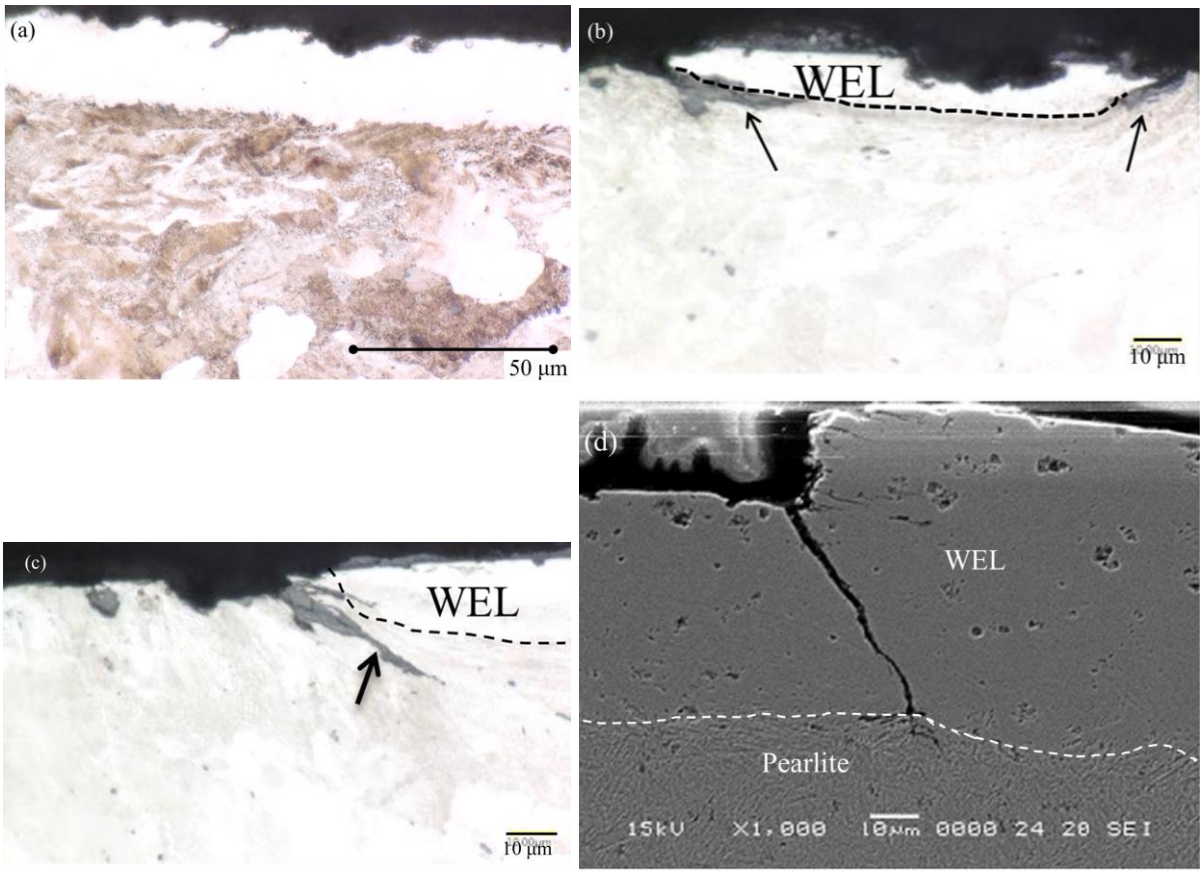

Fig. 2.6: Optical micrograph of (a) a WEL observed in a Dutch R260 Mn grade rail steel; (b) RCF crack initiation at the WEL/base boundary; (c) RCF crack initiation in the pearlite adjacent to the WEL; (d) a SEM image of RCF crack formed inside WEL from [58].

Extensive characterization studies on WEL have been done, in order to trace its origin [8,51,55,64–68]. Generally, two formation mechanisms are assumed possible for WEL: *(i)* severe plastic deformation leading to strain-induced cementite dissolution and grain refinement, e.g. nanocrystalline ferrite with carbon supersaturation [69] and *(ii)* high-temperature increase and subsequent fast cooling causing a martensitic phase transformation.

The first hypothesis for the WEL formation is related to severe plastic deformation of the pearlite. TEM results of Newcomb and Stobbs [49] show that WEL is a severely deformed ferrite, in which cementite is absent. Their transient temperature calculation indicates that the high temperature needed for austenite formation and subsequent martensite transformation to occur cannot be reached, from the loading history of the studied rail piece. They propose the WEL formation in analogy to mechanical alloying that is well known as a low-temperature process [70]. Based on investigations of the microstructure of the WEL using TEM and X-ray diffraction and on discussions of the nanostructure formation mechanism, Lojkowski et al. [56] conclude that the WEL is a nanocrystalline ferrite produced by cyclic heavy plastic deformation far below the austenitization temperature. Baumann et al. [54] investigated the WEL in corrugated rails and observed the WEL at corrugation crests, with a hardness of 1000 HV to 1200 HV.

TEM analysis revealed a nanocrystalline structure with a grain size of less than 50 nm. Based on these observations, they claimed that WEL formation due to a temperature increase alone does not seem possible and indicated the possibility of the dissolution of cementite due to severe plastic deformation [54].

Critical questions in the theory that WEL forms by plastic deformation are why the cementite dissolves and where the carbon from the dissolved cementite is accommodated. First, at temperatures lower than the austenitizing temperature, cementite is expected to be stable. Second, cementite has a much higher carbon centration, 6.7 wt%, than that in the ferrite, less than 0.001 wt% at room temperature. This means that during the severe plastic deformation, a higher density of sites to accommodate the carbon must be generated.

Meanwhile, similar nanocrystalline ferrite white layers as WEL are commonly observed in pearlite after applying severe plastic deformation, e.g. [56,71]. The extremely high nanohardness of 12 GPa and the nanometer size grains in the WEL [56] can be well reproduced by severe plastic deformation routes. A certain degree of strain seems to be necessary for the final nanometer size grains and the full cementite dissolution. It is commonly argued that the severe plastic deformation in pearlite produces high dislocation density and can refine grains down to tens of nanometers, both of which provide trapping sites for the carbon from the dissolved cementite. Calculations show that carbon has a higher affinity to dislocations in ferrite, 0.75-0.78 eV, than dislocation in cementite, 0.5 eV [72]. As a result, the driving force for cementite to dissolve exists during severe plastic deformation. With a dislocation density in the order of 10^{13} m^{-2}, a concentration of approximately 1 wt% of carbon can be accommodated. Theoretical modeling of cementite dissolution into ferrite during plastic deformation remains difficult, despite the numerous experimental studies.

The other hypothesis is that WEL is martensite, formed due to phase transformations. Österle et al. [55] study a WEL in field-loaded rail steels using a cross-sectional transmission electron microscopy (XTEM) and synchrotron X-ray diffraction (XRD). A martensite-like microstructure, e.g. high dislocation density, twinning substructure, is identified. Comparing the microstructure and the hardness of WEL with the martensite, formed by laser heating on the same steel grade, they conclude that the WEL is martensite with high dislocation density. Wild et al. [64] analyzed WEL observed in a corrugated rail track. Their SEM results show cementite particles within the WEL, which are mainly close to the WEL/pearlite boundary. The carbon concentration in the WEL in the rail surface is identified to be heterogeneous, by analyzing the lattice parameter changes in the ferrite phase using the same synchrotron XRD peak. Based on the results, they conclude that the characterized WEL is a martensite of nano-scale grain size containing cementite particles. Research by Wang et al. [65] detected retained austenite via X-ray diffraction (XRD) and further confirmed the martensitic nature of the WEL. Takahashi et al. [51] analyzed the WEL with atom probe tomography (APT) and found that lamella thinning had not occurred in the WEL. As a result, they conclude that the WEL region did not undergo severe plastic deformation. Together with the prediction of the increased temperature via frictional heat and from the shape analysis

of manganese profiles from APT, they conclude that the WEL is formed by martensitic transformation. Furthermore, a similar white martensite layer is observed in the wheel steels, which originally have a similar pearlitic microstructure [73–76]. Finally, a white layer is also commonly observed in steel components, whose working condition suffers significant temperature increases, e.g. in machining surface [77], hard turning [78,79].

The hypothesis that WEL is martensite indicates that a significant temperature rise occurs in the rail surface due to the contribution of frictional heat generated by wheel/rail contact. The pearlite must first transform to austenite and subsequently to martensite. The former process requires a significant temperature increase, e.g. 725 °C in Fig. 2.2. The rapid cooling after the wheel passed will transform austenite to martensite.

It can be well expected that the pearlite to austenite transformation can be incomplete during a single wheel passage. The transformation from ferrite and cementite to austenite requires reconstruction of crystal lattice structures, e.g. body-centered cubic ferrite to face-centered cubic austenite. The transformation requires also partitioning of carbon between cementite/austenite and ferrite/austenite, which is again temperature and time-dependent. Due to fact that the duration of a single wheel/rail contact time is typically in the magnitude of 10^{-3} second, there is very limited time for the pearlite to austenite transformation to complete and a carbon gradient can be expected due to its limited diffusion distance. Accordingly, a mixed microstructure of martensite, untransformed ferrite and cementite can occur, explaining the observations of cementite in WEL and the carbon gradient in [64].

A quantitative insight into the WEL formation via phase transformation may be obtained from the phase field modeling approach (PFM). Savran [80] and Militzer [81] performed separate PFM modeling of austenite formation in a pearlitic type microstructure under isothermal conditions and good agreement with experimental results is reached. Martensite is known to be a nonequilibrium phase and there is limited information about the kinetic data of martensite to austenite transformation. By treating martensite as a carbon-supersaturated ferrite, nevertheless, Thiessen [82] successfully established a reasonable match between the simulation and experimental results. This indicates that PFM can be a very promising approach to simulate the WEL formation via the phase transformation mechanism. A detailed study of WEL formation with PFM can be found in Chapter 6.

2.5 Summary and conclusions

This chapter reviews the literature regarding the microstructures in rail steels and the subsequent RCF damage formation. The RCF damage in steel with a fully pearlitic microstructure is due to plastic strain accumulation and plasticity exhaustion in the pearlite, via the plastic shakedown and ratcheting.

Premature damage initiation in pearlite steel will occur in the presence of PE ferrite, intermetallic inclusions, and WEL, which act as the microstructural weak sites. They serve as preferential stress/strain

accumulation sites, leading to an early failure in the surrounding matrix or their own fracture. Both lead to fatigue crack formation.

WEL is the most mysterious structural alteration in rail surface and the most important weak microstructure site. Comparing with PE ferrite and intermetallic inclusions, WEL is more difficult to be eliminated via metallurgic routes and its influence can only be distinguished through a sound understanding of its formation mechanism. The complicated wheel/rail contact conditions and the different loading histories of the studied rail steels in the literature fail to reach a universal hypothesis for the WEL formation. As a result, the origin of the WEL in the studied rails can vary significantly from track site to site due to loading conditions and microstructure characterizations are essential to achieve a sound understanding of WEL formation on the specific rail tracks/network.

References

[1] Li Z, Zhao X, Esveld C, Dollevoet R, Molodova M. An investigation into the causes of squats—Correlation analysis and numerical modeling. Wear 2008;265:1349–55.

[2] Li Z. 13 - Squats on railway rails BT - Wheel–Rail Interface Handbook, Woodhead Publishing; 2009, p. 409–36.

[3] Gui X, Wang K, Gao G, Misra RDK, Tan Z, Bai B. Rolling contact fatigue of bainitic rail steels: The significance of microstructure. Mater Sci Eng A 2016;657:82–5.

[4] Pointner P. High strength rail steels—The importance of material properties in contact mechanics problems. Wear 2008;265:1373–9.

[5] Pointner P, Joerg A, Jaiswal J. Deliverable report D4.1.5GL-Definitive guidelines on the use of different rail grades INNOTRACK GUIDELINE. 2009.

[6] Ekberg A, Paulsson B. Concluding technical report - Innotrack. 2010.

[7] Daniel W, Kerr M, Daniel AW. Final Report on the Rail Squat Project R3-105. 2013.

[8] Clayton P, Allery MBP. Metallurgical Aspects of Surface Damage Problems in Rails. Can Metall Q 1982;21:31–46.

[9] Cannon DF, Pradier H. Rail rolling contact fatigue Research by the European Rail Research Institute. Wear 1996;191:1–13.

[10] Franklin FJ, Garnham JE, Davis CL, Fletcher DI, Kapoor A. The evolution and failure of pearlitic microstructure in rail steel – observations and modelling. Woodhead Publishing Limited; 2009.

[11] Wu J, Petrov RH, Naeimi M, Li Z, Dollevoet R, Sietsma J. Laboratory simulation of martensite formation of white etching layer in rail steel. Int J Fatigue 2016;91:11–20.

[12] Sahay Mohapatra, Goutam, Totten, George E. SS. Overview of Pearlitic Rail Steel: Accelerated Cooling, Quenching, Microstructure, and Mechanical Properties. J ASTM Int 2009;6.

[13] Garnham JE, Davis CL. 5 - Rail materials A2 - Lewis, R. In: Olofsson UBT-WIH, editor., Woodhead Publishing; 2009, p. 125–71.

[14] Magel EE. Rolling Contact Fatigue: A Comprehensive Review. Washington DC: 2011.

[15] Kalousek J, Fegredo DM, Laufer EE. The wear resistance and worn metallography of pearlite, bainite and tempered martensite rail steel microstructures of high hardness. Wear 1985;105:199–222.

[16] Das Bakshi S, Shipway PH, Bhadeshia HKDH. Three-body abrasive wear of fine pearlite, nanostructured bainite and martensite. Wear 2013;308:46–53.

[17] Bhadeshia HKDH. High Performance Bainitic Steels. Mater Sci Forum 2005;500–501:63–74.

[18] Zheng C, Lv B, Zhang F, Yang Z, Kang J, She L, et al. A novel microstructure of carbide-free bainitic medium carbon steel observed during rolling contact fatigue. Scr Mater 2016;114:13–6.

[19] Bramfitt BL, Corporation BS. Structure / Property Relationships in Irons and Steels. Met Handb Desk Ed Second Ed 1998:153–73.

[20] Harzallah R, Mouftiez a., Hariri S, Felder E, Maujean JP. Impact and Sliding Wear Resistance of Hadfield and Rail Steel. Appl Mech Mater 2011;146:112–23.

[21] Lv B, Zhang M, Zhang FC, Zheng CL, Feng XY, Qian LH, et al. Micro-mechanism of rolling contact fatigue in Hadfield steel crossing. Int J Fatigue 2012;44:273–8.

[22] Harzallah R, Mouftiez A, Felder E, Hariri S, Maujean JP. Rolling contact fatigue of Hadfield steel X120Mn12. Wear 2010;269:647–54.

[23] Guo SL, Sun DY, Zhang FC, Feng XY, Qian LH. Damage of a Hadfield steel crossing due to wheel rolling impact passages. Wear 2013;305:267–73.

[24] Zhang M, Lv B, Zhang F, Feng X. Explosion Deformation and Hardening Behaviours of Hadfield Steel Crossing. ISIJ Int 2012;52:2093–5.

[25] Shariff SM, Pal TK, Padmanabham G, Joshi S V. Comparative Study on Dry Sliding Wear Behavior of Various Railroad Steels. J Tribol 2011;133:21602.

[26] Liu FC, Yang ZN, Zheng CL, Zhang FC. Simultaneously improving the strength and ductility of coarse-grained Hadfield steel with increasing strain rate. Scr Mater 2012;66:431–4.

[27] Zhang FC, Lv B, Zheng CL, Zou Q, Zhang M, Li M, et al. Microstructure of the worn surfaces of a bainitic steel railway crossing. Wear 2010;268:1243–9.

[28] Caballero FG, Bhadeshia HKDH. Very strong bainite. Curr Opin Solid State Mater Sci 2004;8:251–7.

[29] Stock R, Pippan R. RCF and wear in theory and practice-The influence of rail grade on wear and RCF. Wear 2011;271:125–33.

[30] Aglan H, Fateh M. Fracture and fatigue crack growth analysis of rail steels. J Mech Mater Struct 2007;2.

[31] Aglan HA, Liu ZY, Hassan MF, Fateh M. Mechanical and fracture behavior of bainitic rail steel. J Mater Process Technol 2004;151:268–74.

[32] Zhang MR, Gu HC. Microstructure and properties of carbide free bainite railway wheels produced by programmed quenching. Mater Sci Technol 2007;23:970–4.

[33] Hofer C, Bliznuk V, Verdiere A, Petrov R, Winkelhofer F, Clemens H, et al. Correlative microscopy of a carbide-free bainitic steel. Micron 2016;81:1–7.

[34] Sundman B, Jansson B, Andersson JO. The Thermo-Calc databank system. Calphad 1985;9:153–90.

[35] Porter DA, Easterling KE, Sherif M. Phase Transformations in Metals and Alloys, (Revised Reprint). CRC press; 2009.

[36] European Norm EN 13674-1. Railway applications – track – rail – Part 1: Vignole railway rails 46 kg/m and above. 2011.

[37] Hyzak JM, Bernstein IM. The role of microstructure on the strength and toughness of fully pearlitic steels. Metall Trans A 1976;7:1217–24.

[38] Elwazri AM, Wanjara P, Yue S. The effect of microstructural characteristics of pearlite on the mechanical properties of hypereutectoid steel. Mater Sci Eng A 2005;404:91–8.

[39] Taleff EM, Syn CK, Lesuer DR, Sherby OD. Pearlite in ultrahigh carbon steels: Heat treatments and mechanical properties. Metall Mater Trans A 1996;27:111–8.

[40] Naeimi M, Li Z, Petrov R, Dollevoet R, Sietsma J, Wu J. Substantial Fatigue Similarity of a New Small-Scale Test Rig to Actual Wheel-Rail System. Int J Mech Aerospace, Ind Mechatron Manuf Eng 2014;8:1998–2006.

[41] Eden HC, Garnham JE, Davis CL. Influential microstructural changes on rolling contact fatigue crack initiation in pearlitic rail steels. Mater Sci Technol 2005;21:623–9.

[42] Garnham JE, Davis CL. Very early stage rolling contact fatigue crack growth in pearlitic rail steels. Wear 2011;271:100–12.

[43] Garnham JE, Ding RG, Davis CL. Ductile inclusions in rail, subject to compressive rolling–sliding contact. Wear 2010;269:733–46.

[44] Hashimoto K, Fujimatsu T, Tsunekage N, Hiraoka K, Kida K, Santos EC. Effect of inclusion/matrix interface cavities on internal-fracture-type rolling contact fatigue life. Mater Des 2011;32:4980–5.

[45] Sun C, Lei Z, Xie J, Hong Y. Effects of inclusion size and stress ratio on fatigue strength for high-strength steels with fish-eye mode failure. Int J Fatigue 2013;48:19–27.

[46] Moghaddam SM, Sadeghi F. A Review of Microstructural Alterations around Non-Metallic Inclusions in Bearing Steel during Rolling Contact Fatigue. Tribol Trans 2016;2004:1–61.

[47] Bedekar V, Hyde R, Shivpuri R. TEM Investigation of Butterfly and White Etching Area Formed During Rolling Contact Fatigue. Microsc Microanal 2012;18:1778–9.

[48] Grabulov A, Petrov R, Zandbergen HW. EBSD investigation of the crack initiation and TEM/FIB analyses of the microstructural changes around the cracks formed under Rolling Contact Fatigue (RCF). Int J Fatigue 2010;32:576–83.

[49] Newcomb SB, Stobbs WM. A transmission electron microscopy study of the white-etching layer on a rail head. Mater Sci Eng 1984;66:195–204.

[50] Zhang HW, Ohsaki S, Mitao S, Ohnuma M, Hono K. Microstructural investigation of white etching layer on pearlite steel rail. Mater Sci Eng A 2006;421:191–9.

[51] Takahashi J, Kawakami K, Ueda M. Atom probe tomography analysis of the white etching layer in a rail track surface. Acta Mater 2010;58:3602–12.

[52] Dikshit V, Clayton P, Christensen D. Investigation of rolling contact fatigue in a head-hardened rail. Wear 1991;144:89–102.

[53] Grassie SL. Studs and squats: The evolving story. Wear 2015.

[54] Baumann G, Fecht HJ, Liebelt S. Formation of white-etching layers on rail treads. Wear 1996;191:133–40.

[55] L. WÖRHPAW. Investigation of white etching layers on rails by optical microscopy, electron microscopy, X-ray and synchrotron X-ray diffraction. Mater Sci Eng A 2001;303:150–7.

[56] Lojkowski W, Djahanbakhsh M, Bürkle G, Gierlotka S, Zielinski W, Fecht HJ. Nanostructure formation on the surface of railway tracks. Mater Sci Eng A 2001;303:197–208.

[57] Carroll RI, Beynon JH. Rolling contact fatigue of white etching layer: Part 1. Crack morphology. Wear 2007;262:1253–66.

[58] Seo J, Kwon S, Jun H, Lee D. Numerical stress analysis and rolling contact fatigue of White Etching Layer on rail steel. Int J Fatigue 2011;33:203–11.

[59] Carroll RI, Beynon JH. Rolling contact fatigue of white etching layer: Part 2. Numerical results. Wear 2007;262:1267–73.

[60] Ishida M. Rolling contact fatigue (RCF) defects of rails in Japanese railways and its mitigation strategies. Electron J Struct Eng 2013;13:67–74.

[61] Steenbergen M, Dollevoet R. On the mechanism of squat formation on train rails – Part I: Origination. Int J Fatigue 2013;47:361–72.

[62] Pal Valente, C., Daniel, W., Farjoo, M. S, Pal S, Valente C, Daniel W, Farjoo M. Metallurgical and physical understanding of rail squat initiation and propagation. Wear 2012;284–285:30–42.

[63] Clayton P. Tribological aspects of wheel-rail contact: a review of recent experimental research. Wear 1995;191:170–83.

[64] Wild Wang, L., Hasse, B., Wroblewski, T. , Goerigk, G., Pyzalla, A. E. Microstructure alterations at the surface of a heavily corrugated rail with strong ripple formation. Wear 2003;254:876–83.

[65] E. A. LWPASWW. Microstructure features on rolling surfaces of railway rails subjected to heavy loading. Mater Sci Eng A 2003;359:31–43.

[66] Pal S, Daniel WJT, Farjoo M. Early stages of rail squat formation and the role of a white etching layer. Int J Fatigue 2013;52:144–56.

[67] M. SPVCDWF. Metallurgical and physical understanding of rail squat initiation and propagation. Wear 2012;284–285:30–42.

[68] Pal S, Daniel WJT, Valente CHG, Wilson A, Atrens A. Surface damage on new AS60 rail caused by wheel slip. Eng Fail Anal 2012;22:152–65.

[69] Hono K, Ohnuma M, Murayama M, Nishida S, Yoshie A, Takahashi T. Cementite decomposition in heavily drawn pearlite steel wire. Scr Mater 2001;44:977–83.

[70] Murty BS, Ranganathan S. Novel materials synthesis by mechanical alloying/milling. Int Mater Rev 1998;43:101–41.

[71] Todaka Y, Umemoto M, Tsuchiya K. Nanocrystallization in Carbon Steels by Various Severe Plastic Deformation Processes. Nanomater. by Sev. Plast. Deform., Wiley-VCH Verlag GmbH & Co. KGaA; 2004, p. 505–10.

[72] Buono VTL, Gonzalez BM, Andrade MS. Kinetics of strain aging in drawn pearlitic steels. Metall Mater Trans A 1998;29:1415–23.

[73] Ahlstroem J. Residual stresses generated by repeated local heating events - Modelling of possible mechanisms for crack initiation. Wear 2016;366–367:180–7.

[74] Fletcher DI. Numerical simulation of near surface rail cracks subject to thermal contact stress. Wear 2013;314:96–103.

[75] Ekberg A, Kabo E. Fatigue of railway wheels and rails under rolling contact and thermal loading-an overview. Wear 2005;258:1288–300.

[76] Handa K, Kimura Y, Mishima Y. Surface cracks initiation on carbon steel railway wheels under concurrent load of continuous rolling contact and cyclic frictional heat. Wear 2010;268:50–8.

[77] Griffiths BJ. White Layer Formations at Machined Surfaces and Their Relationship to White Layer Formations at Worn Surfaces. J Tribol 1985;107:165.

[78] Hosseini SB, Klement U, Yao Y, Ryttberg K. Formation mechanisms of white layers induced by hard turning of AISI 52100 steel. Acta Mater 2015;89:258–67.

[79] Umbrello D, Rotella G. Experimental analysis of mechanisms related to white layer formation during hard turning of AISI 52100 bearing steel. Mater Sci Technol 2012;28:205–12.

[80] Savran VI. Austenite formation in C-Mn steel. Delft University of Technology, 2009.

[81] Militzer M, Azizi-Alizamini H. Phase Field Modelling of Austenite Formation in Low Carbon Steels. Solid-Solid Phase Transform. Inorg. Mater., vol. 172, Trans Tech Publications; 2011, p. 1050–9.

[82] Thiessen RG, Sietsma J, Palmer TA, Elmer JW, Richardson IM. Phase-field modelling and synchrotron validation of phase transformations in martensitic dual-phase steel. Acta Mater 2007;55:601–14.

[83] Steinbach I, Pezzolla F, Nestler B, Seeßelberg M, Prieler R, Schmitz GJ, et al. A phase field concept for multiphase systems. Phys D Nonlinear Phenom 1996;94:135–47.

Chapter 3 Materials and Characterization techniques

3.1 Introduction

In this chapter, details about the studied materials and the performed characterization techniques will be given. Rail specimens, showing rolling contact fatigue (RCF) damage, were investigated. On the one hand, RCF is usually observed in areas within several millimeters from the contact surface [1], so the microstructural characteristics in these affected areas are of major interest for this thesis. On the other hand, microstructures in zones free of deformation, e.g. the rail center, are used as a reference for the surface counterpart. The assumption is that the microstructure on the as-manufactured rail surface is identical to the microstructure in the center of the rail cross-section.

The microstructures in the rail steels were characterized by techniques at different resolution levels and aspects. Optical microscopy (OM), scanning electron microscopy (SEM) and transmission electron microscopy (TEM) were used to study the microstructure morphology at different scales and for the subsequent quantifications. The crystallographic characteristics, in addition to the phase components, in the specimens were studied using X-Ray diffraction (XRD), electron backscatter diffraction (EBSD) and transmission Kikuchi diffraction (TKD) in SEM and the electron diffraction method in TEM. The atom probe tomography (APT), currently the technique with the highest spatial resolution, is used to characterize the compositional characteristics in the WEL in this thesis. The main principles of the above-mentioned methods, in addition to the experimental settings, will be explained in the subsequent sections.

3.2 Rail steels

The rail steels, investigated in this thesis, was originally located on a straight track site between Steenwijk and Meppel in the Netherlands and had been in service during 1989 - 2007. The rail track is mainly a passenger line with a maximum operation speed of 140 km/h and an approximate annual 3,650,000 tons of loads are expected. This entails approximately 1.2 million wheel passages under the assumption of an average load of 3 tons per wheel passage. The rail track suffered from the squat problem at the rail crown, showing a typical two lung shape as in [5]. A well-developed squat in the studied rail, before removal, is shown and indicated by the white arrow in Fig. 3.1(a). The darkened surface areas, within the yellow dotted loop in Fig. 3.1(a), are shallow depressions produced by plastic deformation of materials above the subsurface crack by train wheels. These were subsequently corroded. The accumulated yearly loading was around 4.1 million tons. The notations RD, TD and ND in Fig. 3.1(a) refer to the train/rolling direction (RD), transverse direction (TD) and the direction perpendicular to the surface (ND).

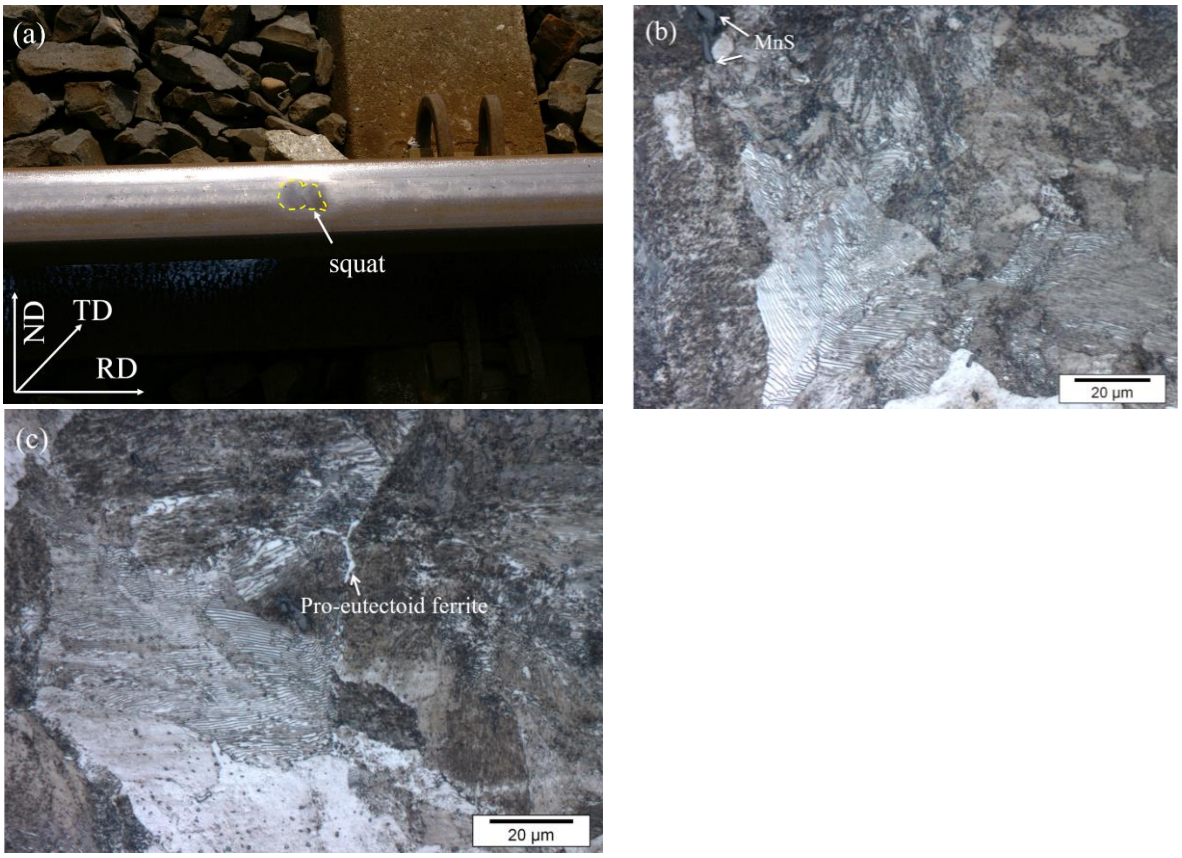

Fig. 3.1: (a) A photo of the rail track used for this study before removal. A mature squat defect, with representative two lung shape and surface darkening, can be observed; (b) A representative lamellar pearlitic microstructure in the rail surface and rail center; (c) A lamellar pearlite with a small fraction of pro-eutectoid ferrite in the specimen from rail web. The microstructures were revealed by 2% Nital.

The studied rail is a R260 Mn grade with a composition of 0.67%C, 1.51%Mn, 0.25%Si, 0.02%P and 0.02%S (in mass %). A nearly fully lamellar pearlite, Fig. 3.1(b), represents the microstructures in both rail surface and the rail center, ~ 25 mm beneath the contact surface. MnS intermetallic inclusions are frequently observed and one example is indicated by the arrows in Fig. 3.1(b). The MnS area density in rail surface and center zones were measured and averaged from pictures taken from minimum of six randomly selected areas. A magnification of 100 x is selected to ensure a sufficiently big area for a representative quantification. The number density of MnS particles in the surface area is $23 \pm 9 \times 10^6$ m^{-2} and is slightly higher than that in the central zones, which is $17 \pm 9 \times 10^6$ m^{-2}.

A small fraction of pro-eutectoid ferrite is observed at the prior-austenite grain boundaries in specimens taken from rail web, e.g. indicated by arrows in Fig. 3.1(c). The presence of pro-eutectoid ferrite must be due to the cooling conditions or possibly due to decarburization at the studied rail part during the manufacturing process.

3.3 Characterization techniques and analyzing procedures

Whether a technique is suitable for the characterization work depends on many factors, e.g. the fineness of the microstructure, and the purpose of the investigation etc. On the one hand, the viewing field in the facility should be large enough to have sufficient representativeness. Otherwise, characterization of multiple specimens from a similar area is required. On the other hand, the required microstructure details must be adequately resolved, e.g. with sufficient spatial or angular resolution. A smaller spatial and angular resolution means the more advanced capability of the facility.

3.3.1 Microhardness

Hardness can be an indicative measure of material strength [6]. An empirical correlation between the Vickers hardness, HV, to the strength of steels can be given as [6]:

$$\sigma = a + a_i HV \qquad (3.1)$$

in which a is a constant and a_i is the regression constant for correlating the Vickers hardness HV, in kgf/mm^2, to the yield strength of the steel σ, in MPa. This equation is valid for steels with the strength of 325 - 2350 MPa, irrespective of the microstructures, e.g. bainite, pearlite, ferrite-pearlite, martensite. Consequently, the differences in material strength can be reflected by the variation in the measured hardness. In loaded rails, a surface work-hardened area can form due to plastic deformation by the wheel/rail contact [7]. WEL can form in rail surface as well, but is much harder than the nondeformed pearlite matrix and the work-hardened pearlite in rail surface [3,4,9,10]. In this study, Vickers hardness is used to identify the changes in mechanical properties across the cross-section of the rail specimen due to the past train passages. The measurements were done in a Durascan 70 (STRUERS) hardness tester. The selected loads for the HV measurements vary with microstructures. A load of 0.49 N was considered to be large enough to give accurate measurements and is sufficient to reveal the hardness distribution in: (1) the WEL; (2) the possible surface work-hardened zone. A 2.94 N load was used to measure the

hardness of the undeformed pearlite area. The loading time is 10 s for all measurements. The hardness of the undeformed area of 290 HV, averaged from measurements from ten areas, is used as the reference throughout the thesis.

3.3.2 Optical and Scanning Electron Microscopy (OM and SEM)

Optical microscopy (OM) is one of the oldest and simplest characterization techniques, used for initial microstructure characterizations or preparations for further characterization with more advanced techniques. The classical sample preparation route before OM characterization includes mechanical grinding with SiC paper and polishing till 1 μm suspension. The as-polished specimens can then be immediately used for quantifications of intermetallic inclusions, e.g. size, number density etc.

Chemical etching, by 2-4 vol% HNO_3 in ethanol (Nital), is required to reveal the microstructures in the pearlitic steels. This etchant attacks the ferrite/cementite phase boundary and the pearlite colony or prior-austenite grain boundaries and the as-etched specimens can be characterized by OM and scanning electron microscopy (SEM). The revealed cementite and ferrite appear dark and bright respectively in the OM micrograph, e.g. in Figs. 3.1(b) and (c). Due to the very small lamellae distance in pearlite, OM can perform only partially the characterization task and SEM is a suitable alternative due to the improved spatial resolution in comparison to the OM.

Fig.3.2 (b) is an illustration of the signals generated due to beam/sample interactions in SEM, which can subsequently be collected by detectors for imaging or mapping. The secondary electrons (SE) are formed in multiple inelastic scattering processes from atoms in the specimen after interaction with the incident beam. The energy of the SE is a few electron-volts (eV), so only specimen volume within tens of nanometers from the surface can emit SE signals. Consequently, SE images show the topographical features on the specimen surface. In this thesis, SE is used to characterize the pearlite microstructure and WEL in the rail specimen and a typical SE-SEM image of the lamellar pearlite is shown in Fig. 3.2(c). A dedicated introduction of generation and application of other signals in SEM, Fig. 3.2(b), can be found elsewhere [12] and will not be discussed here.

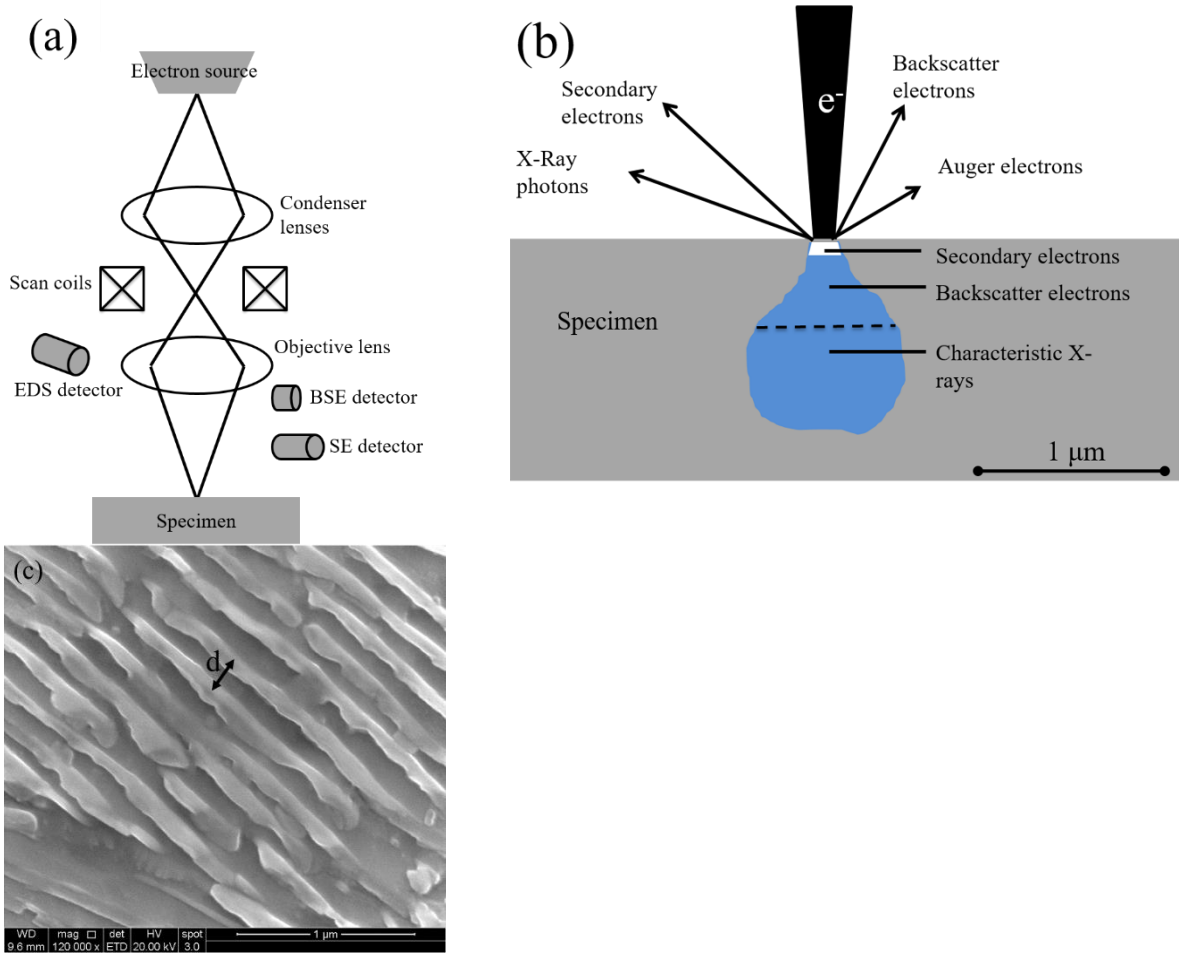

Fig. 3.2: (a) A schematic drawing of typical configurations of SEM; (b) Sketch of signals commonly used for imaging or mapping in most of the SEM; (c) A representative SE-SEM image of lamellar cementite and ferrite in the rail center.

In this thesis, a FEI Quanta 450 and a Jeol JEF 6500F SEM were used for sample characterization. Both microscopes are equipped with field emission electron guns (FEG) and the characterizations were done with an accelerating voltage of 10 or 15 kV. The observed cementite lamellar distance in the SEM micrographs can vary due to different orientations of the pearlite colonies to the intersected specimen surface. This makes a direct measurement of the true cementite interlamellar distance difficult. Therefore, the average value of more than 40 measurements was used to represent the true cementite interlamellar distance. The average cementite interlamellar distance in the reference zone is used as a parameter input for the initial microstructure in the phase field modeling in Chapter 6.

3.3.3 X-Ray Diffraction (XRD)

X-ray diffraction is a conventional technique for microstructure investigations. A schematic drawing of the common geometry of XRD equipment is shown in Fig. 3.3(a). The X-ray photons are generated and aligned in the X-ray tube. The X-ray photons interact with the specimen and are subsequently scattered or diffracted. A detector, with an identical angle to the horizontal plane as the X-ray tube, is positioned

on the other side of the specimen to collect the scattered X-ray photons. A spectrum like the one in Fig. 3.3(b) then appears on the computer screen. The intensity maxima in Fig. 3.3(b), i.e. the peaks, carry the crystal characteristic of the diffracting crystal planes {h k l} via Bragg's law:

$$n\lambda = 2d_{hkl}\, sin\, \theta \qquad (3.2)$$

in which λ is the wavelength of the incoming beam, d_{hkl} is the inter-planar distance between the crystal planes, with Miller indices (h k l), n is an integer and is the order of the reflection, θ is the angle between the incident or the reflected X-ray beams with the diffracted crystal plane.

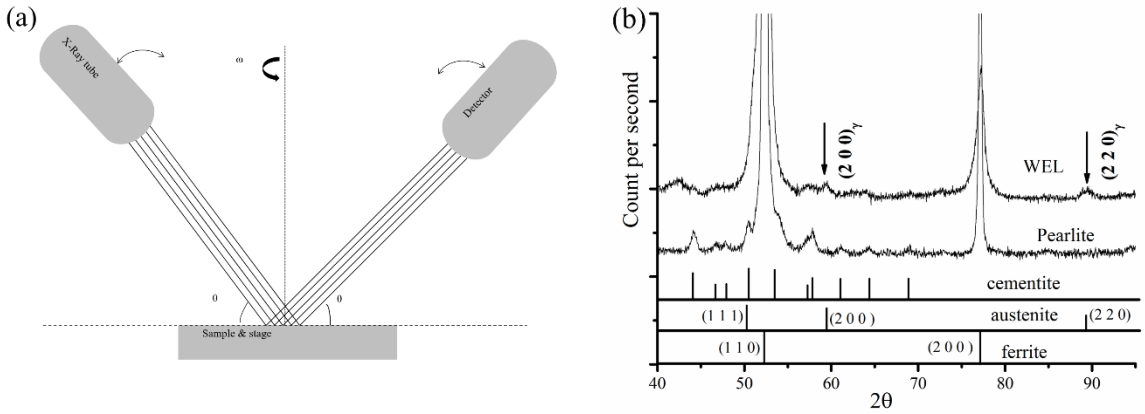

Fig.3.3: (a) Simplified schematic drawing of normal XRD configurations; (b) An example of two XRD spectra of the studied rail.

XRD was used to analyze the phase constituents in the WEL formed on the surface of the studied rail piece. Due to the massive corrosion and oxidation on the rail surface, a careful grinding, with grinding paper number 2000#, was done to remove the unwanted surface layer. A subsequent etching with 2 % Nital for 2 – 3 s was applied and the sample was cleaned with ethanol and dried by warm air. After the etching, the WEL clusters appeared lighter in color than the surrounding matrix due to the etching, for example, the white arrows in Fig. 3.4. Two areas on the rail surface were scanned: *(i)* areas including the WEL patch within the white loops in Fig. 3.4; *(ii)* areas without WEL, i.e. outside the running band. Another specimen was further cut from the rail center and was ground and polished till 1 μm diamond suspension. This specimen served as an additional reference sample for comparison with the above-mentioned surface regions. Scans were done in a Bruker D8 XRD machine with parallel beam geometry, and the scanned areas are approximately 11.8 × 5 mm^2. A cobalt source with a wavelength of 0.179 nm was used to generate the X-rays, at 45 kV and 25 mA respectively. The scanning step size (2θ) was set to be 0.03º with a time per step of 1 s.

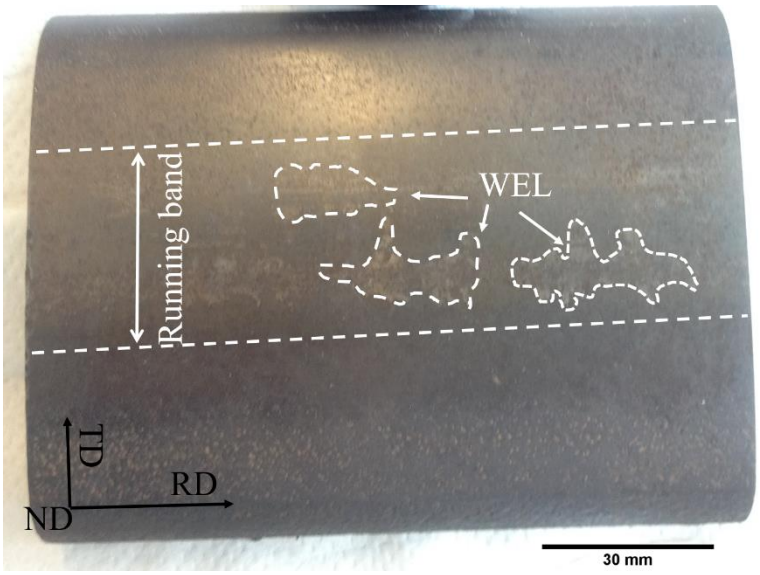

Fig. 3.4: Overview of rail surface after careful grinding and slight etching with 2% Nital. The WEL can be identified by color and part of WEL is indicated by arrows in the photo.

3.3.4 Transmission Electron Microscopy (TEM)

Transmission electron microscopy (TEM) is one of the most advanced characterization techniques, capable of resolving details down to crystal atomic planes. The configuration of TEM can be briefly explained by the simplified sketch in Fig. 3.5(a). The electron beam is generated by applying a high electrical field, 80 – 300 kV, which produces electron waves with a shorter wavelength than that in SEM and consequently result in improved spatial resolution. The spatial resolution will, however, be reduced due to beam broadening by the occurrence of both chromatic and spherical aberrations from the lens. The size and the parallelism of the electron beam are controlled before the beam reaches the specimen by adjusting the condenser lenses, the condenser aperture and the objective lens. The electron-transparent specimen for TEM analysis reduces the beam/specimen interaction volume, comparing with SEM, thus further improves the spatial resolution. A retractable objective aperture, with holes of different diameters, is located at the back focal plane of the image and can form either bright or dark field images. A selected area aperture, also with different diameters, can be located at the image plane of the objective lens and can choose the area of interest to form the selected area diffraction (SAD) patterns. The image or diffraction pattern is magnified by the underneath projective lens and is finally recorded by the detecting system. It should be noted the above-mentioned methods are part of the capacity of TEM and a comprehensive introduction of characterization methods in TEM can be found in the classic textbook of TEM by William & Carter [13].

The drawing in Fig. 3.5(b) illustrates how the bright field (BF) and dark field (DF) images form. When there is no aperture and in the diffraction mode in TEM, a diffraction pattern from a single grain or phase forms as the one at the bottom in Fig. 3.5 (b). The diffraction pattern carries crystal information of the diffracting volume by the Bragg's law in equation (3.2) and can be resolved by sequential indexing procedures. BF forms by allowing the directing beam in Fig. 3.5(b) passing through the objective

aperture, while DF is formed by using one of the diffracted beams. The DF is very useful for studying the distribution, size of the second phase or precipitates. In order to do so, one of the reflections from the phase must be chosen by the objective aperture.

In this thesis, the morphology and phase component in the WEL were characterized in a Jeol JEM 2200 FS with a Cs corrector, which corrects the spherical aberration, for the objective lens. All operations were done with accelerating voltage of 200 kV. The selected area diffraction patterns were formed by using the minimum aperture size of 100 nm.

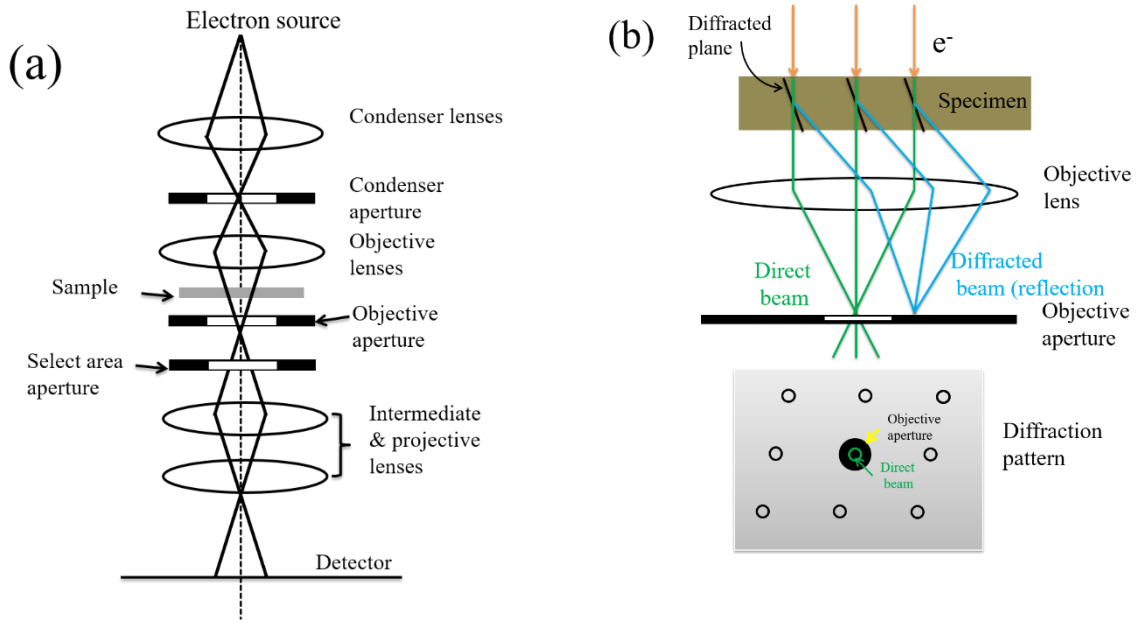

Fig. 3.5: (a) Simplified sketch of configuration in TEM; (b) Illustration of formation of BF and DF in the TEM.

3.3.5 Automated crystal orientation mapping techniques

3.3.5.1 Electron Backscatter Diffraction (EBSD)

Electron Backscatter Diffraction (EBSD) is one of the most widely used techniques for crystallographic study in materials science. The high accuracy of crystallographic orientation determination from EBSD enables the precise identification of orientation relationship between phases [14,15], the local misorientation, which can change due to deformation [16] etc. The crystal orientation information is extracted by analyzing the so-called Kikuchi bands, which form due to diffraction events in the specimen. A traditional configuration for EBSD measurements is shown in Fig. 3.6 (a). The specimen is tilted 20 ° away of the incident beam and Kikuchi bands form due to diffraction events in the specimen, corresponding to Bragg conditions as in equation (3.2). The generation of a Kikuchi band can be interpreted as shown in the drawing in Fig. 3.6(b). In this figure, the diffraction event at one of the {110} planes of a body-centered cubic (BCC) crystal structure is shown as an example. The two cones (green and blue) are due to diffracting of the incident beam at the {110} planes and the angles between the two

cones are two times the Bragg angles for the diffracting crystal planes. Kikuchi bands form if the two cones are intercepted and collected by the detector (phosphorous screen) placed close to the specimen and they are further processed by the commercial software for indexation.

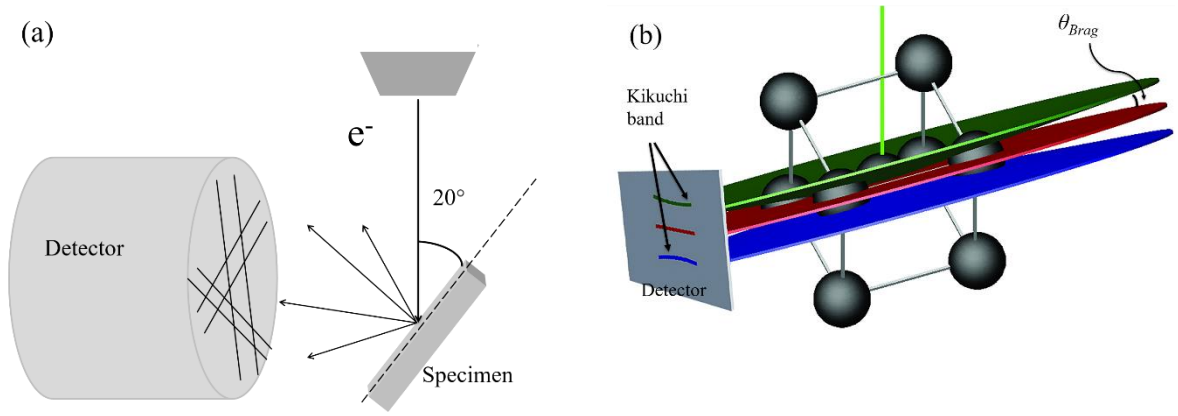

Fig.3.6: (a) A drawing of the common configuration of EBSD; (b) generation of Kikuchi band due to diffraction in the specimen. Fig (b) is by virtue of Oxford instruments [17]

The width of the Kikuchi *bands can be geometrically related* to the specific crystal plane distance, as shown in Fig. 3.6(b) and accurate measurements of crystal interplane angle and crystal plane spacing are essential for the automatic crystal orientation indexing [18]. As a result, accurate determination of the positions of the Kikuchi bands, collected by the EBSD detector, is crucial for a precise orientation indexation. However, the Kikuchi bands are usually broad diffuse lines with non-uniform intensities, especially in deformed specimens which contain high dislocation densities. As a result, the accurate Kikuchi band indexing becomes challenging and the subsequent automated crystal orientation identification [18], since the edges of the Kikuchi lines cannot be unambiguously identified. A Hough tra**n**sformation, a simple mathematic algorithm, is introduced to solve the problem. The Hough transformation translates the Kikuchi band position from the EBSD camera into separate points in the Hough space:

$$\rho = x\cos\theta + y\sin\theta \qquad (3.3)$$

(x, y) is the coordinate of one pixel in the Kikuchi line in an EBSD map, for example, the filled red circle in Fig. 3.7(a); ρ and θ are coordinates of lines that pass through the pixel. The filled red circle in Fig. 3.7(a) is subsequently translated to the red sinusoid curve in Fig. 3.7(b) by equation (3.3). After the transformation, all points in the Kikuchi line are translated into sea ries of sinusoid curves, which coincide at a single point, Fig. 3.7(b). After such translation, one Kikuchi band is translated into a bright point in the Hough space, e.g. translation from Fig. 3.7(c) to Fig. 3.7(d). The colors in both Figs. 3.7(c) and (d) are for demonstration purpose and the same color between the Kikuchi lines and the spot is to indicate the consequence after the Hough transform. The bright point in the Hough space can be well detected and the original position of the corresponding Kikuchi bands can be precisely determined and

used for the subsequent automated indexing in the software. The angular resolution of normal EBSD is typically smaller than 1° [19] .

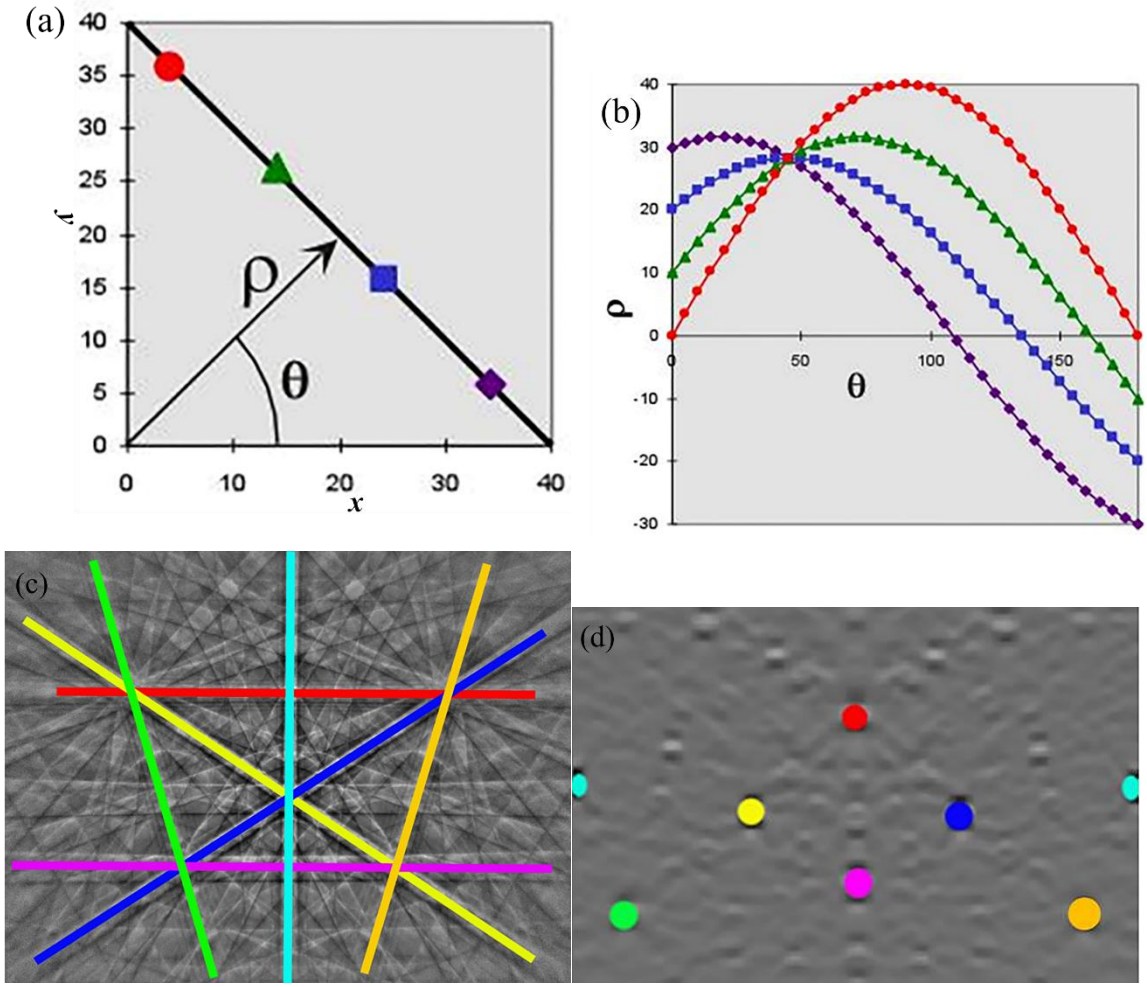

Fig.3.7: The Hough transformation from a real space in (a) into Hough space; An example of Hough transformation of Kikuchi bands in (c) into points in (d). Image (c) and (d) are by virtue of Oxford instruments [17].

In the work of this thesis, EBSD was used to characterize the WEL and the pearlite. A careful specimen preparation was required for such measurements. The specimens were ground and polished following classical metallographic sample preparation route till 1 µm diamond suspension. A further careful 40 minutes OPS polishing is applied with low pressure to remove the deformation layer caused by previous preparation steps.

The EBSD measurements were carried out in a FEI Quanta-450 SEM equipped with a field emission gun (FEG) and Hikari-Pro, EBSD detector. EDAX-TSL OIM® Data Collections v.6.2 was used for data acquisition. All measurements were performed with accelerating voltage of 20 kV, FEI-spot size of 5, a 40 µm final aperture, a step size of 50 nm and a hexagonal scan grid mode. With these settings, ~90% of the orientation data points were correctly indexed with confidence index higher than 0.06. The orientation data were analyzed by means of TSL OIM® Data analysis v. 7.3. The grains were defined

as regions containing minimum of 4 pixels with an internal misorientation less than 5° unless specifically mentioned. Otherwise, a specific explanation will be given.

3.3.5.2 Transmission Kikuchi Diffraction in SEM (TKD)

A great improvement in the spatial resolution from conventional EBSD is achieved by using thin electron-transparent foils, without sacrificing the angular resolution [20–23]. The relatively new method is named as transmission Kikuchi diffraction in SEM (TKD) or transmission EBSD and the indication of TKD will be applied throughout this thesis. A representative experimental configuration of TKD measurements is shown in Fig. 3.7 [25]. The thin TEM foils allow generation of Kikuchi bands via electrons that penetrate the specimen. Due to the significantly reduced sample thickness with respect to EBSD, the spatial resolution is greatly improved due to reduced sample volume interacting with the electron beam. Spatial resolution down to 10 nm was reported in [22] and a spatial resolution of 3 nm is reported in ref [24].

The TKD measurements were done in a FEI Quanta-450 SEM equipped with a field emission gun (FEG). The customized sample holder in Fig. 3.8, also in [25], was used for the measurements, and a total sample tilt of -10° was used to achieve the best results. An acceleration voltage of 30 kV, spot size #5 (aperture 40 µm) and a working distance of 5 mm were used for the scans. The step size is 12 nm.

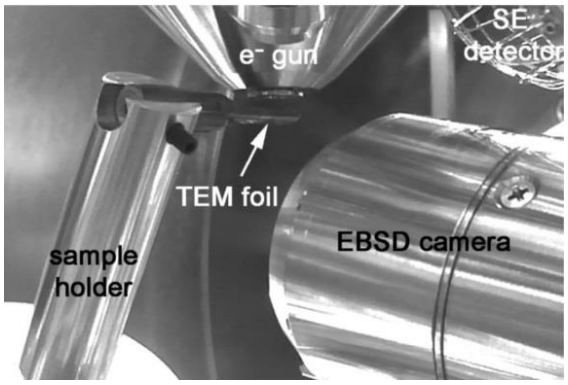

Fig. 3.8: Experimental configuration of TKD measurement in the current thesis and also in [25].

3.3.6 Dual Beam Focus Ion Beam milling (FIB)

A dual beam microscope with a Focus Ion Beam (FIB) is a single integrated system with both focus ion beam column and SEM column with field emission gun. A typical configuration of such a system is shown in Fig. 3.9(a) [26]. The SEM column is set to be vertical and the FIB column is tilted 52° from the horizontal plane. The ion beam (Ga+) and electron beam interact simultaneously with the specimen at the so-called coincident point [27]. The gallium source in the FIB column sputters away the surface material while the SEM system offers complimentary monitoring of the milling process, using high-resolution SEM. Such a combination enables precise site-specific sample extractions and failure prevention during preparing very thin specimens, for example for TEM characterization [27]. A dual

beam is usually equipped with EBSD attachment as conventional SEM and the sample stage is rotatable. This enables a three-dimensional characterization such as damage morphology [16,28] and also combined with 3-D EBSD [29,30], with sequential milling process and the subsequent reconstruction.

A FEI Nova 600 Nanolab DualBeam was used to prepare the TEM lamellae from WEL, at different locations relating rail depth: *(i)* surface WEL, ~ 3 μm beneath the rail surface; *(ii)* central WEL, ~ 12 μm below the rail surface and approximately in the center of the WEL; *(iii)* interface WEL, in the WEL and ~ 1 μm above the WEL/pearlite boundary.

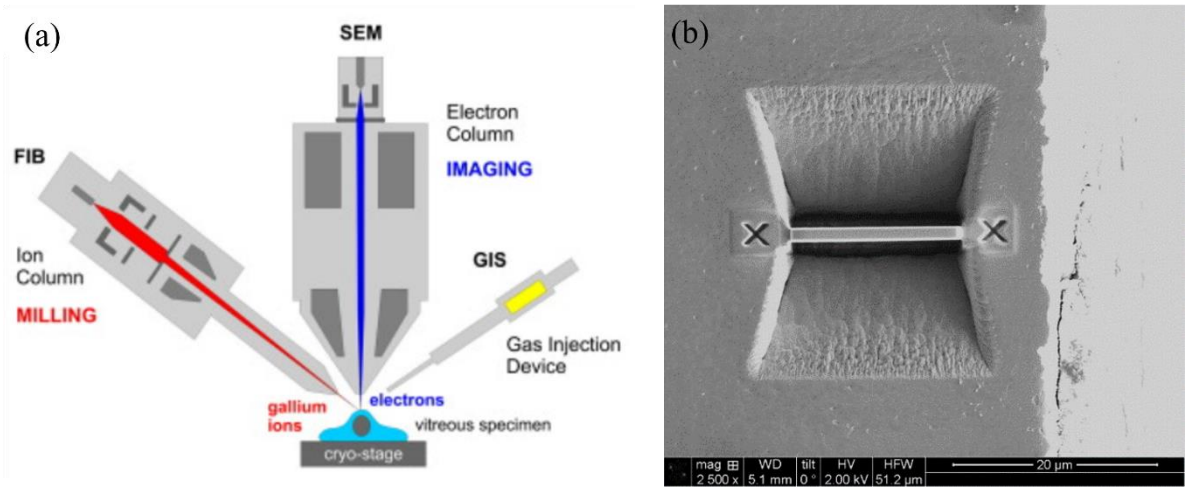

Fig. 3.9: (a) A sketch of configuration settings in a dual beam FIB [26]. (b) An SE-SEM snapshot of a to-be-prepared TEM lamella in the FIB.

3.3.7 Atom probe tomography (APT)

Atom probe tomography (APT) is currently the characterization technique with the highest spatial resolution. The advantage of APT can be the quick data collection rate, 3-D compositional reconstruction and the capability to characterize a large number of atoms with sufficient accuracy. The configuration of a local electrode atom probe (LEAP) is schematically represented in Fig. 3.10 [31]. Three main components form the LEAP system: (1) the specimen and the stage; (2) the local electrode; (3) the detector. The specimen for atom probe analysis is a sharp tip, with a radius of around 20 – 100 nm. The sample also serves as the positive electrode and a voltage is applied to ionize the atoms in the specimen at cryogenic temperatures. A local electrode is located concentrically close to the sample tip, enabling generation of the high electric field with a low voltage. This setting enables high data collecting rate, up to 10^7 atoms/hour, and also the enlarged field of view. Laser pulse was applied periodically to the sample tip to enhance and shorten the ionization process. A position sensitive detector is located to collect the ions. The ions reach the detector and their corresponding positions of origin in the sample tip are calculated based on the very accurate measurement of the time of flight (in ps), enabling the element identifications. The information along the z-axis is achieved by considering the difference of time of

flight from different evaporation sequences. The compositional profile, in three dimensions, can then be reconstructed by means of a dedicated software.

In this thesis, a Cameca LEAP-4000x HR 3D atom probe microscope, with a collecting efficiency of 42 %, was used to characterize the compositions in the WEL and the matrix pearlite. The APT needles were prepared by FIB and measured in voltage mode, with a pulse repetition of 200 kHz, a pulse fraction of 0.2 and a sample temperature of 20 K. The data was analyzed with Imago IVAS software, v3.6.

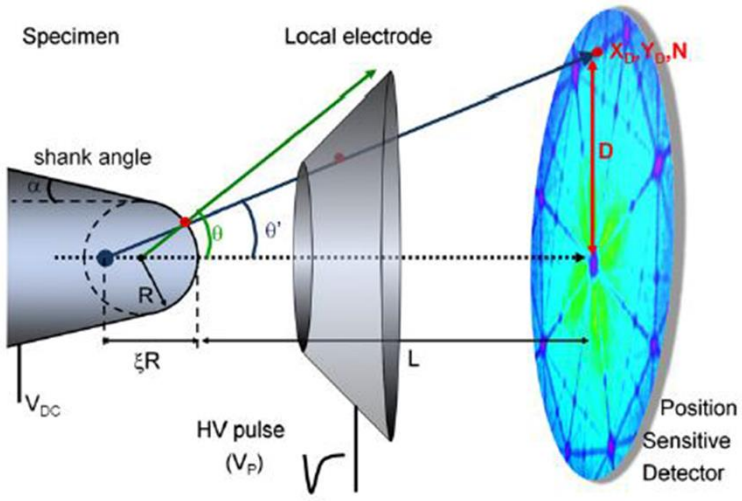

Fig. 3.10: Representative configuration of a LEAP [31].

3.3.8 Thermo-mechanical simulator

Gleeble 1500 was used to simulate fast heating and cooling cycles and to estimate the possibility for WEL formation via phase transformation. Cylindrical specimens, with a diameter of 6 mm and 75 mm in length, were recommended for combined fast heating and loading treatments. The specimens were quickly heated to temperatures between 730 °C and 930 °C, see Fig. 3.11 [3]. Heating rates of 20 °C/s and 200 °C/s were used to carry out the experiments. After heating to the selected temperature, the specimens were immediately quenched at a rate of 67 °C/s, using helium gas, to transform austenite to martensite. Such a cooling rate is shown to be sufficient to transform austenite to martensite. In order to study the role of deformation in the formation of martensite and also to be closer to the real condition, a compressive strain of 3 % was simultaneously applied during the heat treatment to 730 °C with a heating rate of 200 °C/s. The magnitude of the compressive strain was estimated by the numerical simulation in [3] and a Von-Mises strain of 0.3 % was used to represent the effective strain in the rails during the passage of one single wheel.

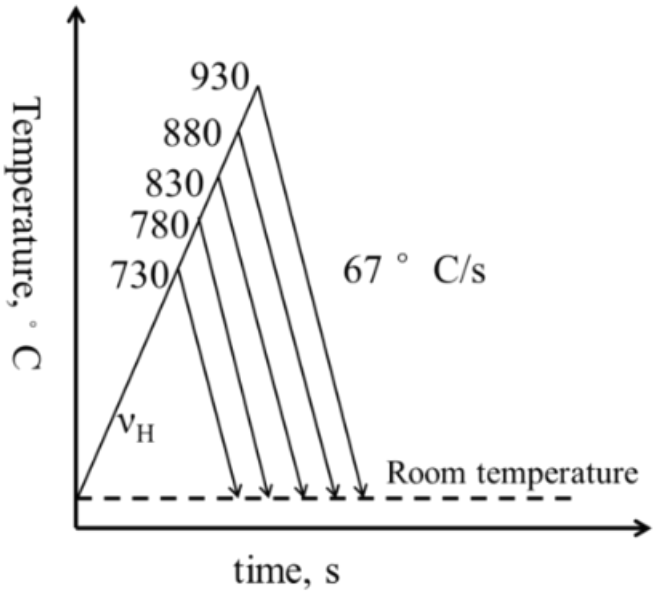

Fig. 3.11: Design of heat treatments for simulation of WEL microstructure formation only by fast heating and quenching. V_H is the heating rate.

References

[1] Magel EE. Rolling Contact Fatigue: A Comprehensive Review. Washington DC: 2011.

[2] Garnham JE, Beynon JH. The early detection of rolling-sliding contact fatigue cracks. Wear 1991;144:103–16.

[3] Wu J, Petrov RH, Naeimi M, Li Z, Dollevoet R, Sietsma J. Laboratory simulation of martensite formation of white etching layer in rail steel. Int J Fatigue 2016;91:11–20.

[4] Takahashi J, Kawakami K, Ueda M. Atom probe tomography analysis of the white etching layer in a rail track surface. Acta Mater 2010;58:3602–12.

[5] Li Z, Dollevoet R, Molodova M, Zhao X. Squat growth—Some observations and the validation of numerical predictions. Wear 2011;271:148–57.

[6] Pavlina EJ, Van Tyne CJ. Correlation of Yield strength and Tensile strength with hardness for steels. J Mater Eng Perform 2008;17:888–93.

[7] Pal S, Daniel WJT, Farjoo M. Early stages of rail squat formation and the role of a white etching layer. Int J Fatigue 2013;52:144–56.

[8] Stock R, Pippan R. Rail grade dependent damage behaviour - Characteristics and damage formation hypothesis. Wear 2014;314:44–50.

[9] Lojkowski W, Millman Y, Chugunova SI, Goncharova I V., Djahanbakhsh M, Bürkle G, et al. The mechanical properties of the nanocrystalline layer on the surface of railway tracks. Mater Sci Eng A 2001;303:209–15.

[10] Zhang HW, Ohsaki S, Mitao S, Ohnuma M, Hono K. Microstructural investigation of white etching layer on pearlite steel rail. Mater Sci Eng A 2006;421:191–9.

[11] Williams DB, Carter CB. The Transmission Electron Microscope BT - Transmission Electron Microscopy: A Textbook for Materials Science. In: Williams DB, Carter CB, editors., Boston, MA: Springer US; 2009, p. 3–22.

[12] Vernon-Parry KD. Scanning electron microscopy: an introduction. III-Vs Rev 2000;13:40–4.

[13] Williams DB, Carter CB. Transmission Electron Microscopy, A Textbook for Materials Science. Springer US; 2009.

[14] Ryde L. Application of EBSD to analysis of microstructures in commercial steels. Mater Sci Technol 2006;22:1297–306.

[15] DeArdo AJ, Cayron C, Karjalainen LP, Suikkanen PP. Crystallographic analysis of martensite in 0.2C-2.0Mn-1.5Si-0.6Cr steel by EBSD. Metall Ital 2011;103:13–22.

[16] Grabulov A, Ziese U, Zandbergen HW. TEM/SEM investigation of microstructural changes within the white etching area under rolling contact fatigue and 3-D crack reconstruction by focused ion beam. Scr Mater 2007;57:635–8.

[17] oxford instruments. http://www.ebsd.com/10-ebsd-explained (accessed September 12, 2016).

[18] Brewer LN, Field DP, Merriman CC. Electron Backscatter Diffraction in Materials Science. In: Schwartz JA, Kumar M, Adams LB, Field PD, editors., Boston, MA: Springer US; 2009, p. 251–62.

[19] Zaefferer S. A critical review of orientation microscopy in SEM and TEM. Cryst Res Technol 2011;46:607–28.

[20] Brodusch N, Demers H, Gauvin R. Nanometres-resolution Kikuchi patterns from materials science specimens with transmission electron forward scatter diffraction in the scanning electron microscope. J Microsc 2013;250:1–14.

[21] van Bremen R, Ribas Gomes D, de Jeer LTH, Ocelík V, De Hosson JTM. On the optimum resolution of transmission-electron backscattered diffraction (t-EBSD). Ultramicroscopy 2016;160:256–64.

[22] Trimby PW, Cao Y, Chen Z, Han S, Hemker KJ, Lian J, et al. Characterizing deformed ultrafine-grained and nanocrystalline materials using transmission Kikuchi diffraction in a scanning electron microscope. Acta Mater 2014;62:69–80.

[23] Trimby PW. Orientation mapping of nanostructured materials using transmission Kikuchi diffraction in the scanning electron microscope. Ultramicroscopy 2012;120:16–24.

[24] Bruker. https://www.bruker.com/products/x-ray-diffraction-and-elemental-analysis/eds-wds-ebsd-sem-micro-xrf-and-sem-micro-ct/quantax-ebsd/hardware/transmission-kikuchi-diffraction-in-sem/optimus.html (accessed February 12, 2017).

[25] Hofer C, Bliznuk V, Verdiere A, Petrov R, Winkelhofer F, Clemens H, et al. Correlative microscopy of a carbide-free bainitic steel. Micron 2016;81:1–7.

[26] Rigort A, Plitzko JM. Cryo-focused-ion-beam applications in structural biology. Arch Biochem Biophys 2015;581:122–30.

[27] Young RJ, Moore M V. Dual-Beam (FIB-SEM) Systems. In: Giannuzzi LA, Stevie FA, editors. Introd. to Focus. Ion Beams Instrumentation, Theory, Tech. Pract., Boston, MA: Springer US; 2005, p. 247–68.

[28] Evans MH, Walker JC, Ma C, Wang L, Wood RJK. A FIB/TEM study of butterfly crack formation and white etching area (WEA) microstructural changes under rolling contact fatigue in 100Cr6 bearing steel. Mater Sci Eng A 2013;570:127–34.

[29] Petrov R, Hernandez PG, García OL, Sharma H, Kestens L. 3D-Microstructural and Texture Characterization in Different Length Scales. Appl. Texture Anal., John Wiley & Sons, Inc.; 2008, p. 197–204.

[30] Petrov R, García OL, Mulders JJL, Reis ACC, Bae JH, Kestens L, et al. Three Dimensional Microstructure–Microtexture Characterization of Pipeline Steel. Mater Sci Forum 2007;550:625–30.

[31] Gault B, Loi ST, Araullo-Peters VJ, Stephenson LT, Moody MP, Shrestha SL, et al. Dynamic reconstruction for atom probe tomography. Ultramicroscopy 2011;111:1619–24.

Chapter 4 Characterization of WEL using advanced techniques: microstructural insight

Abstract:
Micro- to nano-scale characterizations were done to investigate the microstructures in the white etching layer (WEL), observed in a Dutch R260 Mn grade rail steel. Retained austenite in WEL is identified by electron backscatter diffraction (EBSD), transmission Kikuchi diffraction (TKD) and X-ray diffraction (XRD). EBSD and TKD methods quantify grains in the WEL with a size range of 20 nm – 4 μm. Transmission electron microscopy (TEM) identifies complex heterogeneous microstructure morphologies in the WEL: nano-twinning substructure with high dislocation density in WEL close to rail surface and untransformed cementite and dislocations in WEL close to the pearlite matrix. The study with atom probe tomography (APT) shows heterogeneous alloying element distribution through the WEL thickness. Accordingly, WEL is considered to be martensite with multi-layered microstructure. These findings are supported by the temperature calculations from the shape analysis of the manganese profile from APT measurements, related to manganese diffusion. The deformation characteristics in WEL and the pearlite beneath the WEL are discussed based on the EBSD and TKD measurements. The role of deformation in the martensitic phase transformation for WEL formation is discussed.
Keyword: white etching layer; rails; martensite; temperature; phase transformation; plastic deformation[1].

[1] The chapter is based on a scientific paper:

J Wu, R H Petrov, S Kölling, P Koenraad, L Malet, S Godet, J Sietsma. Micro and Nanoscale Characterization of Complex Multilayer-Structured White Etching Layer in Rails. Met 2018;8

4.1 Introduction

White etching layer (WEL) [1–8] is a common microstructure alteration on rail surface formed due to rail/wheel contact and is frequently associated with rolling contact fatigue (RCF) damage. During train passages, part of the initial pearlitic microstructure in the rail surface changes into a different structure. The new structure is typically revealed as a 10 – 20 μm featureless layer which appears in white color in the optical microscope, after etching with a nitric acid solution in ethanol. Furthermore, WEL is a common problem in rails with pearlite microstructure as it occurs: *(1)* with different initial microstructural components, i.e. ferrite-pearlite [8] or fully lamellar pearlite [1,5,6], *(2)* at various track sites, e.g. tangential tracks or curved rails. The presence of WEL is considered to cause crack initiation following brittle fracture of the WEL due to its high hardness, up to 1200 HV [5]. Worldwide observations of crack initiation at WEL are reported in the metallographic studies of loaded rails, e.g. Japan [9], the Netherlands [10], Australia [11], Great Britain [12]. Carrol et al. [13,14] performed laboratory twin disc tests to study the influence of WEL on RCF behavior in rails and they propose that WEL facilitates both wear and RCF processes in rails. In their subsequent numerical analysis, stress/strain concentration at WEL is identified and is considered to be consistent with their experimental observations.

Microstructure in the WEL is usually exploited by combined advanced characterization methods to trace its origin. Detection of tetragonal deviation from the body-centered cubic (BCC) lattice and retained austenite with (synchrotron) X-ray diffraction (XRD) is a commonly strong proof of martensite in the WEL [3,15]. Additional supportive evidence can be martensite twinning substructure observed by transmission electron microscopy (TEM) [3]. Using TEM, Takahashi et al. [6] determine WEL to consist of grains of a few hundred nanometers with high dislocation density, which is much finer than the pearlite beneath the WEL. Combined with atom probe tomography (APT) analysis, they identify manganese diffusion in the WEL, the quantification of which leads to the conclusion that the rail temperature has risen at least to 900 °C. Accordingly, the hypothesis that martensitic phase transformation leads to the WEL formation is proposed.

The other hypothesis is that WEL consists of nanocrystalline ferrite grains, which is a consequence of accumulated strain from passing train wheels. The original pearlite/ferrite structure is proposed to be significantly refined down to near ten nanometers grain size, and the cementite dissolves in it due to the plastic deformation. The extremely high hardness [7,16] is considered to be abnormal for a martensite microstructure produced by standard heat treatments, while it can be interpreted to be caused by strengthening from the ultra-fine ferrite grains. In some cases, WEL is considered to form according to this hypothesis despite the observation of martensitic-like characteristics. In the TEM work of Baumann [2] for example, a fully martensitic microstructure is identified and no retained austenite identification is reported in the analyzed WEL. In addition, their temperature calculations fail to support the required

temperature for pearlite to austenite transformation to occur. As a result, they propose that WEL forms due to the repeated deformation.

Formations of WELs according to the above hypotheses are well supported by separate laboratory simulations. For example, (ultra)fast heat treatments can produce martensite with hardness and grain sizes comparable to the studied WEL in rails [17], or with hardness and a twinning substructure for martensite [18]. A similar white layer is also commonly observed in the surface of loaded components, operating under conditions of significant temperature increase, e.g. in surface machining [19], hard turning [20,21]. On the other hand, nanocrystalline ferrite white layers are observed in pearlite after applying severe plastic deformation, e.g. [7,22]. The extremely high hardness and the nanometer-sized grains in the WEL [7], can be well reproduced by severe plastic deformation. A certain strain threshold seems to be necessary for the formation of nanometer size grains and complete cementite dissolution. Consequently, the microstructure in the WEL must be related to the loading conditions of the studied rail specimen. Relating to the wheel/rail contact, it will be realistic to assume that WEL forms via combined plastic deformation and temperature increase and the separate contributions depend on the loading history from wheels.

Among the above-mentioned works, few used automatic orientation mapping methods, e.g. electron backscattered diffraction (EBSD) and the recently developed transmission Kikuchi diffraction (TKD) with an improved spatial resolution [23,24]. The EBSD and TKD methods provide accurate crystal orientation and misorientation measurements and are inherently useful in revealing the deformation structures in the WEL [17] and the strain gradient in the rails [25,26]. Such structures are difficult to be characterized and quantified by other methods such as TEM and APT. In addition, EBSD can scan over a large bulk specimen, including the WEL and the surrounding matrix, offering a wider overview of differences between WEL and the pearlite beneath it in the grain size, deformation scale etc. The EBSD spatial resolution, typically 50 – 100 nm, may limit the identification of very fine grains in the WEL [26], while complementary information can be provided by TKD method, for which a spatial resolution down to 10 nm is reported [23,24]. As a result, EBSD and TKD will be useful to characterize the WEL and extra information might be extracted from the crystallographic aspects.

In this work, we perform a comprehensive characterization of the WEL, observed in an R260 Mn grade rail, by using methods at different resolution levels and from different aspects. We aim to explore an extensive insight into the formation mechanism of WEL via investigations on crystallographic, morphological and compositional characteristics. For such purpose, XRD, EBSD and TKD will identify the phase components in the WEL, while the EBSD and TKD also have the advantages of mapping the phase distribution and revealing the local misorientation changes caused during the train passages. TEM will be used to characterize the morphological and phase constituents in WEL at a higher resolution level. The APT is able to reveal the compositional variations in the WEL. Finally, the formation mechanism will be discussed based on the obtained results.

4.2 Materials and methods

The studied WELs were taken from an R260Mn grade rail track with a composition of Fe-0.67 wt% C-1.51 wt% Mn-0.21 wt% Si. The rail track was originally implemented in a straight track site between Meppel and Steenwijk in the Netherlands between 1989 and 2007 [17] and the loading conditions on the studied rail steel are described in section 3.2 in Chapter 3. The corroded and oxidized products in the rail surface, due to unprotected lab storage in the air after removal, was carefully ground away by using Struers #2000 grinding paper. The freshly revealed steel surface was first cleaned with ethanol and subsequently etched by 2 % Nital. The rail surface shows areas with noticeably different colors, e.g. the photo in Fig. 4.1(a). After etching, isolated blocks of light color areas can be identified close to the two edges of the running band. The surrounding areas were etched in gray shade and can be well recognized by the naked eye. The empty dashed white loops in the photo in Fig. 4.1(a) are for indication of shapes and distribution of the light blocks. The notations of RD, TD and ND refer to directions parallel with the traffic/rolling direction (RD), transverse direction (TD) and the direction perpendicular to the rail surface (ND) respectively.

An enlarged view of a light color block area, within the right-hand loop in Fig. 4.1(a), is shown in Fig. 4.1(b). It can be seen that the light color blocks are not continuous and there are smaller, separated light blocks beside the major one. These tiny light blocks are difficult to see in Fig. 4.1(a). Fig. 4.1(c) is a further magnified view of the largest light block in Fig. 4.1(b). Again, the structure in the main light zone is inhomogeneous and consists of light and dark gray areas. The hardness of the light blocks in Fig. 4.1(c) is measured to be ~ 820 HV and is much harder than the gray areas, which has a hardness close to the pearlite matrix reported 290 HV in [17]. The black portions in Fig. 4.1(c) are probably unremoved oxide layers. Finally, Fig. 4.1(d) is an optical micrograph of a cross-sectional specimen, cut through one of the light blocks. WEL with classic morphology and the pearlite beneath are well recognized. Consequently, the light portions in Fig. 4.1(a-c) are considered to be WELs. Fig. 4.1(e) is an indicative drawing to show the positions where APT tips and TEM lamellae were extracted.

XRD scans were first done on the WEL zones in the rail piece in Fig. 4.1(a), after final polishing with 1 μm diamond suspension. The scanned area including WEL was approximately 11.8×5 mm^2 and part of the surrounding matrix areas were inevitably included in the XRD scans, due to the erratic distribution of WELs in the rail surface. The scans were done in a Bruker D8 XRD machine with a parallel beam geometry, using Co Kα radiation. All scans were done at 45 kV acceleration voltage and 25 mA current. The scanning step size (2θ) was set to be 0.03º and the 40 –95° 2θ angular range was scanned with a speed of 1 s per step. For reference, one sample, cut from the rail center so not containing WEL, was scanned under identical settings and serves as a reference. Phase components in both WEL and pearlite areas were identified by comparing the 2θ positions of the diffraction peaks with the phase data in the ICDD database [27].

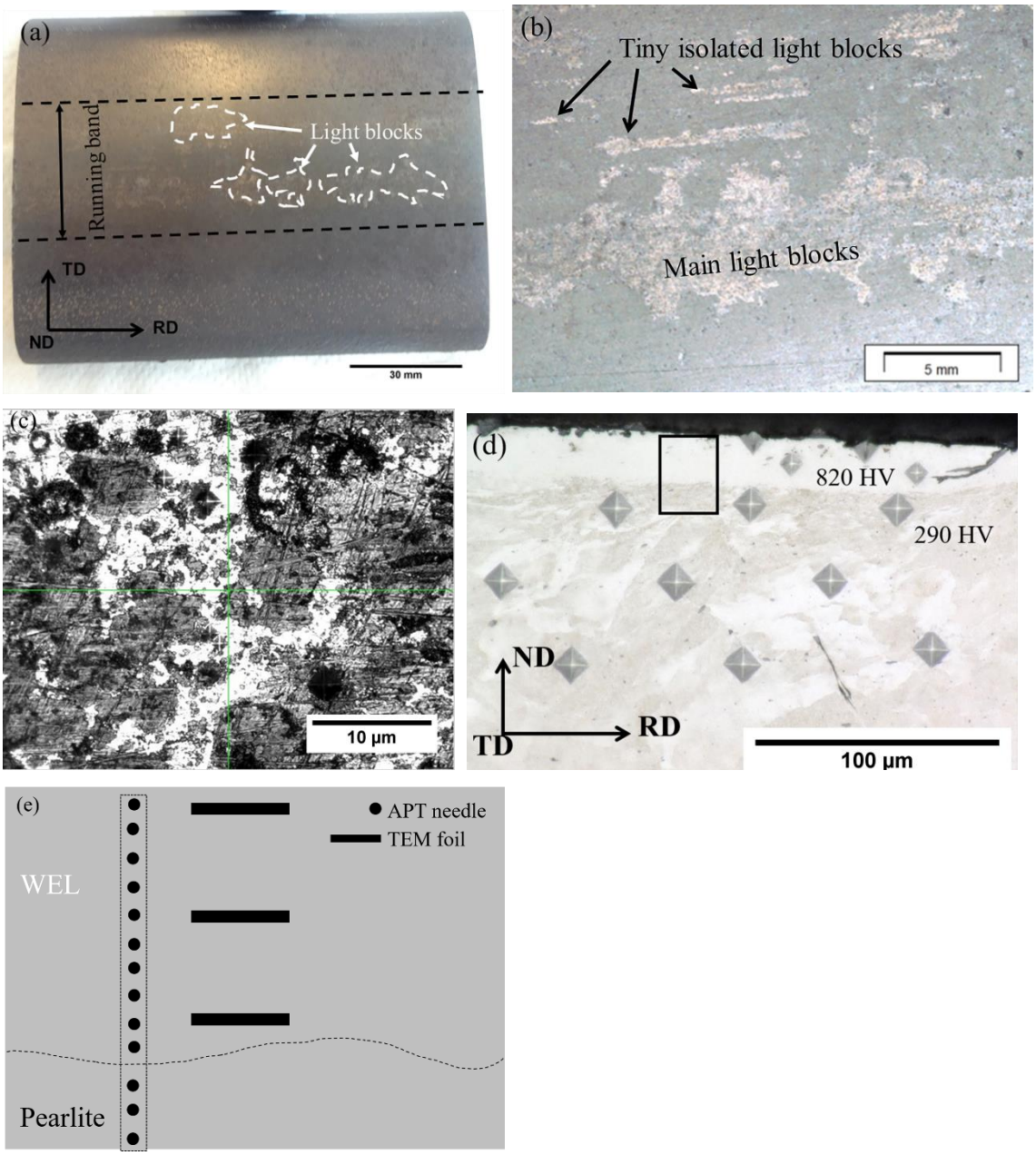

Fig. 4.1: (a) An overview of rail surface after careful grinding and subsequent etching with 2 % Nital; (b) the enlarged view of the downright light block; (c) A representative micrograph in the main light area in (b); (d) optical micrograph of a cross-sectional specimen, cut cross one of the WEL blocks in (a); (e) the enlarged view in the black rectangle in (d), with schematic indications of positions where the APT pillars and the TEM lamellae were extracted.

The cross-sectional WEL specimen in Fig. 4.1(d) was subsequently characterized by electron backscatter diffraction (EBSD), after following the sample preparation described in [17]. An FEI Quanta – 450 field emission gun scanning electron microscope (FEG-SEM), equipped with Hikari-Pro EBSD detector, was used for the scans. The orientation data was collected under 20 kV, FEI spot size 5, a final

aperture size of 40 μm and a working distance of 16 mm. The data was collected with EDAX-TSL OIM Data Collections *v6.2* software, on a hexagonal scan grid mode with a step size of 50 nm.

Three TEM lamellae were subsequently extracted from the specimen for EBSD scans. The lamellae were prepared by the Focused Ion Beam and lift-out method in a FIB-SEM, FEI Nova 600 Nanolab DualBeam. In the subsequent sections, the three TEM lamellae were named after their relative original positions in the WEL, schematically shown in Fig. 4.1(e): *(i)* surface WEL, ~ 3 μm beneath the rail surface; *(ii)* center WEL, ~ 12 μm below the rail surface and approximately in the center of the WEL; *(iii)* interface WEL, in the WEL and ~ 1 - 2 μm above the WEL/pearlite boundary. TKD measurements on the three lamellae were first done in the same SEM used for EBSD measurements in this chapter. The specimen holder configuration described in [28] was used for the study. The scans were done with a 5 mm working distance, 30 kV voltage and 12 nm step size. All orientation data was analyzed by the OIM post-processing software, version *7.30*.

The following cleanup procedures were applied to the EBSD and TKD data scans, before the comparison and quantification: *(i)* grain confidence index (CI) standardization with a grain definition of a threshold angle of 5° and minimum grain size of 6 pixels. This does not change the orientations but associates the CI of all pixels in the defined grains to the highest CI of the defined grain; *(ii)* neighbor orientation correlation. After this step, orientations of pixels with low CI, less than 0.1, will be reassigned to the neighbor grain orientation, based on the selected parameters in the OIM software. In this study, a clean-up level 3 was used for the neighbor orientation correlation. The grains were defined to have a minimum 5° misorientation with the neighbor grain and a minimum 4 and 8 pixels were defined for grains in EBSD and TKD respectively. After the cleanup procedures, the remaining pixels with CI<0.1 were removed from the EBSD scan as dubious and they appear as black pixels in the scans.

The same TEM lamellae were further characterized by a Jeol JEM-2200FS FEG-TEM with a C_s corrector for the objective lens. The experiments were done at 200 kV. A minimum objective aperture size of 100 nm was used for performing selected area diffraction (SAD).

For compositional analysis, the sharp needles along WEL depth were prepared from the same main WEL block, which is schematically shown in Fig. 4.1(e). The APT tips were carefully extracted in a FEI Nova 600 FIB/SEM Dual Beam set-up. The APT measurements were done in a Cameca LEAP-4000x HR 3D atom probe microscopy in voltage mode, with a pulse repetition of 200 kHz, a pulse fraction of 0.2 and a sample temperature of 20 K. The APT data was analyzed with Imago Visualization and Analysis Software (IVAS) version 3.6.

4.3 Results

4.3.1. X-Ray Diffraction (XRD) results

Fig. 4.2 shows the XRD spectra of scans on surface WEL and the central reference specimen, which has a fully pearlitic microstructure. The central reference specimen is identified to indeed consist of

cementite and ferrite. A similar phase composition is recognized in the spectrum of surface WEL specimen, while additionally {2 0 0} and{2 2 0} peaks of austenite are identified. The cementite peak intensity in the surface WEL spectrum is very weak, compared with the reference pearlite sample. In addition, the {1 1 0} and {2 0 0} peaks of ferrite in the surface WEL specimen are broader than that of the reference sample and are slightly asymmetric. This can be due to peak broadening caused by small grains or due to high dislocation densities. The unexpected peaks in the WEL specimen, at 42° in Fig. 4.2, are from the unground oxide, since excessive grinding was avoided not to remove WEL in the rail surface during sample preparation for XRD measurements.

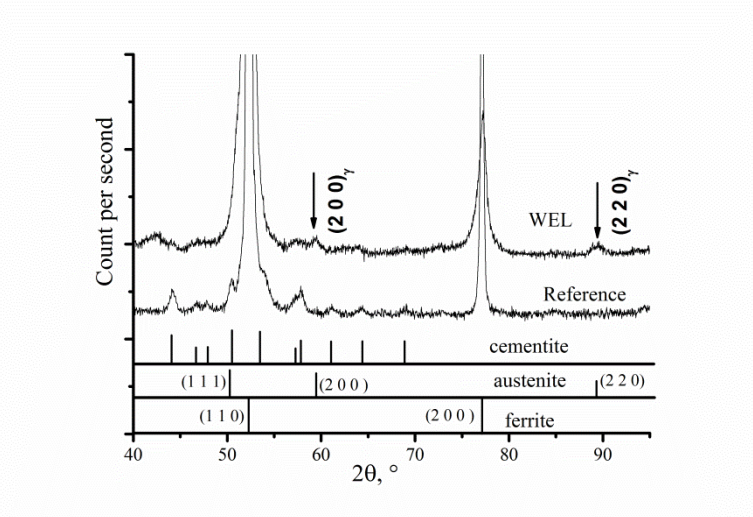

Fig. 4.2: XRD spectra of the WEL zone at rail surface and the reference pearlitic specimen from the rail center

4.3.2. Electron Backscatter Diffraction (EBSD) results

Fig. 4.3(a) shows the grayscale image quality (IQ) map of ferrite, from the EBSD scan on the WEL specimen. Superimposed is the color-coded inverse pole figure (IPF) of austenite. No pixels were discarded for the mapping. The WEL can be differentiated from the pearlite area by areas with lower IQ. It appears in dark gray shades, indicating higher dislocation density and/or very fine grains in the WEL. The grains within the WEL are heterogeneous both in size and morphology. The WEL close to the rail surface, e.g. within the zone 2 in the empty dashed rectangle in Fig. 4.3(a), show random morphology, while the subsurface WEL has elongated grains, e.g. in zone 1 in Fig. 4.3(a). Furthermore, individual WELs in the pearlite zone, identified by the low IQ, are observed and are partly indicated by solid black arrows in Fig. 4.3(a). Isolated WELs in the pearlite region, and separated from the main big WEL block, are so frequently observed that it can be used to indicate the propagating characteristics of WEL during the loading history.

Austenite is frequently identified in the WEL, e.g. the superimposed IPF in Fig. 4.3(a). There is no clear trend of austenite distribution relating to the WEL depth position and austenite grains are located both close to the rail surface and close to the WEL/pearlite boundary.

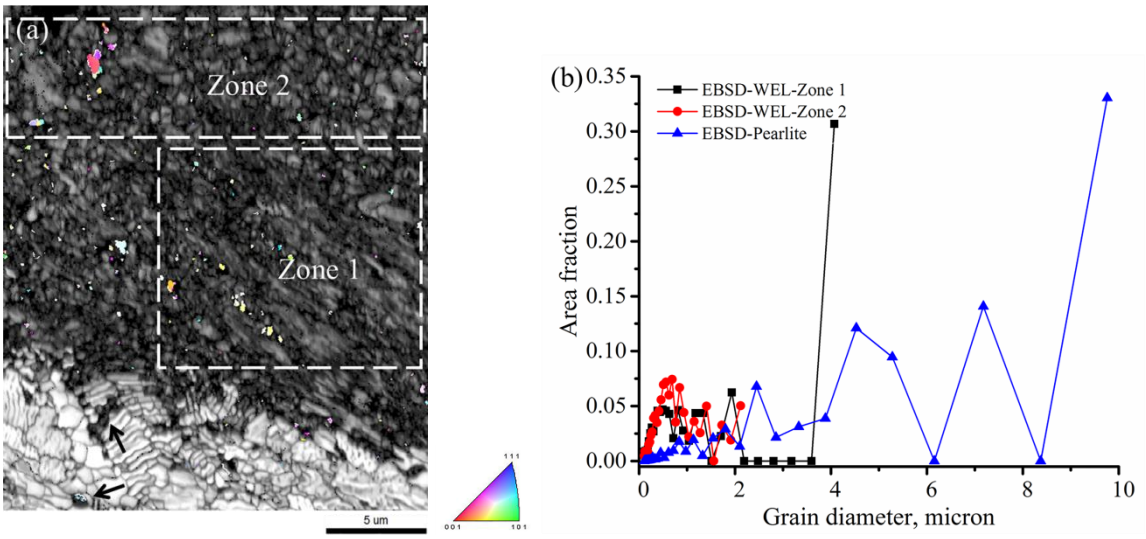

Fig. 4.3: (a) The image quality map of WEL imposed with the inverse pole figure of austenite. Part of the pearlite beneath the WEL was also included for the mapping; (b) comparison of grain diameter of the zone 1 and zone 2 in (a) and also pearlite area.

Fig. 4.3(b) shows the martensite grain size distribution, quantified from the zone 1 and zone 2 in Fig. 4.3(a). The grain size distribution of pearlite area beneath the WEL is included for comparison. It can be seen that the grain size ranges of zone 1 and 2 are different. The grains in 'zone 1' are 110 nm – 4 µm, which is wider than the grain size distribution in zone 2, 112 nm – 2 µm. Grain size of the pearlite ferrite underneath is bigger than in the WEL zones, with 113 nm – 10 µm. The average grain size of zone 1, zone 2 and pearlite ferrite are 323 ± 236 nm, 302 ± 314 nm and 798 ± 320 nm respectively. It should be noted that most of the grains are with sub-micron size while only a few grains exceed 1 micron. Fig. 4.4(a) shows the kernel average misorientation (KAM) map of the BCC ferrite phase in WEL, Fig. 4.3(a), using a threshold of 5° and the 1st neighbor. The dark zones are due to the applied threshold of 5° and 4 pixels for grain definition. The fraction of green and yellow, misorientation of 1 – 3°, in WEL indicate the deformation history in the rails. Such zones are much less in the pearlite area in Fig. 4.4(a) and are mainly located at the grain boundaries and the cementite/ferrite phase boundaries. Fig. 4.4(b) is the plot of BCC KAM distribution, mapped from the whole WEL and the pearlite underneath the WEL. The KAM plot of a reference area, 500 µm beneath the rail surface and deformation-free, is added as a reference. It can be seen that the WEL has distinctly higher KAM than the subsurface pearlite and reference pearlite and the latter two areas have similar KAM distributions.

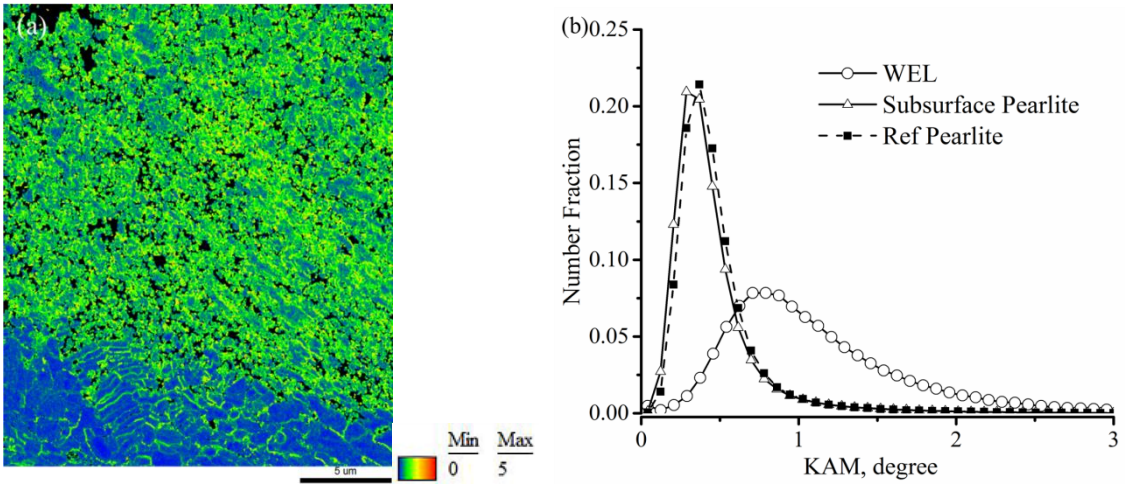

Fig. 4.4: KAM map of the WEL specimen, using 5 ° and 1st neighbor in (a); and KAM plot of ferrite in WEL and pearlite underneath the WEL respectively (b).

4.3.3. Transmission Kikuchi Diffraction (TKD) results

Figs. 4.5(a) – (c) show the TKD-IQ maps, superimposed with the color-coded IPF of austenite, of the three TEM foils extracted from the WEL. The martensite-like morphology can be seen in the IQ map of surface WEL and center WEL, Figs. 4.5(a) and (b). The grains in both lamellae can be observed to be heterogeneous and grains in central WEL appear to be finer than the surface ones. The microstructure in the interface WEL in Fig. 4.5(c) is different from those in Figs. 4.5(a) and (b). Dark parallel rod-like particles, which fail to be indexed, are observed in this TEM lamella. The white line boundaries, with angle/axis rotation of 90° <1 1 2>, are to show the boundaries character between austenite and bcc matrix. Among the three TEM foils, the central specimen shows the highest fraction of retained austenite and austenite grains are frequently observed at the recognized grain boundaries.

Fig. 4.6(a) shows the ferrite equivalent grain diameter distribution in the surface WEL, center WEL, and interface WEL. Grain size in the surface and interface WEL are comparable in the size range while central WEL has the finest grain size range, below 800 nm. The surface and the interface WELs have larger grain size, exceeding 1 µm. The average grain size of surface WEL, central WEL and interface WEL are 640 ± 116 nm, 370 ± 119 nm and 887 ± 146 nm respectively. Fig. 4.6(b) shows the KAM distribution measured in the three TEM foils. The interface WEL has the lowest KAM whereas the central and the surface zone of the WEL have practically the same KAM distribution.

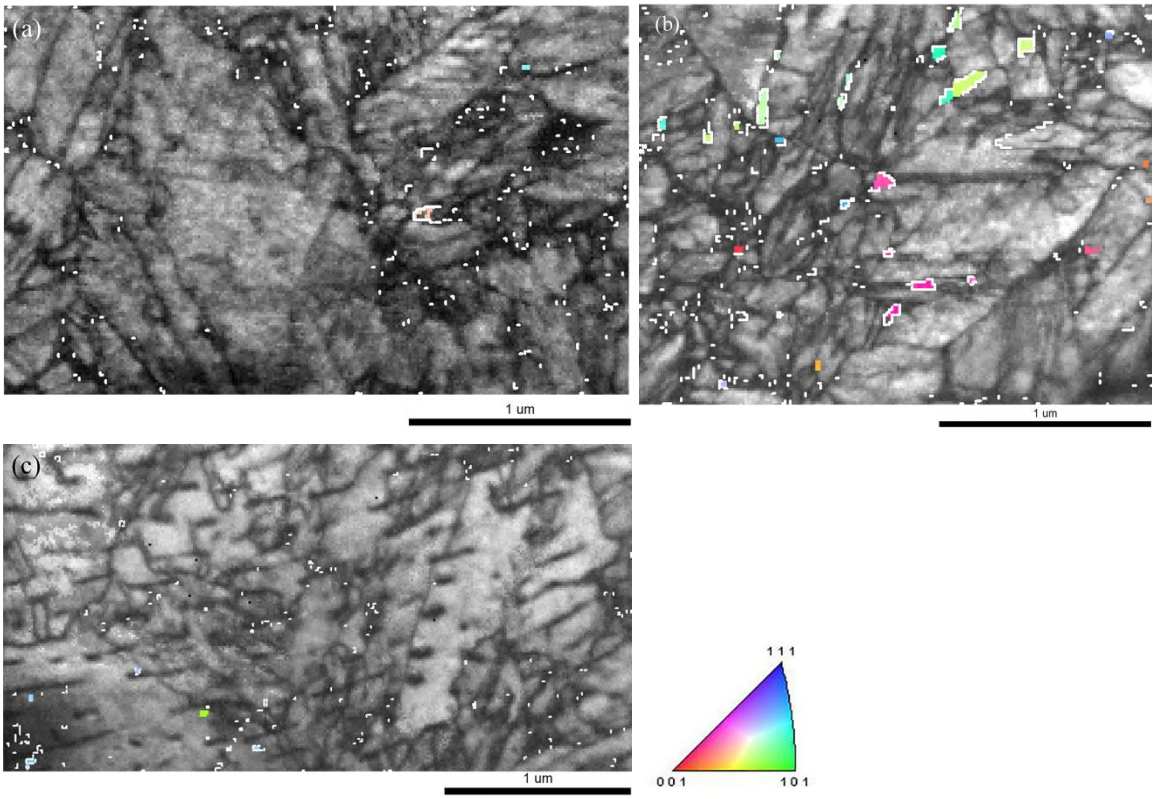

Fig. 4.5: The IQ map superimposed with the IPF of austenite of (a) surface WEL; (b) central WEL; (c) interface WEL. Colored regions indicate austenite grains, according to the oriental scheme.

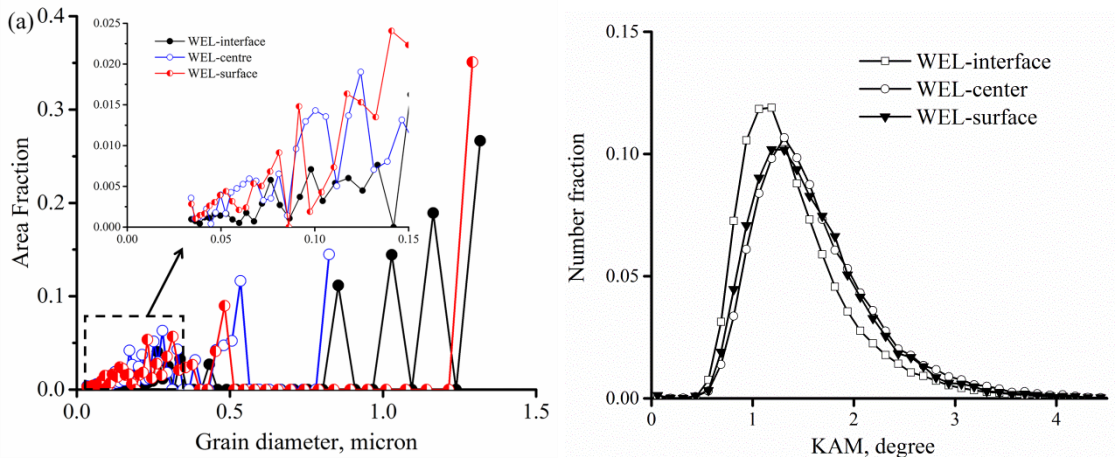

Fig. 4.6: (a) Plot of grain diameter vs area fraction of the characterized TEM foils; (b) Plot of KAM of the characterized TEM foils, using 4th neighbor.

4.3.4. Transmission Electron Microscopy (TEM) results

Fig. 4.7(a) is a representative bright field (BF) TEM image of the surface WEL specimen. The high dislocation density and the twinning-like structures are frequently observed through the whole TEM foil. Fig 4.7(b) shows the selected area diffraction (SAD) pattern of the area within the yellow circle in Fig. 4.7(a). The indexing identifies a {1 1 2} type twinning and the simulated pattern of Fig. 4.7(b) is shown in Fig. 4.7(d). The black arrow indicates the {1 1 2} twinning planes. Fig. 4.7(c) is a dark field (DF)

image, using the reflection ($\bar{2}$ 1 1) of the twinning plane. Due to the high dislocation density in the characterized TEM foil, an accurate quantification of the dislocation density is impossible.

Fig. 4.8 is a typical BF image of the center WEL TEM foil. In this specimen, the twinned structures and high dislocation density regions are also observed, although they are less common in this zone (subsurface WEL) than in the surface WEL.

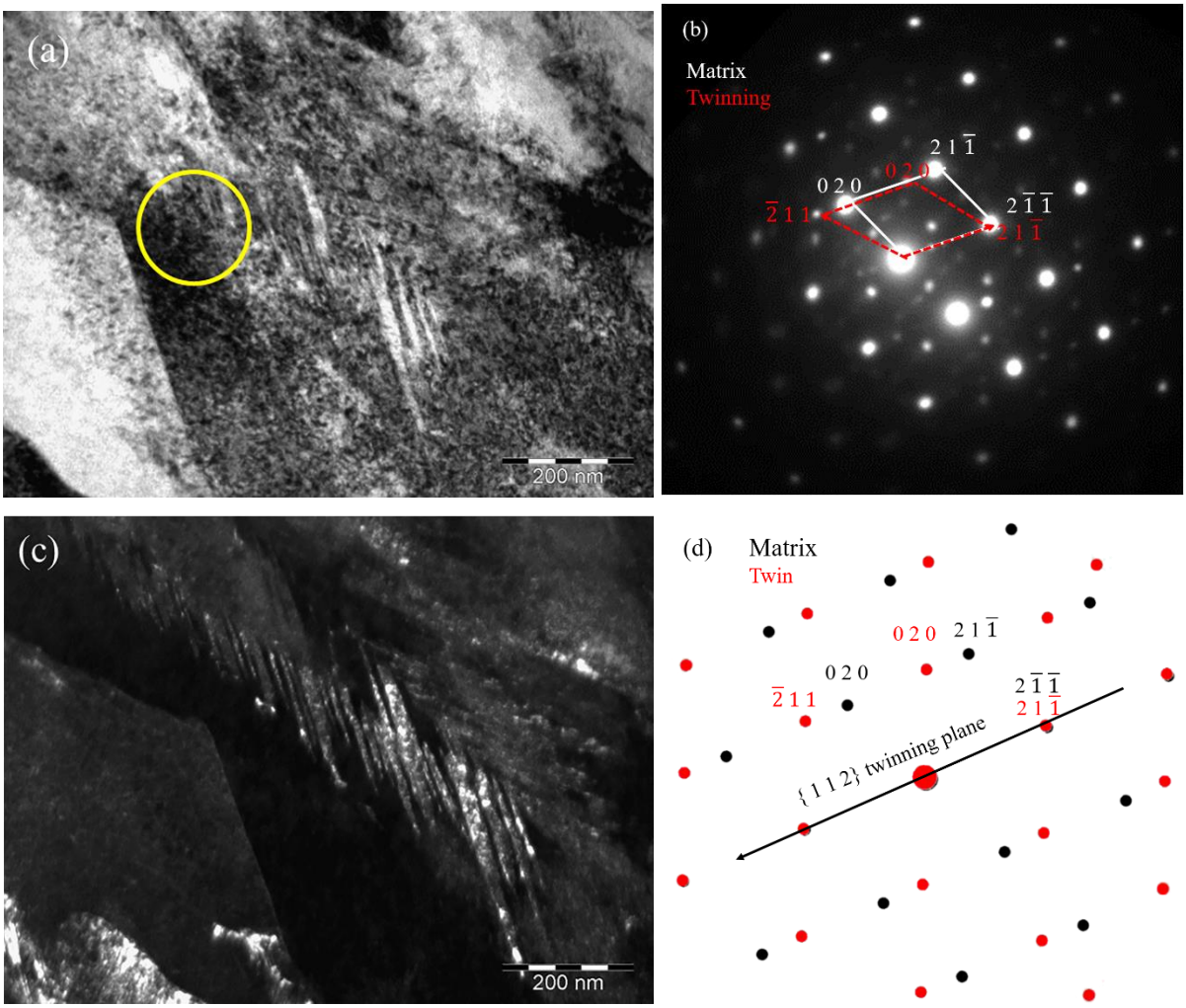

Fig. 4.7: (a) The bright field image of surface WEL in the TEM foil. The yellow circle is for forming the selected area diffraction pattern in (b), from zone axis $[1\ 0\ 2]_{matrix}$; (c) The dark field image formed using reflection (-2 1 1) of the twinning plane; (d) The simulated diffraction pattern corresponding to (b).

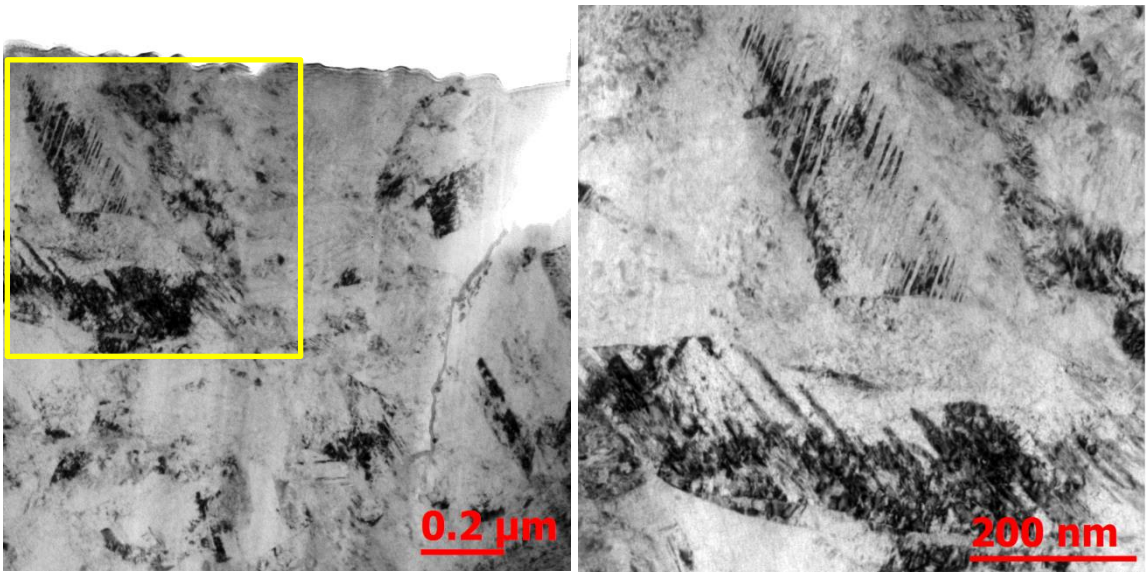

Fig. 4.8: (a) A representative BF micrograph of microstructure in the central WEL; (b) The enlarged view of the rectangle in (a).

Figs. 4.9(a)-(d) and Figs. 4.10(a)-(d) are two examples of microstructures in the interface WEL. In this specimen, the twinning structure is not as obvious as in the surface and subsurface WEL while a lamellar morphology is observed in the BF image in Fig. 4.9(a). The lamellae appear to be parallel and they look fragmented. A SAD pattern was taken in the yellow circle in Fig. 4.9(a) and is shown in Fig. 4.9(b). The indexing of pattern in Fig. 4.9(b) is presented in Fig. 4.9(d), revealing the following orientation relationship:

$(112)_\alpha // (\bar{2}\bar{3}3)_\theta$

$[\bar{6}\,\bar{4}\,1]_\alpha // [\bar{6}\,9\,5]_\theta$

This orientation relationship is in accordance with the Bagaryatsky orientation relationship between cementite (θ) and ferrite (α) [29], hence the elongated dark structures are most probably remaining or partially dissolved cementite.

The dark field (DF) image in Fig. 4.9(c) is formed using the reflection of $(2\bar{1}1)_\theta$.

Figs. 4.10(a)-(d) is another example of the microstructure in the interface WEL TEM foil, where the lamellar structure as in Fig. 4.9(a) is not observed. The indexing of the SAD pattern in Fig. 4.10(b) reveals the orientation relationship:

$(0\bar{1}1)_\alpha // (022)_\theta$

$[100]_\alpha // [0\bar{1}1]_\theta$

The DF image in Fig. 4.10(c) is formed using the reflection of $(2\ 1\ 1)_\theta$. High dislocation density is visible in Fig. 4.9(a) and Fig. 4.10(a).

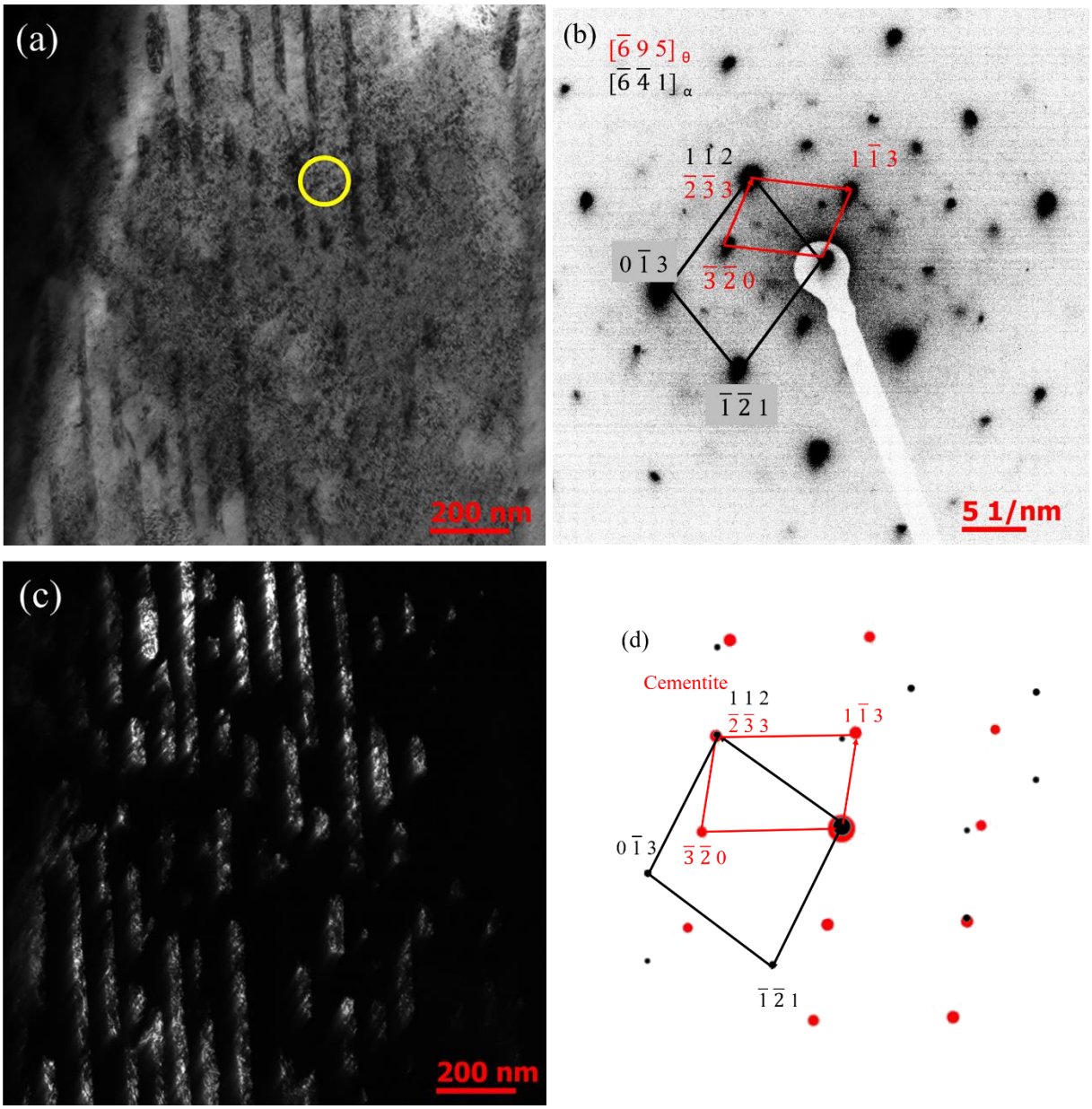

Fig. 4.9: (a) The BF image of interface WEL- TEM specimen; the SAD pattern of the area in the empty circle in (a) is shown in (b) and the indexed pattern is presented in (d). The DF image in (c) is formed by using $(2\bar{1}1)$ reflection of cementite.

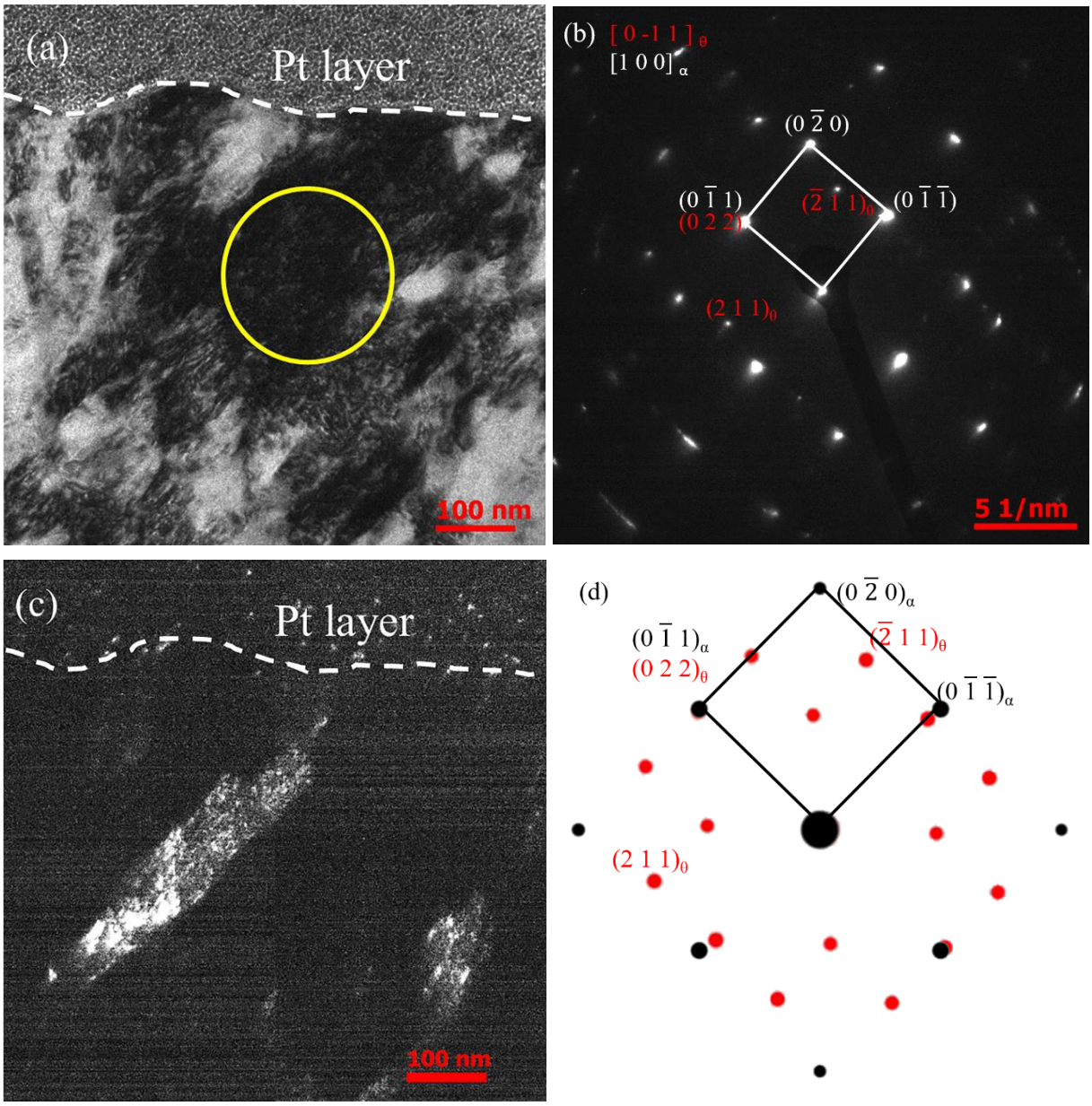

Fig. 4.10: (a) The BF image of another area in WEL-interface TEM specimen; the SAD pattern of the area in the empty circle in (a) is shown in (b) and the indexed pattern is presented in (d). The DF image in (c) is formed by using (211) reflection of cementite.

4.3.5 Atom Probe Tomography (APT) results

Fig. 4.11(a) shows the atomic distribution of carbon, manganese and silicon in an APT needle, extracted ~ 28 μm beneath the rail surface and ~ 3 μm beneath the WEL. A particle which is enriched of carbon and manganese, and depleted of silicon, is observed. The quantification of the atomic concentration in an area across the particle is shown in Fig. 4.11(b). The carbon concentration of the particle is 25 at%, indicating the particle to be cementite. The manganese significantly enriches in the cementite, ~ 6.7 at%, and is close to the equilibrium concentration at low temperature, e.g. 200 °C, from Thermo-Calc estimation. The silicon is enriched in the ferrite, which also accords to the equilibrium concentration in the pearlitic ferrite.

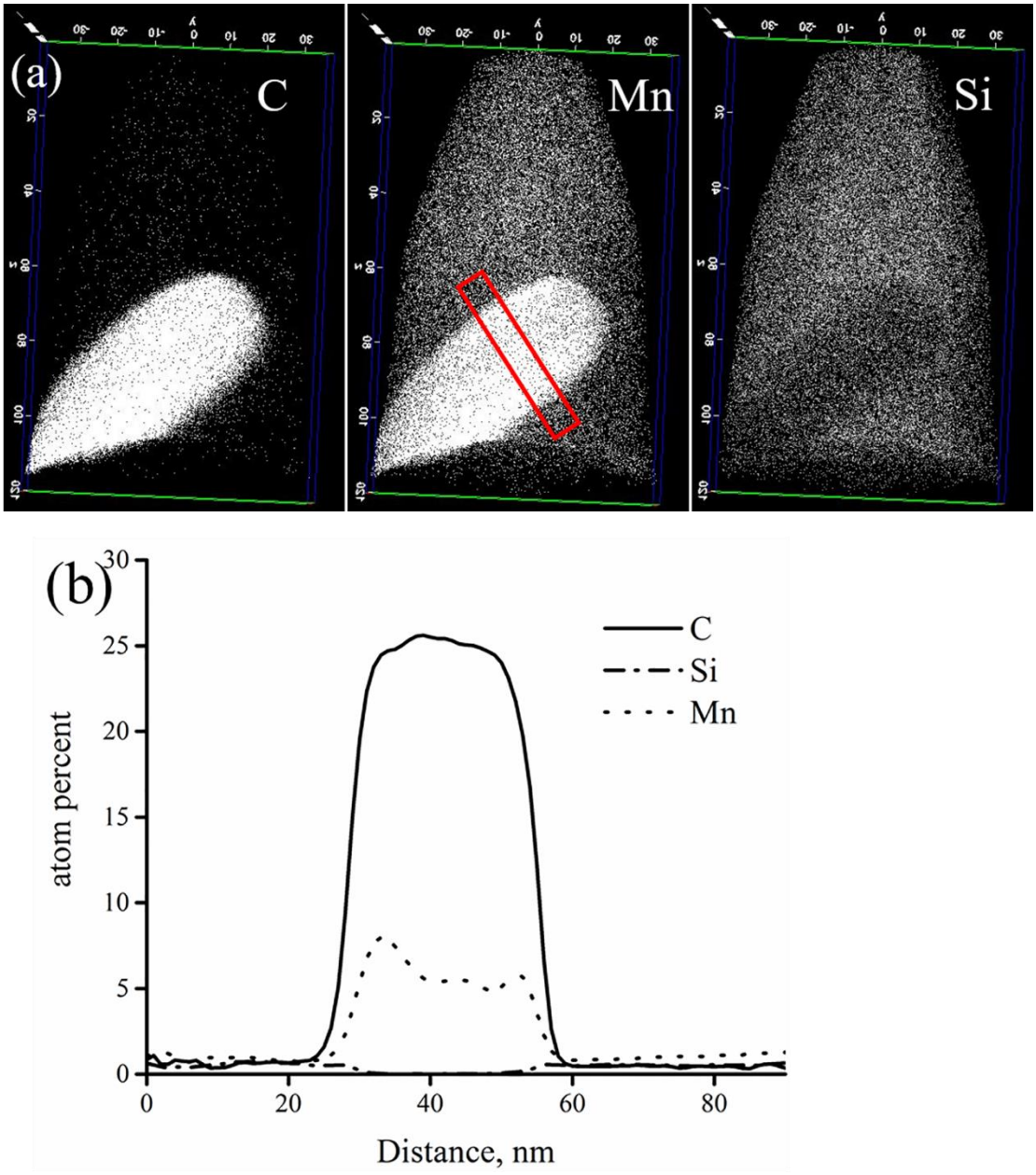

Fig. 4.11: The 3D element maps in the APT needle taken from pearlite ~3 μm beneath WEL (a) and the composition quantifications of volumes in the empty rectangle is shown in (b).

Fig. 4.12 shows the analysis of an APT needle extracted about 2 μm beneath the rail surface, equivalent to the surface WEL. Manganese and silicon are homogeneously distributed while carbon segregation can be observed. The carbon content that corresponds to the segregation site can be up to ~ 9.5 at%, while the matrix has a carbon concentration of around 2 at%.

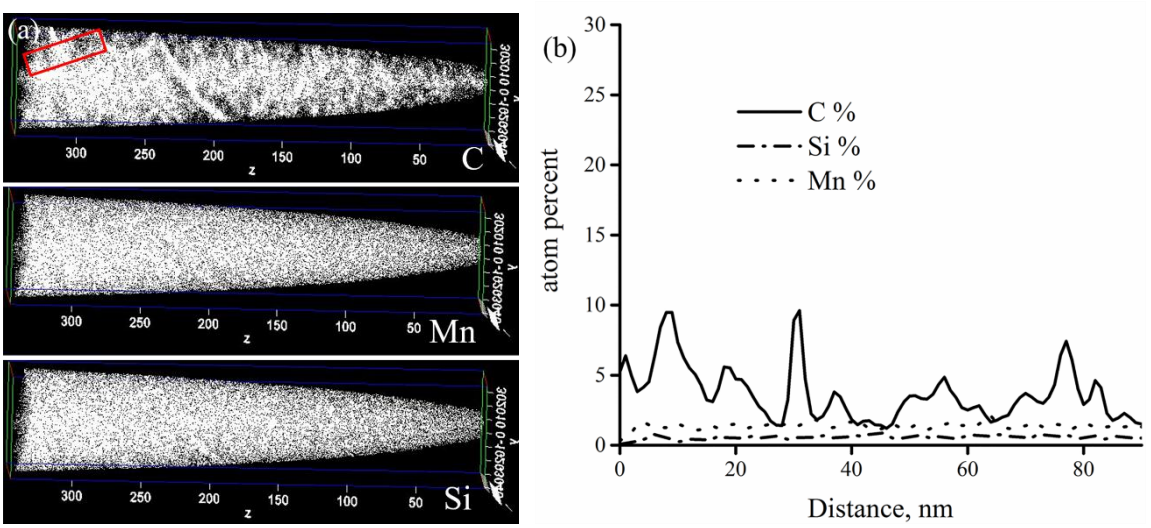

Fig. 4.12: The 3D element maps of APT needle taken in WEL, ~2 μm beneath the rail surface (a) and the composition quantifications of volumes in the empty rectangle in (b).

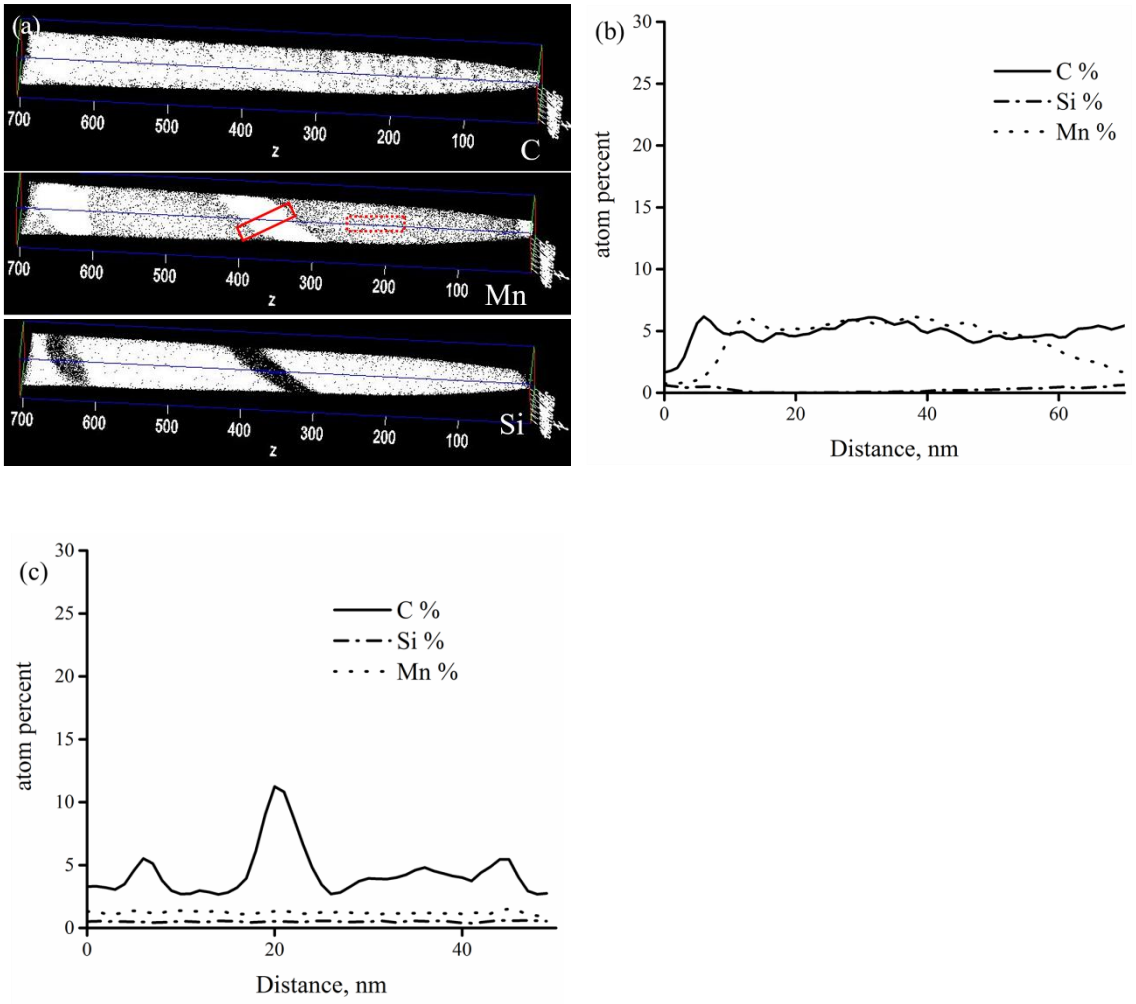

Fig. 4.13: The 3D element maps of APT needle taken in WEL, ~10 μm beneath rail surface (a) and the composition quantifications of volumes in the solid rectangle, in (b), and the dotted rectangle in (c) respectively.

Fig. 4.13 shows the analysis of an APT needle extracted about 10 μm beneath the rail surface, equivalent to the central WEL. The manganese-rich and silicon-poor zones indicate locations of previous cementite. However, the carbon segregation at the manganese-rich zone is not pronounced and the carbon distribution through the whole APT tip appears to be more homogeneous than that of manganese and silicon. The composition profiles in the manganese-rich zones show a carbon concentration of ~ 5 at%. Such concentration is higher than the average 3 at% (0.67 wt%) for the overall carbon concentration for the studied R260 Mn grade rail steel but is significantly lower than the 25 at% for cementite. The composition profile of an area without the manganese-rich zone is shown in Fig. 4.13(c). A carbon concentration spike of 10 at% is identified. Both quantifications indicate that carbon enrichment occurs in areas at and outside the original cementite locations.

Fig. 4.14 shows the carbon, manganese and silicon profiles of a needle in the WEL near the WEL/pearlite boundary, equivalent to the interface WEL. A lamella, enriched in carbon and manganese and depleted in silicon, is identified. The quantification within the red rectangle in Fig. 4.14(a) is shown in Fig. 4.14(b). A carbon concentration of 25 at% for cementite is quantified, whereas the cementite border is more diffuse than of cementite in the matrix in Fig. 4.11(b).

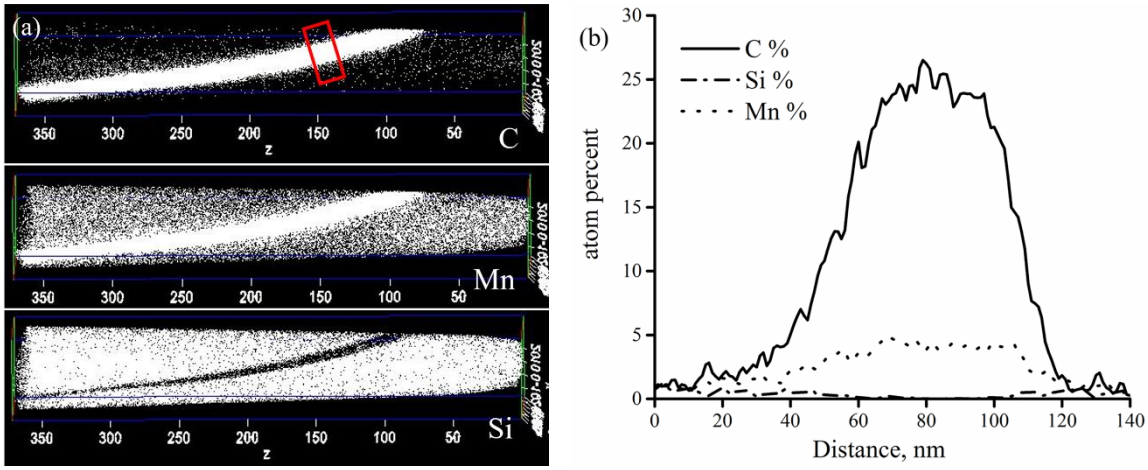

Fig. 4.14: The 3D element maps of APT needle taken in WEL and close to the WEL/pearlite boundary (a) and the composition quantifications of volumes in the solid empty rectangle (b).

4.4. Discussion

4.4.1. The complex microstructure in the WEL

The applied methods consistently identify the characterized WEL as a martensite microstructure. First, the common detection of retained austenite by XRD in Fig. 4.2, EBSD in Fig. 4.3(a) and TKD in Fig. 4.5(a) – (c) is strong evidence of martensite nature of WEL, e.g. [3]. The slight asymmetric profiles at $\{2\ 0\ 0\}_\alpha$ and $\{1\ 1\ 0\}_\alpha$ peaks in Fig. 4.2 indicate minor lattice tetragonality, expected from martensite with the average ~ 0.67 wt% carbon in the studied rail steel. Secondly, the identified nano-twinning in the WEL, Figs. 4.7(a) and (b) and Fig. 4.8, can be well expected in martensite, as is shown in martensite

produced by applying heat treatment to rail steels with a similar rail composition as in this study, e.g. by laser treatment in [17,18]. Finally, the redistribution of manganese is an important indication of high temperature increase in rails, possibly up to 1400 °C [6]. The similar procedures of temperature calculation from the manganese profile in ref [6]is used in this chapter and will be explained in detail in section 4.2.

The martensite in WEL shows heterogeneous morphology and complex compositional characteristics along rail depth, as revealed by TEM and APT. The martensite in the topmost surface WEL lamellae consists of nano-twinned substructures with a very high dislocation density, Fig. 4.8(a). No cementite is identified during indexing the selected area diffraction pattern. The manganese and silicon profiles in the APT needles from this region, Fig. 4.12, are homogeneous while the carbon profile shows nano-segregation, with a maximum C content up to 9 at%. This is significantly different from the APT map in the pearlite regions underneath the WEL in Fig. 4.11, indicating a redistribution of manganese and silicon during wheel passages. The carbon spikes in Fig. 4.12 can be up to 9.5 at% and are frequently identified in other areas in the same APT needle. Such high carbon concentration is difficult to be accommodated by dislocations only but can also be accommodated by grain boundaries, twins [30] and retained austenite [31]. The distance between the carbon spikes is typically 5 – 30 nm, which is much smaller than the measured martensite grain size in TKD, Fig. 4.7(a), or EBSD, Fig. 4.3(b). In addition, retained austenite may also accommodate carbon, but its low fraction, no more than 6%, could not explain the so frequent observations of the carbon spikes. Consequently, the most significant carbon spikes are considered to be accommodated at martensite twins.

The martensite morphology in the center of WEL thickness, Fig. 4.8, is similar to that in surface WEL in Fig. 4.7, i.e. with nanotwinning and dislocations. However, the compositional profile is different in the central WEL. The manganese-rich and silicon-poor zones remain observable in the APT needle, Fig. 4.13, while the carbon concentration at the identical zones is much less than the equilibrium 25 at% for cementite. Consequently, these zones are likely to correspond to the original cementite sites. Furthermore, there is absence of clear correlation between the carbon spikes and the manganese-rich zones, e.g. Fig. 4.13 (b) and (c), indicating carbon redistribution in the WEL. Finally, the microstructure morphology in the bottom of WEL is totally different from the one observed in the center and surface WEL. Untransformed cementite is recognized, both by electron diffraction and APT, and appears fragmented. This probably corresponds to the observed lamellar traces in the TKD map at the similar depth (Fig. 4.5(c)), in which cementite is unidentified due to the fact it was not included in the phase list for indexation with TKD.

The characterized WEL is different from the ones reported in [5,6], in which the WEL was studied by a combination of APT and TEM, like in this study. First, the identified nano-twinning substructure in this work, e.g. Fig. 4.7, is not reported in [5,6]. Secondly, the grain structure is different. Zhang et al. [5] identify nano-size grains in the top part of the WEL by recognizing a ring diffraction pattern and in the dark field TEM image. In the bottom of the WEL, they recognize fragmented cementite by electron

diffraction. Such fragmented cementite is also observed in the bottom of the investigated WEL, Figs. 4.9(a–d). However, the nano-sized grains are not observed in the topmost WEL in Figs. 4.7(a) and (b), since the ring pattern is not observed. Referring to the proposed hypothesis of WEL formation by phase transformation in this study, the fragmented cementite can be due to heterogeneous nucleation and growth of austenite at the ferrite/cementite phase boundaries.

The APT analysis of WEL in Figs. 4.12 – 4.15 is similar to the observation in [6]. Takahashi et al. [6] recognize zones with homogeneous manganese distribution and carbon enriched zones without manganese clustering in a WEL, which they conclude to be martensite formed via phase transformation. Such observations are made in the current APT work in Figs. 4.12 and 4.13, and the same conclusion regarding WEL can be more convincing with the additional observations of martensite morphology and the detected austenite phase in the WEL by TEM, EBSD and TKD. It should be noted that the TEM images in [6] do not show cementite lamellae in the WEL as the ones observed in the current study in Figs. 4.9 and 4.10. Zhang et al. [5] recognize a heterogeneous carbon distribution in the APT tip, without showing the profile of manganese. Consequently, it is impossible to correlate the carbon clusters to the sites of the original cementite. In short, the characterized WEL is different in both microstructure morphology and the compositional characteristics from the literature.

The combined characterization work, using EBSD and TKD, offers extra insight into the formation of the studied WEL. First, EBSD enables a larger overview of the WEL than for example TEM, considering the difference in sample size and the scanned area. It reveals coarse grains in the WEL, up to 4 μm. Complimentary to the EBSD scans, the TKD measurements also quantify micron size grains. Such grain size is much larger than those measured in other studies by TEM [5,6] or XRD [7], in which the grain size hardly exceeds 700 nm. Secondly, the KAM measured in the matrix beneath the WEL shows comparable misorientation profile as that of pearlite in an undeformed area. This indicates negligible deformation in the zones and is in accordance with the absence of transient work-hardened zone below the WEL as was shown by hardness measurement in [17]. As a result, the EBSD and TKD analyses support the hypothesis of WEL formation via martensite phase transformation.

4.4.2. Temperature estimation by shape analysis

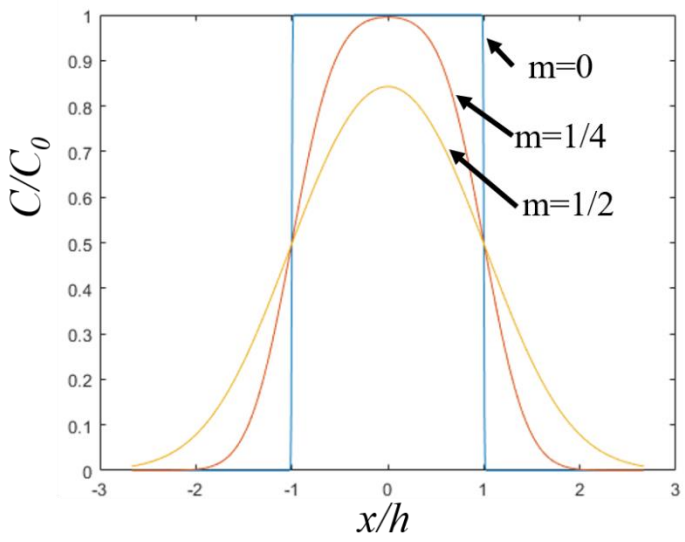

Fig. 4.15: Schematic drawing of shape analysis of manganese profile. The C and C_0 represent the manganese concentrations in both WEL and pearlite cementite. The *x*/*h* is the ratio of manganese diffusion distance to the original cementite width and the numbering, m, represents the ratio of diffusion length to the zone width. Details see main text.

The temperature changes in the studied rails can be estimated via the shape analysis of the manganese profile in the WEL, e.g. [4]. The manganese diffusion can be described by Fick's law, using error functions:

$$\frac{C}{C_0} = 0.5\left\{\mathrm{erf}\left(\frac{1-\frac{x}{h}}{\frac{\sqrt{Dt}}{h}}\right) + \mathrm{erf}\left(\frac{1+\frac{x}{h}}{\frac{\sqrt{Dt}}{h}}\right)\right\}$$

in which C and C_0 are the manganese concentration after diffusion and at the initial stage. $\boldsymbol{x}$ is the distance, D is the diffusion coefficient of manganese in austenite, t is the diffusion time and h is the thickness of the cementite lamella.

Due to the elevated temperature and the contact time, the original steep manganese profile in pearlite can become diffusive due to Mn diffusion in austenite. The Mn diffusivity depends on the temperature and the time allowed for the diffusion to occur. Fig. 4.15 schematically shows the changes of manganese profile, with an initial composition C_0 and a width of $2h$, due to diffusion. The variable m for each line corresponds to $\frac{\sqrt{Dt}}{h}$. The Mn diffusion co-efficient in austenite is calculated by $D = D_0 \times \exp(-\frac{Q}{RT})$, in which D_0 is the prefactor, 2.34×10^{-5} m^2/s, and Q is the activation energy, 2.61×10^5 J/mol [4]. The time, t, specifically refers to the duration when Mn diffuses in the austenite, i.e. when the temperature is above the A_1, and is estimated by $(T - A_1)/v$, in which A_1 is 700 °C (973 K) and the heating rate v is 1.5×10^6 °C/s [3]. The estimated manganese concentrations from APT tips are shown in table 2.

It is worthwhile to point out that the reference manganese peak concentration, used for calculating the manganese diffusion distance, is chosen from the measured cementite only. The manganese concentration in cementite can differ among lamellae due to different forming conditions and the manganese diffusion distance in the WEL, thus the subsequently required temperature for the diffusion distance, can be affected. The value of *m* for the surface WEL is approximately ½, which corresponds to a maximum temperature of approximately 1400 °C.

It is further worthwhile to point out that the temperature estimation from the shape analysis in this section is indicative. First, the Mn profile of cementite in the matrix pearlite, Fig. 4.11(b), is used as the starting profile in Fig. 4.15, i.e. when *m* is 0. However, the Mn profile in Fig. 4.11(b) does not show the identical rectangle shape for $m = 0$ in Fig. 4.15. Instead, the determined value *m* corresponding to the Mn profiles at a different depth within the WEL is an approximation, by comparing the degree of changes in the Mn profile to the one in the matrix pearlite. Second, current calculation only considers a single wheel passage. The WEL in rails are expected to form after multiple wheel passage, during which the Mn diffusion distance in austenite can accumulate as well. For example, the Mn can diffuse ~ 8.8 nm at 1400 °C, calculated by following the approach used in this section. The same diffusion distance requires ~ 2500 wheel passes, assuming that an identical temperature of 730 °C is reached during each wheel passage. Note that 730°C should be regarded as a lower limit, since at lower maximum temperatures no austenite would form, which is in contradiction with the experimental evidence of retained austenite. The calculated 2500 wheel passages is not comparable with the 1.2 million wheel passages, imposed on the studied rail track. However, not each wheel passage necessarily contributes to the temperature increase above the austenitization temperature at the rail surface due to the differences in the loading conditions during the individual wheel/rail contact. In addition, the evolution of the WEL during the train wheel passages can be complex since it may be worn away as wear debris and new WEL forms during the subsequent wheel passages As a result, the calculated temperature in Table. 2 is to indicate the significant temperature increase at the rail surface during the wheel/rail contact.

Table.2 Quantified manganese concentration from needles at different depth in the WEL and in the pearlite matrix

Region	Position, μm	Mn peak concentration, at%	Shape	Estimated T (°C)
Surface WEL	5	4.10	Diffuse	~ 1400
Interface WEL	23	5.32	Slightly diffused	< 1150
Pearlite	26	5.44	Non-diffused	

4.4.3. Formation Mechanism of the Multi-Layered Structure Characterizing Martensite in the WEL

It is expected that the passing trains cause simultaneous deformation and frictional heat on the rails. The deformation is indicated by the high KAM in the EBSD scan on the WEL, which can be due to localized

crystal lattice distortion. The KAM profile in the pearlite immediately beneath the WEL indicates negligible deformation in this zone. The abrupt change of KAM profile from WEL to the pearlite underneath indicates that the thermally-induced martensitic transformation is the dominant contribution to the formation of the studied WEL.

In situ observation of the exact WEL formation mechanism is impossible, due to practical limitations associated with the complex loading conditions of the wheel/rail contact. However, the principal formation mechanism of the multi-layered structure martensite in the studied WEL, e.g., Figs. (4.7–4.10) and Figs. (4.12–4.14), can be interpreted on the basis of phase transformation theory. The identified morphological and compositional characteristics of martensite in the APT tips and TEM lamellae, extracted at different depths in the WEL, are attributed to variations in the thermal history at the corresponding positions.

According to the hypothesis attributing WEL formation to martensitic phase transformation, the initial pearlitic microstructure in the rails transforms to austenite when the rail surface is heated to very high temperatures (i.e., austenitized) by the train wheels. The austenite subsequently transforms to martensite due to the rapid cooling after the train passes. On the one hand, the chemical composition and microstructures of the product martensite depend on the composition of the parent austenite [30]. On the other hand, the austenite composition depends on the characteristics of the pearlite to austenite transformation. An understanding of the pearlite to austenite transformation process is therefore essential for interpreting the multi-layered structures of the martensite in the characterized WEL.

The final characteristics of the WEL are imparted during multiple wheel passages. In this process, the pearlite to austenite transformation is followed by martensite formation during cooling. The martensite serves as the initial microstructure for the subsequent phase transformation cycles. In the literature, the reverse martensite to austenite transformation is widely considered compositional invariant, i.e., the parent and product phases have the same composition.

The pearlite to austenite transformation is considered a diffusional process [31], characterized by the redistribution of carbon between the initial phases and austenite. Moreover, manganese partitioning between ferrite/cementite and austenite, albeit on a very fine scale that is observable via high-resolution characterization only, is typical of this transformation. These diffusional processes are temperature- and time-dependent and the ferrite and cementite to austenite transformation may be incomplete if carbon diffusion in austenite is limited, e.g., due to the limited diffusion time during fast heating and the use of temperatures residing in the lower range of the austenite phase region [17,31].

Simulations show that the most favorable conditions for the pearlite to austenite transformation occur at the rail surface, where the temperature is highest [17]. The temperature decreases rapidly from the surface to the rail center. As a result, compared with the region closer to the rail center, the surface region experiences higher temperatures and longer dwelling times within the austenite temperature range. This implies that the diffusion distances are longer and consequently carbon and manganese are more homogeneously distributed in the surface than in the center. The compositional characteristics of the

APT tip from the bulk pearlite (see Fig. 4.11) are compared with those of the tips from different depths in the WEL. A clear tendency for manganese and carbon segregation with increasing depth in the WEL is revealed. The absence of the 25 at% carbon zone from the rail-surface tip (see Fig. 4.12) and the WEL-center tip (see Fig. 4.13) indicates the full dissolution of cementite. Therefore, an overall steel carbon concentration of 0.67 wt.% is assumed for the austenite. Martensite with this carbon concentration is expected to have a twinning substructure with high dislocation density, similar to those observed for the surface WEL and the center WEL (Figs. 4.7–4.8). However, due to the local conditions, less diffusion occurs at the bottom of WEL (than at the top). Therefore, the pearlite is only partly transformed to austenite and cementite persists, as revealed via TEM (Figs. 4.9–4.10) and APT (Fig. 4.14).

4.5. Summary and conclusions

A systematic characterization has been done on WEL in an R260 Mn grade rail steel, with XRD, EBSD, TKD, TEM and APT. The conclusion that WEL forms via martensitic phase transformation is based on the identified retained austenite by XRD, EBSD and TKD and the martensite microstructure revealed by TEM. A complex multi-layer structure in WEL was revealed by TEM and APT. The WEL close to the rail surface has a microstructure of nano-twinned martensite with high dislocation density. The bottom side of WEL consists of ferrite and untransformed cementite and high dislocation density. The manganese diffusion from the APT analysis is strong evidence for the significant temperature increase which allows the WEL to form. The observed microstructure fits well with the suggested phase transformation mechanisms.

EBSD and TKD are shown to be useful complementary tools in characterizing and tracing the origin of WEL. They quantify grain size in the WEL as 20 nm – 4 μm and the hypothesis of WEL formation via severe plastic deformation only is thus excluded. The KAM measurement has been widely used to study the local misorientation due to plastic deformation. This measure reveals differences of deformation scales in the WEL and the matrix pearlite. The comparison of KAM in the WEL, the pearlite immediately beneath WEL and the WEL shows a secondary contribution of deformation to the formation of WEL.

References

[1] Dikshit V, Clayton P, Christensen D. Investigation of rolling contact fatigue in a head-hardened rail. Wear 1991;144:89–102.

[2] Baumann G, Fecht HJ, Liebelt S. Formation of white-etching layers on rail treads. Wear 1996;191:133–40.

[3] L. WÖRHPAW. Investigation of white etching layers on rails by optical microscopy, electron microscopy, X-ray and synchrotron X-ray diffraction. Mater Sci Eng A 2001;303:150–7.

[4] Wild Wang, L., Hasse, B., Wroblewski, T. , Goerigk, G., Pyzalla, A. E. Microstructure alterations at the surface of a heavily corrugated rail with strong ripple formation. Wear 2003;254:876–83.

[5] Zhang HW, Ohsaki S, Mitao S, Ohnuma M, Hono K. Microstructural investigation of white etching layer on pearlite steel rail. Mater Sci Eng A 2006;421:191–9.

[6] Takahashi J, Kawakami K, Ueda M. Atom probe tomography analysis of the white etching layer in a rail track surface. Acta Mater 2010;58:3602–12.

[7] Lojkowski W, Djahanbakhsh M, Bürkle G, Gierlotka S, Zielinski W, Fecht HJ. Nanostructure formation on the surface of railway tracks. Mater Sci Eng A 2001;303:197–208.

[8] Newcomb SB, Stobbs WM. A transmission electron microscopy study of the white-etching layer on a rail head. Mater Sci Eng 1984;66:195–204.

[9] Ishida M. Rolling contact fatigue (RCF) defects of rails in Japanese railways and its mitigation strategies. Electron J Struct Eng 2013;13:67–74.

[10] Steenbergen M, Dollevoet R. On the mechanism of squat formation on train rails – Part I: Origination. Int J Fatigue 2013;47:361–72.

[11] Pal Valente, C., Daniel, W., Farjoo, M. S, Pal S, Valente C, Daniel W, Farjoo M. Metallurgical and physical understanding of rail squat initiation and propagation. Wear 2012;284–285:30–42.

[12] Clayton P. Tribological aspects of wheel-rail contact: a review of recent experimental research. Wear 1995;191:170–83.

[13] Carroll RI, Beynon JH. Rolling contact fatigue of white etching layer: Part 1. Crack morphology. Wear 2007;262:1253–66.

[14] Carroll RI, Beynon JH. Rolling contact fatigue of white etching layer: Part 2. Numerical results. Wear 2007;262:1267–73.

[15] E. A. LWPASWW. Microstructure features on rolling surfaces of railway rails subjected to heavy loading. Mater Sci Eng A 2003;359:31–43.

[16] Lojkowski W, Millman Y, Chugunova SI, Goncharova I V., Djahanbakhsh M, Bürkle G, et al. The mechanical properties of the nanocrystalline layer on the surface of railway tracks. Mater Sci Eng A 2001;303:209–15.

[17] Wu J, Petrov RH, Naeimi M, Li Z, Dollevoet R, Sietsma J. Laboratory simulation of martensite

formation of white etching layer in rail steel. Int J Fatigue 2016;91:11–20.

[18] Österle Rooch, H., Pyzalla, A., Wang, L. W, OeSterle W, Rooch H, Pyzalla A, Wang L, Österle W, et al. Investigation of white etching layers on rails by optical microscopy, electron microscopy, X-ray and synchrotron X-ray diffraction. Mater Sci Eng A 2001;303:150–7.

[19] Griffiths BJ. White Layer Formations at Machined Surfaces and Their Relationship to White Layer Formations at Worn Surfaces. J Tribol 1985;107:165.

[20] Hosseini SB, Klement U, Yao Y, Ryttberg K. Formation mechanisms of white layers induced by hard turning of AISI 52100 steel. Acta Mater 2015;89:258–67.

[21] Umbrello D, Rotella G. Experimental analysis of mechanisms related to white layer formation during hard turning of AISI 52100 bearing steel. Mater Sci Technol 2012;28:205–12.

[22] Todaka Y, Umemoto M, Tsuchiya K. Nanocrystallization in Carbon Steels by Various Severe Plastic Deformation Processes. Nanomater. by Sev. Plast. Deform., Wiley-VCH Verlag GmbH & Co. KGaA; 2004, p. 505–10.

[23] Trimby PW. Orientation mapping of nanostructured materials using transmission Kikuchi diffraction in the scanning electron microscope. Ultramicroscopy 2012;120:16–24.

[24] Trimby PW, Cao Y, Chen Z, Han S, Hemker KJ, Lian J, et al. Characterizing deformed ultrafine-grained and nanocrystalline materials using transmission Kikuchi diffraction in a scanning electron microscope. Acta Mater 2014;62:69–80.

[25] Linz M, Cihak-Bayr U, Trausmuth A, Scheriau S, Künstner D, Badisch E. EBSD study of early-damaging phenomena in wheel–rail model test. Wear 2015;342–343:13–21.

[26] Wu J, Petrov RH, Naeimi M, Li Z, Sietsma J. A Microstructural Study of Rolling Contact Fatigue in Rails. Proc. Second Int. Conf. Railw. Technol. Res. Dev. Maintenance, Ajaccio, Fr. 8-11 April 2014, Civil-Comp Press; 2014.

[27] JCPDS-International Center for Diffraction Data (2014), Diffrac EVA, Version 4.1 .

[28] Hofer C, Bliznuk V, Verdiere A, Petrov R, Winkelhofer F, Clemens H, et al. Correlative microscopy of a carbide-free bainitic steel. Micron 2016;81:1–7.

[29] Zhou DS, Shiflet GJ. Ferrite: Cementite crystallography in pearlite. Metall Trans A 1992;23:1259–69.

[30] Miller MK, Beaven P a, Brenner SS, Smith GDW. An Atom Probe Study of the Aging of Iron-Nickel-Carbon Martensite. Metall Mater Trans A 1983;14:1021–4.

[31] Miller MK, Beaven P a., Smith GDW. A Study of the Early Stages of Tempering of Iron-carbon Martensites by Atom Probe Field Ion Microscopy. Metall Trans A 1981;12:1197–204.

Chapter 5 Laboratory simulation of martensite formation of white etching layer in rail steel

Abstract:

White etching layer (WEL) is a frequently observed microstructural phenomenon in rail surface, formed during dynamic wheel/rail contact. It is considered as one of the main initiators for rolling contact fatigue cracks. There are several hypotheses for the formation mechanism of WEL. However, due to the complicated wheel/rail contact conditions, none is directly proven. Currently, the most popular hypotheses refer to either formation of martensitic WEL by phase transformations or formation of nanocrystalline ferritic WEL by severe plastic deformation. In Chapter 4, the phase transformation mechanism was shown to be the most possible for the studied rail steel. In this work, WEL formation by martensitic transformation in R260Mn grade pearlitic rail steel was simulated by fast heating and quenching experiments. The contribution of plastic deformation in the martensite formation was studied by applying simultaneous loading and heating. Microstructural characteristics of the simulated WEL and WEL observed in a field rail specimen were characterized by microhardness, optical microscopy, scanning electron microscopy and electron backscatter diffraction. Microstructures of simulated WELs and rail WEL were compared and similarities in morphology are identified. Plastic deformation is found to promote martensite formation. Numerical simulation shows the possible temperature rise up to austenitizing temperatures. Combining comparisons of experimental simulation with the observation of WEL in the rail and the thermodynamic calculations, the hypothesis for WEL formation via martensitic transformation is supported.

Keywords: white etching layer; martensite formation; laboratory simulation; temperature rise; thermodynamic calculations[2]

[2] The chapter is based on a scientific paper:
Wu J, Petrov RH, Naeimi M, Li Z, Dollevoet R, Sietsma J. Laboratory simulation of martensite formation of white etching layer in rail steel. Int J Fatigue 2016;91:11–20.

5.1. Introduction

Rolling contact fatigue (RCF) is the dominant damage mechanism in rails and has attracted wide scientific interest. The high and repetitive external load, exceeding 1 GPa, leads to the formation of peculiar surface structural alterations, surface crack formation and spallation [1,2]. One such specific structural phenomenon in rail surface is widely named white etching layer (WEL) [1–7]. WEL is commonly recognized as a thin and hard layer, which appears white under light reflection after being etched in 2 to 5% HNO_3 in ethanol (Nital etchant). The widely accepted opinion is that the extremely high hardness of WEL, up to 1200 HV [6], is related to its brittleness. RCF cracks associated with WEL are frequently observed in rails [2].

The most popular hypotheses for WEL formation are: *(i)* martensite formed after the rail surface is heated up to austenitization temperatures and subsequently quenched, e.g. [8], and *(ii)* nanocrystalline ferrite as a result of severe plastic deformation [4]. A brief summary of the above two proposed mechanisms is given in Table 1. There is experimental evidence for the WEL formation via martensite phase transformation. In synchrotron X-ray diffraction (XRD) experiments, the WEL is shown to consist of bcc iron and the tetragonal crystal lattice distortion is identified [8,9]. This is a typical feature for high carbon martensite. Detection of retained austenite [8,9] indicates martensitic nature of the WEL to be the most probable. Occasionally, the martensite type features, such as the lath morphology [7] and the micro-twinning substructure [8], are observed in WEL by means of transmission electron microscopy (TEM). Martensite with similar hardness as WEL in [8] can be simulated by laser heat treatment. Takahashi studied WEL in rails using a combination of microhardness, scanning electron microscopy (SEM) and atom probe tomography (APT) [7]. He claimed the absence of severe plastic deformation in the studied rail, from the observation of unchanged cementite interlamellar distance in the rail surface pearlite and the absence of work-hardened pearlite zone beneath the WEL. In addition, identification of manganese diffusion, from cementite to the ferrite lamellae in the WEL by means of APT indicates a strong temperature rise caused by wheel/rail contact. This evidence tends to conclude that WEL is formed by martensitic phase transformation.

However, calculations of temperature rise caused by wheel/rail contact do not support the martensitic transformation for the WEL formation in [9,10]. Reaching the austenitizing temperature, e.g. 727˚C for the eutectoid steel, has been shown to be improbable. Instead, observations of possible deformation twinning in the WEL and the work-hardened pearlite zone below WEL have been made [10,11]. In addition, pearlite after severe plastic deformation is shown to contain similar features as the WEL, such as cementite dissolution, nanometer grains and high hardness [4]. Differential Scanning Calorimetry (DSC) scans reveal a similar decomposing behavior of the WEL and the pearlite after mechanical alloying [4], indicating a similar microstructure type. The extremely high dislocation density in the WEL

is estimated to be able to accommodate the amount of carbon from the dissolved cementite. As a result, WEL formation due to plastic deformation is proposed [4,10,11].

Table.1 Summary of the formation mechanisms of the white etching layer

Proposed mechanism	Supporting evidence
WEL formed by martensitic transformation	Detection of tetragonality and retained austenite in WEL by synchrotron XRD [8,9]. Martensite like morphology in WEL revealed by TEM, e.g. micro-twinning [8] or lath-like morphology [7]. Simulation of martensite with similar hardness as WEL by laser heating experiment [8]. Absence of transient work-hardened pearlite zone below WEL by hardness measurements and no observation of cementite lamellae thinning from APT results [7]. Manganese diffusion revealed by APT [7].
WEL formed by plastic deformation	Temperature calculation does not support martensite transformation mechanism for WEL formation in [9,10]. Observation of deformation characteristics in WEL and the pearlite beneath WEL [10,11]. Reproduction of WEL by severe plastic deformation [4,11]. Similar thermal stability of the WEL and nanocrystalline ferrite formed by mechanical alloying, using DSC [4].

In this study, WEL formation by martensitic transformation mechanism is simulated in laboratory conditions. The WEL formed by martensitic transformation must be a product of (ultra)fast phase transformation because of wheel/rail contact. According to [7], the heating rate generated during train passage can be higher than 10^6 ºC/s to the temperature where austenite forms. After train passage, the austenite transforms to martensite during fast cooling. Due to the extremely short wheel/rail contact time, estimated to be milliseconds using the heating rate of 10^6 ºC/s from room temperature to 727 °C for the eutectoid iron steel, it is almost impossible to measure the actual temperature changes during the period. On the other hand, fast heating and quenching heat treatment can be simulated and controlled using laboratory instruments, such as dilatometer and thermo-mechanical simulator. The latter instrument also provides accurate loading controls, such as (high) strain rate, which is more suitable to simulate the combined thermal and mechanical situation of wheel/rail contact. In this study, WEL formation by fast phase transformation mechanism is simulated by the thermo-mechanical simulator. The microstructural features are characterized and compared with WEL observed in rails. The similarity of the laboratory WEL and WEL in rails will be discussed on the basis of the current observations and comparison with the literature.

5.2. Materials and methods

R260Mn grade rail steel, cut from a straight rail track [12], was investigated. The steel has a composition of Fe-0.67 wt% C-1.51 wt% Mn-0.21 wt% Si, with a nearly fully pearlitic microstructure. The average pearlite colony size is 20 μm and the average cementite interlamellar distance is 150 nm. For WEL formation in laboratory conditions, cylindrical samples of ø6 mm × 75 mm were cut from the bottom of the railhead, where the materials are considered to be free of plastic deformation from train passages. Thermocouples were welded in the specimen center to measure the temperature changes during the experiments, Fig. 5.1(a). The samples were subjected to fast heating and quenching treatment by a Gleeble 1500 thermo-mechanical simulator. The specimens were quickly heated to temperatures between 730 ºC and 930 ºC, see Fig. 5.1(b). Heating rates of 20 ºC/s and 200 ºC/s were used to carry out the experiments. After heating to the selected temperature, the specimens were immediately quenched at a rate of 67 ºC/s, using helium gas, to transform austenite to martensite. It will be shown that austenite forms after being heated to the designed temperatures.

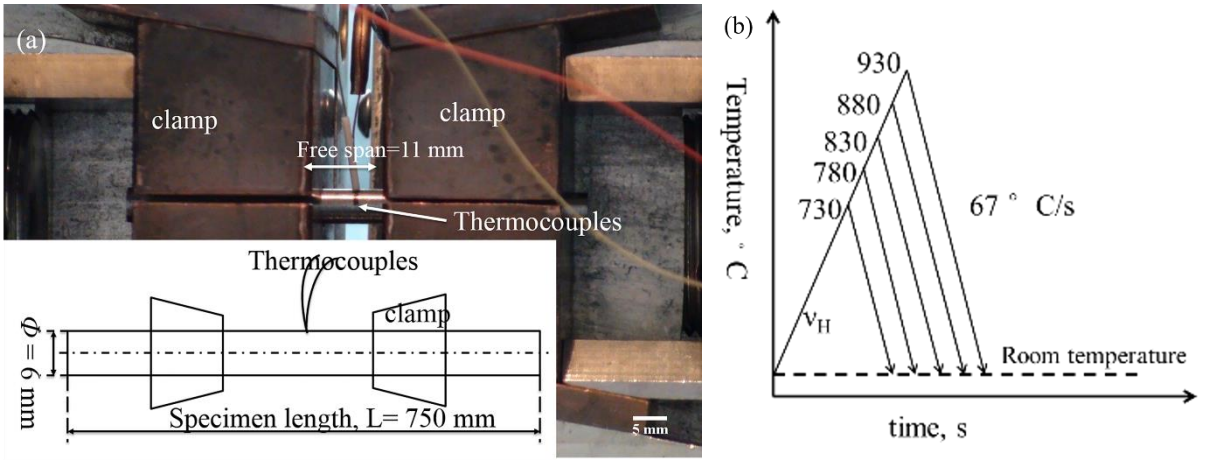

Fig. 5.1 (a) Configuration settings of Gleeble 1500 used in the laboratory simulations. The inset in the left bottom of the figure schematically shows the dimensions of the specimen and the position of the thermocouple. The two parallel arrows in the inset indicate the position where the specimen for microstructure characterization was cut after the heat treatment; (b) Schematic representation of heat treatments used for WEL formation simulation in laboratory conditions

In the following sections, the laboratory samples will be named '$S_{xxx\text{-}yyy}$', where letter S indicates the simulated sample and the first three symbols refer to the temperature samples are heated to (xxx °C) and the last three symbols are the heating rate (yyy °C/s）. For example, $S_{730\text{-}020}$ is the simulated specimen which is heated to 730 °C at the rate of 20 ºC/s. Additionally, rail samples, containing WEL, were also studied and will be named 'rail WEL' throughout this chapter.

It is expected that WEL in rails forms via combined contributions from plastic deformation and temperature increases. In order to study the role of plastic deformation on the martensite (WEL)

formation, the test $S_{730\text{-}200}$ with the identical specimen geometry as described earlier in this section was repeated while plastic deformation was applied simultaneously. The temperature of 730 °C was chosen because martensite with comparable morphology and hardness range to rail WEL was identified after fast heating and quenching tests. In the wheel/rail interaction, both compressive and shear stresses are expected but it is impossible to apply them simultaneously with the Gleeble thermo-mechanical simulator. Moreover, an accurate control of shear stress can be very challenging due to the possibility of sample slippage during the test. On the other hand, controlling compressive stress can be more accurate and a quantitative insight into the consequence of plastic deformation on the final simulated WEL can be obtained. From the finite element method output for the loading condition of the studied rail piece, a representative plastic strain of 0.3 % is used. The loading and the heating stop simultaneously upon reaching 730 °C, with a heating rate of 200 °C/s. In the subsequent section, the specimen tested with simultaneous heating and deformation will be noted as $S_{730\text{-}200\text{-}s}$.

The microstructures in both laboratory simulated samples and rail samples were characterized by microhardness tests, optical microscopy (OM) and scanning electron microscopy (SEM). After each heat treatment cycle, the specimens were cut transversely at the position where thermocouples were welded, see the inset in Fig. 5.1(a). The specimens for metallographic studies were prepared following the routine preparation procedure. A 2 vol% Nital etchant was used to reveal the microstructures. The microhardness was measured with a Durascan 70 (Struers) hardness tester, using a load of 1 N for 10 s. The microstructures were first characterized with an Olympus BX60M optical microscope. The samples were further analyzed with a Jeol 6500F SEM.

Electron Backscatter Diffraction (EBSD) measurements were done on the rail specimen containing WEL. Specimen $S_{730\text{-}200}$ was also analyzed by EBSD for comparison. The sample preparation procedure reported in [11] was used in the study. The EBSD measurements were carried out in a FEI Quanta-450 SEM equipped with a field emission gun (FEG) and Hikari-Pro, EBSD detector. EDAX-TSL OIM Data Collections v.6.2 was used for data acquisition. All measurements were performed with accelerating voltage of 20 kV, FEI-spot size of 5, a 40 µm final aperture, step size of 50 nm and a hexagonal scan grid mode. With these settings, ~90% of the orientation data points were correctly indexed with confidence index higher than 0.06. The orientation data were analyzed by means of TSL OIM Data analysis v. 7 without additional post-processing (cleaning) and the grains were defined as regions containing minimum 4 pixels with an internal misorientation less than 5°.

In order to provide the thermodynamic basis for the design of heat treatments and for the interpretation of the obtained results, the equilibrium quasi-binary iron-carbon phase diagram was calculated by Thermo-Calc® Windows (TCW™), version S. According to Ref [13], the peak normal pressure during wheel/rail contact in the new profile rail can reach 1.8 GPa, which affects the phase diagram [14]. In this work, the hydrostatic pressure of 1.8 GPa was used and its effect on the equilibrium phase diagram was evaluated using Thermo-Calc.

5.3. Results

5.3.1. Iron-carbon phase calculations

The calculated equilibrium quasi-binary iron-carbon (Fe-C) phase diagram under atmospheric pressure is shown in Fig. 5.2(a) and the one calculated under hydrostatic pressure of 1.8 GPa is shown in Fig. 5.2(b). The vertical dashed lines in both figures indicate the carbon concentration of the studied rail steel of 0.67 wt% C. In the equilibrium Fe-C phase diagram under atmospheric pressure for the present composition in Fig. 5.2(a), the minimum temperature for austenite to form, Ae_1, is 700 °C and temperature for full austenitization, Ae_3, is 722°C. Comparing with the classical pure Fe-C phase diagram, a three-phase zone, consisting of ferrite (α), cementite (θ) and austenite (γ), is recognized. The temperatures for the lower limit and the upper limit of the three-phase zone are the Ae_1 and 716 °C respectively.

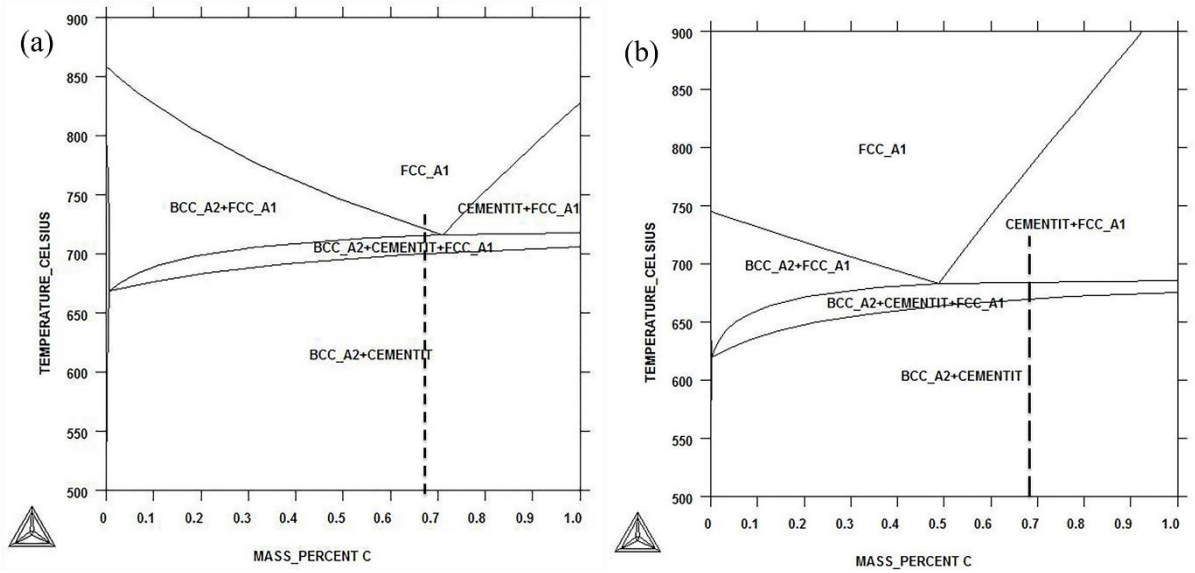

Fig. 5.2 Equilibrium quasi-binary iron-carbon phase diagram: (a) under atmospheric pressure, (b) under hydrostatic pressure of 1.8 GPa

The Fe-C phase diagram in Fig. 5.2(b), with a hydrostatic pressure of 1.8 GPa, is different from the one calculated under atmospheric pressure in Fig. 5.2(a). The most obvious difference is the shift of eutectoid carbon concentration from 0.71 wt% in Fig. 5.2(a) to 0.48 wt% in Fig. 5.2(b). The Ae_1 temperature is 670 °C and Ae_3 is 777 °C. Comparing with the diagram for atmospheric pressure in Fig. 5.2(a), the highest temperature for cementite to remain stable changes from 716 °C in Fig. 5.2(a) to 777 °C in Fig. 5.2(b) for the present composition. The shift in the eutectoid composition indicates that if hydrostatic pressure during wheel/rail contact is high enough, the rail composition shifted from (near) eutectoid to hypereutectoid and cementite will be stable in a wider temperature range under high hydrostatic pressure.

5.3.2. Microstructures of simulated WEL and the rail WEL

Fig. 5.3(a) shows an optical image of the rail WEL. The specimen was cut cross-sectional so that the trains traveled perpendicular to the observed plane. After etching with 2 % Nital, rail WEL is revealed as featureless white islands, separated by distinct boundaries from the brownish etched pearlite matrix. Some pearlite colonies are also etched white but can be identified by hardness measurements. The average thickness of the rail WEL is ~ 25 μm and the microhardness varies between 725 HV and 1050 HV. Immediately beneath the rail WEL, pearlite colonies appear intact and no flattening is recognized. The microhardness measurements in the pearlitic area under the rail WEL are close to the measurements in the original rail center, indicating the absence of work hardening.

Fig. 5.3(b) shows the microstructures, with mixed white and brown contrast under light reflection, in specimen $S_{730\text{-}020}$. The hardness of the brown region is ~290 HV, which is equivalent to the measured hardness of the central pearlite area in the studied rail section. The white area in Fig. 5.3(b) appears featureless for magnification up to 1000 x and is much harder, 670-810 HV, than the brown pearlitic area. The hardness of the white zone compares well with the hardness of martensite with the carbon content of ~0.67 wt% for the studied rail [8]. Accordingly, the hard white phase is considered to be martensite. In addition, within the white martensite blocks, some brownish regions can be observed, as indicated by arrows in Fig. 5.3(b). These regions are also identified as pearlite using SEM at higher magnification, see for example Fig. 5.4(c). Martensite formed in the other specimens, e.g. $S_{780\text{-}020}$ in Fig. 5.3(c) or $S_{930\text{-}020}$ in Fig. 5.3(d), appears grey and is unlike the white martensite in Fig. 5.3(b). The mixed microstructure of martensite and pearlite is formed for austenitizing temperatures up to 830 °C, with reducing fraction of untransformed pearlite. Microstructures of samples $S_{880\text{-}020}$ and $S_{930\text{-}020}$ are similar and one example of the microstructure of the sample $S_{930\text{-}020}$ is shown in Fig. 5.3(d). A single phase is observed, which is identified as martensite by means of hardness. Part of the martensite formed at these temperatures seems to have a needle-like shape. The grey particles in Fig. 5.3(d) are MnS inclusions, see our previous work [12]. Similar microstructures are observed in samples heated with 200 ºC/s. The fraction of martensite, formed at temperatures of 730 °C – 830 °C with the heating rate of 200 °C/s, is lower than those formed at the heating rate of 20 °C/s.

Both the lab simulated and field rail specimens were characterized by SEM. Fig. 5.4(a) shows the SEM micrograph of an area inside the rail WEL and at a micrograph taken at WEL/pearlite boundary is shown in Fig. 5.4(b). Two types of lamellar features in the rail WEL can be observed: *(i)* the lamellar with multidirectional morphology, Fig. 5.4(a); *(ii)* line lamellar with aligned features, as indicated by arrows in Fig. 5.4(b). The aligned morphology is more obvious in areas close to the rail WEL/matrix boundary in Fig. 5.4(b). Across the boundary, connections between cementite lamellae in pearlite and the aligned lamellae in the rail WEL are observed. Thus, the aligned lamellae in the WEL in Fig. 5.4(b) probably correspond to the previous locations of cementite. The distance between the aligned lamellae in rail WEL is similar to the cementite interlamellar distance in the adjacent pearlite. Occasionally, small isolated pearlite islands can be observed within the WEL, indicated by the open rectangle in Fig. 5.4(b).

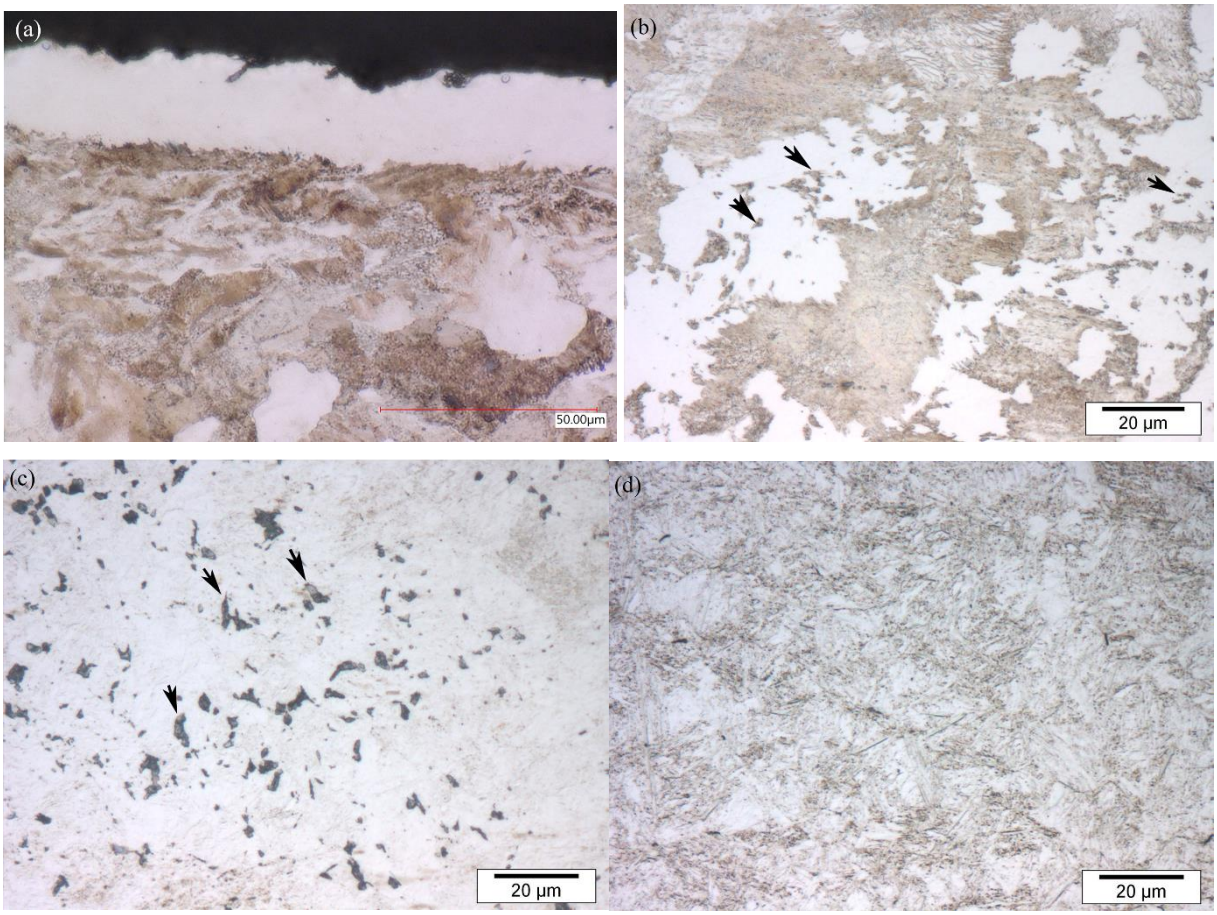

Fig. 5.3 Optical micrographs of: (a) rail WEL, and laboratory simulated specimen (b) $S_{730\text{-}020}$, (c) $S_{780\text{-}020}$ and (d) $S_{930\text{-}020}$. The arrows in (b) and (c) show untransformed pearlite within the martensite blocks.

Similar lamellar features are also observed in the laboratory formed WEL. Fig. 5.4(c) and (d) show SEM micrographs of laboratory specimen $S_{730\text{-}020}$. The dark grey zones in Fig. 5.4(c) and (d) are the martensite with no typical needle shape, as expected for a carbon concentration of 0.67 wt% in the studied rail steel. The similar lamellar features in Fig. 5.4(a) and (b) is recognized in Fig. 5.4(c) and (d), in the laboratory specimen $S_{730\text{-}020}$. The aligned line lamellae in the martensite in Fig. 5.4(d) also appear to continue from the adjacent lamellar cementite in the pearlite matrix. The distance of aligned line morphology in the martensite appears the same as the adjacent cementite. Some untransformed pearlite within martensite block, corresponding to the brownish areas in the white martensite block in Fig. 5.3(b), is recognized in Fig. 5.4(c). It is observed that the martensite formed in specimens heated to 780 ˚C and higher temperatures has the lath-like morphology and is significantly different from the rail WEL. As a result, the microstructures in specimens heated to 780 ˚C and higher temperatures will not be shown and discussed.

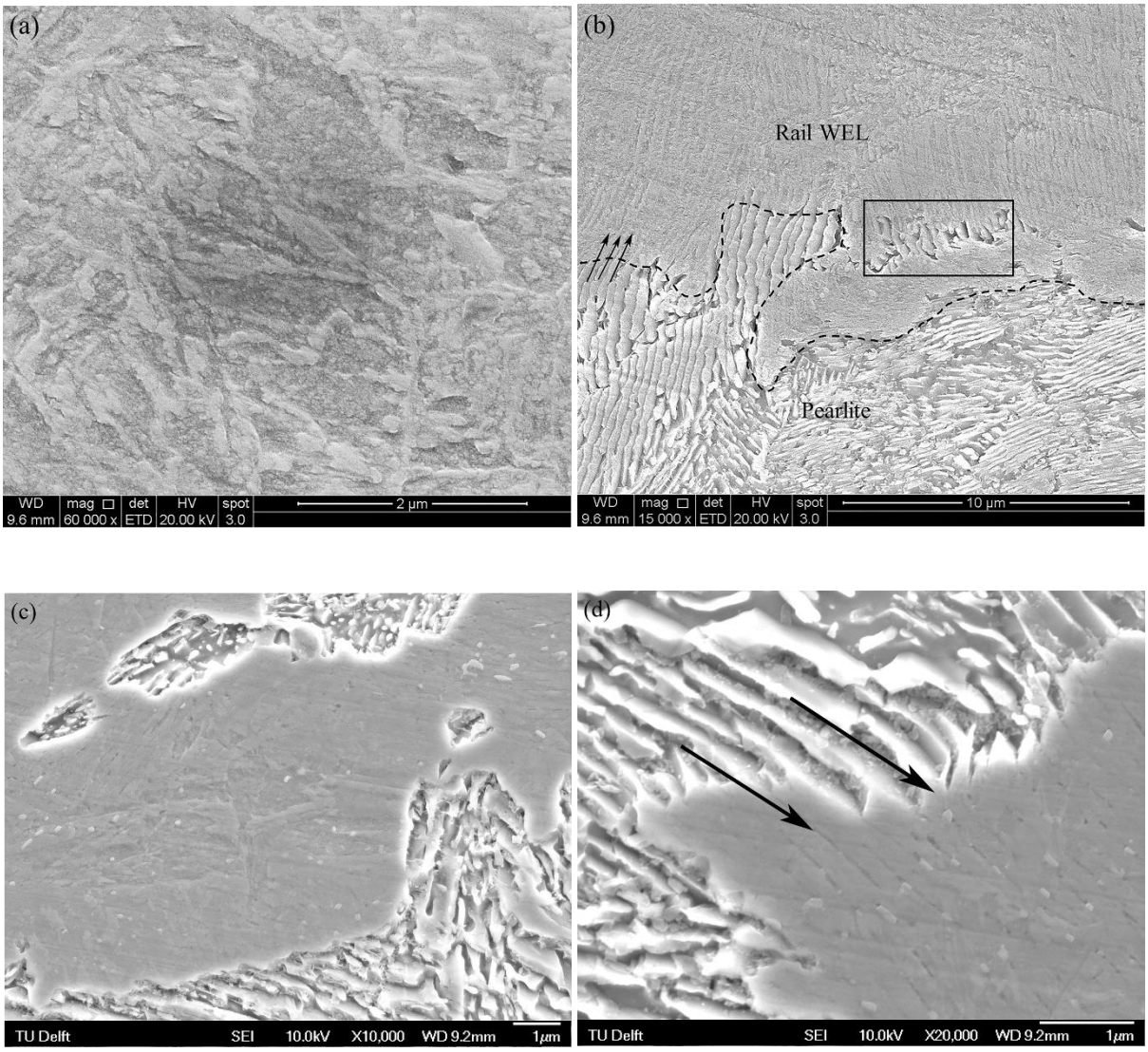

Fig. 5.4 SEM micrographs showing: (a) lamellar morphology in the rail WEL, (b) the aligned line feature at the rail WEL/pearlite boundaries, (c) lamellar morphology and (d) line feature in laboratory specimen $S_{730\text{-}020}$. The dashed line in (b) decorates the rail WEL/pearlite boundary and the arrows in (b) and (d) indicate the continuation from cementite lamellar in pearlite to line feature in rail WEL and laboratory WEL. Note the difference of scales.

The microstructure in the $S_{730\text{-}200\text{-}s}$ is similar to specimen $S_{730\text{-}200}$, namely with mixed featureless martensite and brown pearlite in the optical microscopy and lamellar traces within the as-formed martensite. The difference between the $S_{730\text{-}200}$ and the $S_{730\text{-}200\text{-}s}$ is that the fraction of martensite differs. In the $S_{730\text{-}200}$, the fraction of the white featureless blocks is 12% while in $S_{730\text{-}200\text{-}s}$ the fraction increases up to 56%. The hardness of martensite in $S_{730\text{-}200\text{-}s}$ is 910-930 HV and is higher than that of the martensite in the $S_{730\text{-}200}$, with a hardness of 670-810 HV.

Figs. 5.5(a) and (b) show SEM micrographs of the pearlite before the thermo-mechanical test and the microstructure in the $S_{730\text{-}200\text{-}s}$. Spheroidized cementite is observed in both figures. A further quantification of the fractions of the cementite spheroids from 10 randomly selected areas identifies 19

± 6% spheroidized cementite in the untested specimen while the fraction increases to 40 ± 30% in $S_{730\text{-}200\text{-}s}$, corresponding to a 20% increase in the average fraction of cementite spheroids. The increased fraction of cementite spheroids can be due to cementite fragmentation during plastic deformation during the test.

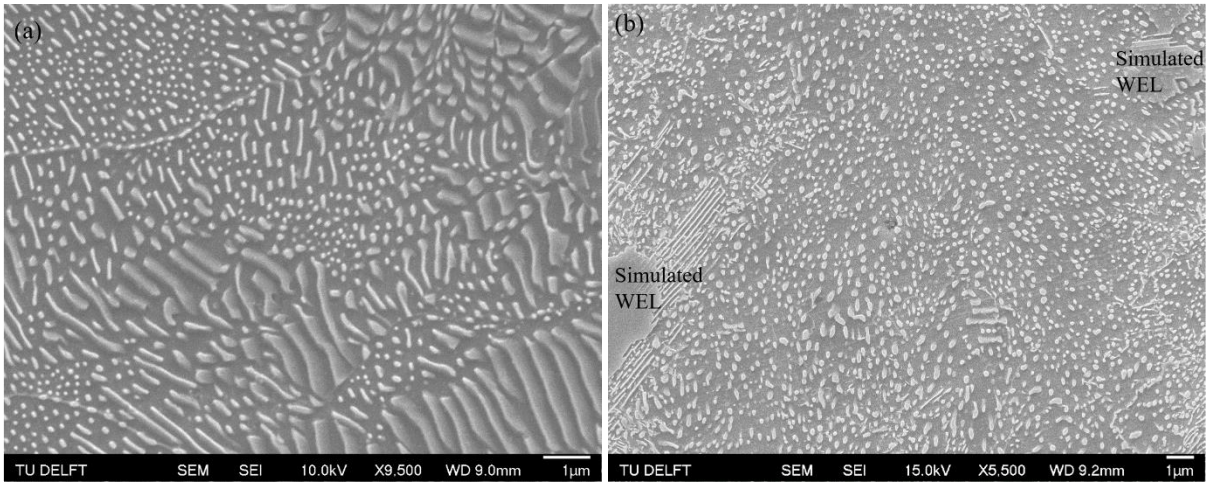

Fig. 5.5 SEM micrographs: (a) pearlite in the specimen before thermo-mechanical tests; (b) the microstructure in the $S_{730\text{-}200\text{-}s}$.

Fig. 5.6(a) and (b) show the SEM images of the rail WEL and simulated WEL in specimen $S_{730\text{-}200}$ respectively. The dashed lines in Fig. 5.6(a) schematically indicate the WEL/pearlite boundaries. Fig. 5.6(b) and (c) are grey scale image quality (IQ) maps, imposed by the map of austenite phase, in red, of Figs. 5.6(a) and (b) respectively. Both WELs show a lower IQ than the pearlite matrix in the IQ maps, probably due to the dislocation density in the WELs. The white lines in Fig. 5.6(c) delineate the axis/angle rotation of $90° < 1\,1\,2 >$, representing the Kurdjumov-Sachs (K-S) orientations between martensite and austenite. The match of K-S orientation between austenite and ferrite, in Fig. 5.6(c), strongly supports the martensitic nature of the rail WEL. Austenite is also identified in the laboratory WEL in Fig. 5.6(d).

The size distribution of the grains in the rail WEL and the laboratory simulated WEL in specimen $S_{730\text{-}200}$ is shown in Fig. 5.6(e). To build this plot, only the WELs are cropped and the pearlitic zones are discarded for the quantitative comparison. It can be seen that the grain size range in the rail WEL and the laboratory WEL in $S_{730\text{-}200}$ is comparable. There are higher fractions of grains smaller than 300 nm in the rail WEL than in $S_{730\text{-}200}$, Fig. 5.6(e). This is probably due to the grain refinement in the rail WEL by the deformation exerted by the passing trains. It should be noticed that the maximum grain diameter in rail WEL, 3.6 µm, is also larger than that in the simulated WEL in $S_{700\text{-}200}$, 1.7 µm. The average grain size measured in the rail WEL, Fig.5. 6(c), is 272 nm whereas the average grain size of the laboratory WEL in Fig. 5.6(d) is 269 nm.

Kernel average orientation (KAM) maps are often used to evaluate the strain distribution and they link the local lattice distortion measured via EBSD to the dislocation density in the material [14]. The KAM

plot of the rail WEL and the laboratory WEL is shown in Fig. 5.6(f). The analysis shows that the martensitic structure formed in the rail WEL has higher KAM than the one formed via lab simulation. This observation is logically consistent with the fact that the martensite in the WEL in rails is formed in the conditions of severe local deformation. Such conditions do not exist during the lab simulations of WEL.

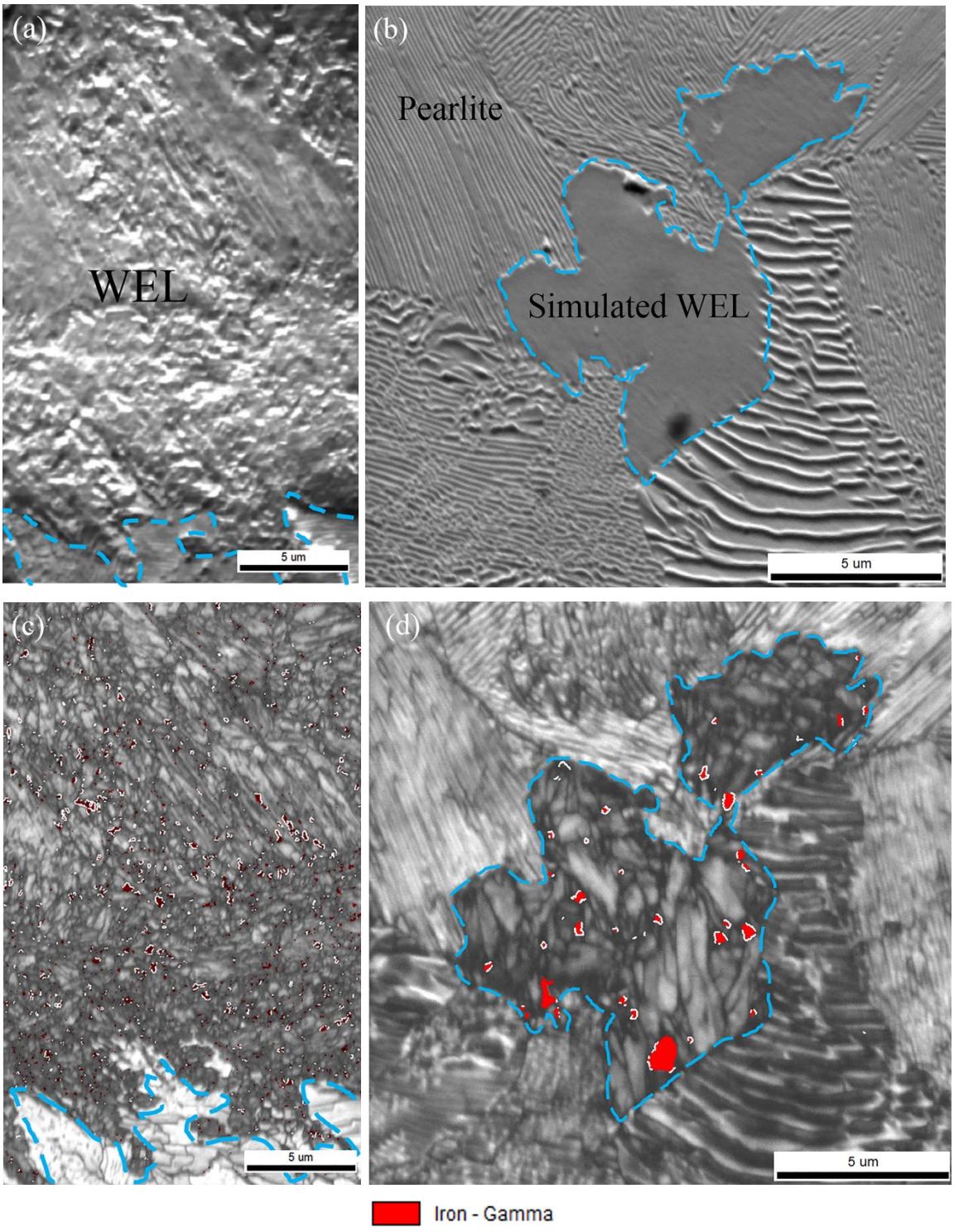

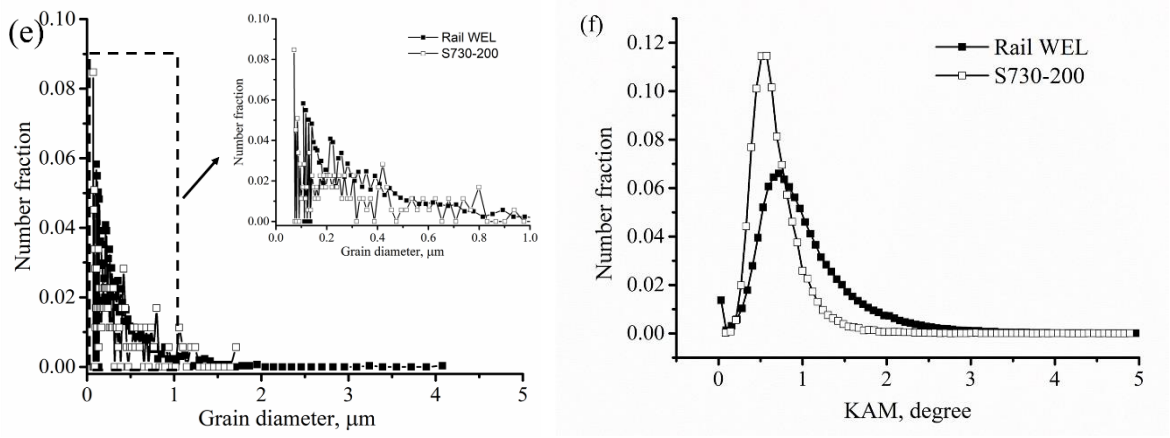

Fig. 5.6(a) SEM micrograph of rail WEL. The blue lines indicate the WEL/pearlite boundary; (b) The SEM micrograph of the simulate WEL in sample $S_{730\text{-}200}$; (c) The IQ map of rail WEL in (a), imposed with austenite phase map. The phase boundaries satisfying the K-S orientation relationship are delineated by the white lines; (d) The IQ map of laboratory WEL of specimen $S_{730\text{-}200}$ in (b), imposed with austenite phase map; (e) Grain diameter distribution of both rail WEL and laboratory WEL in $S_{730\text{-}200}$; (f) KAM distribution of both rail WEL and laboratory WEL in $S_{730\text{-}200}$

5.4. Discussion

5.4.1. Comparison to the literature on rail WELs

A comparison of the characteristics of the studied rail WEL with WELs in literature will be first made. Due to the widely reported nanometer scale microstructure of WEL in rails, high-resolution techniques are usually required, such as using TEM or synchrotron XRD as summarized in Table 1. For example, lattice tetragonality detected by synchrotron XRD is convincing evidence for the martensite nature of the WEL, e.g. [8,9]. In some cases, micromechanical property measurements, e.g. by hardness tests, can be useful in differentiating WELs formed by different mechanisms. For example, the nanocrystalline ferrite rail WEL is commonly reported to be accompanied by the following features in the adjacent pearlite [10,11]: *(i)* a transient work-hardened pearlite zone beneath the WEL, *(ii)* an obvious reduction of the interlamellar cementite distance in the work-hardened pearlite zone. Consequently, observations of the absence of work-hardened zone and the cementite lamellae thinning in the pearlite matrix, e.g. [7], can be a strong indication of WEL not being formed by severe plastic deformation. Consequently, the studied rail WEL is most probably martensite due to the observation of: *(i)* the almost intact pearlite colonies immediately beneath WEL in the rail sample, Fig. 5.3(a), and the absence of work-hardened pearlite area beneath WEL; *(ii)* the almost unchanged interlamellar distance within the WEL, compared with the one in the connecting matrix, c.f. Fig. 5.4(b); *(iii)* the identification of retained austenite in the rail WEL in Fig. 5.6(c).

The laboratory simulated WEL consists of martensite with a similar morphology as observed in the studied rail WEL, see Figs. 5.4(a) - (d). The hardness of the simulated WEL, corresponding to Figs.

5.4(c) and (d), is 670-810 HV. This is in general a bit lower than the measurements in the rail WEL, 725-1050 HV. However, the current laboratory tests represent only one phase transformation cycle. Five repeated heat treatment cycles have been done to specimen $S_{730\text{-}200}$ and the hardness increases to 700 - 850 HV. Repeated fast heat treatments form a well-known procedure for producing finer martensite, thus higher hardness, c.f. [15]. Accordingly, martensite with equivalent hardness as the rail WEL might be produced after multiple wheel passages. In addition, the well-controlled heat treatment also allows relating the quantitative microstructure analysis to the exact heat treatment. The microstructural quantification from the experimental simulation can be used to clarify rail WEL formation due to increased temperature, in the condition where the heating rate is much higher than the current laboratory work.

The temperature change during wheel/rail contact plays an important role in arguing the WEL formation mechanisms. For example, Newcomb [10] characterized the WEL to be fully martensitic. However, the martensite transformation theory is not supported by the temperature rise calculations. As an alternative, he proposes that the martensite in the WEL is a ferrite with supersaturated carbon, which is accommodated by dislocations generated due to plastic deformation.

In the following sections, the temperature rise in the studied rail will be estimated using finite element modeling (FEM). A subsequent discussion on the observed microstructures in the laboratory simulated WEL and the rail WEL will also be made.

5.4.2. Estimation of temperature rise using FE method

When wheels are running on rails, frictional heat is generated at the wheel/rail contact interfaces, causing a temperature rise in the materials. The thermo-mechanical behavior of the wheel-rail contact has been widely studied in the literature, see e.g. [16,17]. The problem of the temperature rise in the wheel-rail system has recently been investigated, using a coupled thermal-mechanical analysis [18]. With the finite element (FE) tool developed in [18], the frictional heat generated during rolling contact and the resulting temperature rise in the materials can be calculated.

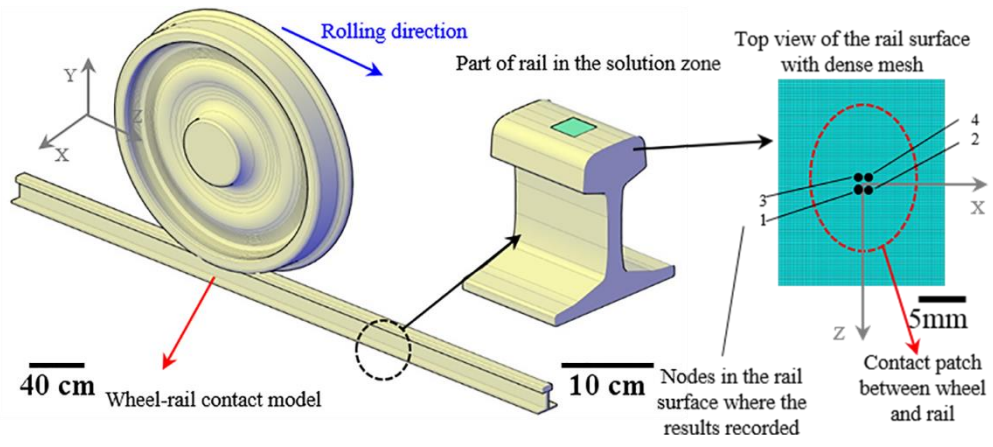

Fig. 5.7 The wheel-rail contact model for calculating temperature rise due to frictional heat

The model developed by Naemi in ref. [19] is used for the current calculation and is shown in Fig. 5.7. The model consists of a single train wheel with a diameter of 0.92 m and a rail track with a total length of 20.54 m. The wheel and rail materials are assumed to behave elastically and they are meshed with 8-node solid elements. To achieve high accuracy with reasonable computing time, a non-uniform mesh is applied with the finest element size of 0.3×0.3 mm^2 in the solution zone and areas far away from the solution zone is meshed with size up to 7.5 cm. At the beginning of the simulations, the materials are uniformly at the ambient temperature and the thermo-mechanical stresses are zero. The magnitudes of the stresses and the temperature at a material point at the contact interface ascend when the wheel approaches it. Four points were selected at the nodes shown in Fig. 5.7 for the temperature output. Using the parameters listed in Table 2, a wheel with a typical velocity of 140 km/h of the Dutch trains rolling along a straight rail was considered with a longitudinal creepage of 3.6%. This corresponds to a slip velocity of 5 km/h. A high friction coefficient of 0.6 was used and the ambient temperature was set to 25 °C. This choice is made, since a higher friction induces greater heat generation at the contact interface, leading to a more critical state. A higher magnitude of creepage can also lead to a higher temperature rise. It is in practice, however, unlikely to have very high creepage in the presence of a high friction coefficient. With a creepage of 3.6% and a friction coefficient of 0.6, the contact was around the point of full slip, i.e. loss of adhesion area in the contact patch, while the wheel was rolling. This is thus indeed a critical situation. According to [9], this status of the friction and creepage was roughly estimated to generate a flash temperature of around 700 °C.

The temperature evolution with time in the rail surface was calculated and shown for the four nodes, Fig. 5.8(a), and their average, Fig. 5.8(b). The nodes were in the middle of the running band, where maximum temperature rise is expected. The temperature increases abruptly when the wheel arrives at the nodes. The peak temperature is obtained, when the nodes are in the rear part of the contact. When the wheel leaves the nodes, they rapidly cool down.

Table 5.2 Parameters used in the thermo-mechanical FE model for typical critical Dutch-operation conditions

Symbol (units)	Description	Values
V (km/h)	Wheel forward velocity	140
S (%)	Creepage	3.6
V_s (km/h)	Slip velocity	5.0
F	Coefficient of friction	0.6
E (GPa)	Young's modulus	210
υ	Poisson's ratio	0.3
κ (m^2/s)	Thermal diffusivity	1.518×10^{-5}
λ (W/°Cm)	Thermal conductivity	50
ρ (kg/m^3)	Density	7850
c (J/kg/°C)	Specific heat capacity	419.5
N (kN)	Normal load	134
M_w (kg)	Wheel weight	900
R_w (m)	Wheel radius	0.46
T_0 (°C)	Ambient temperature	25

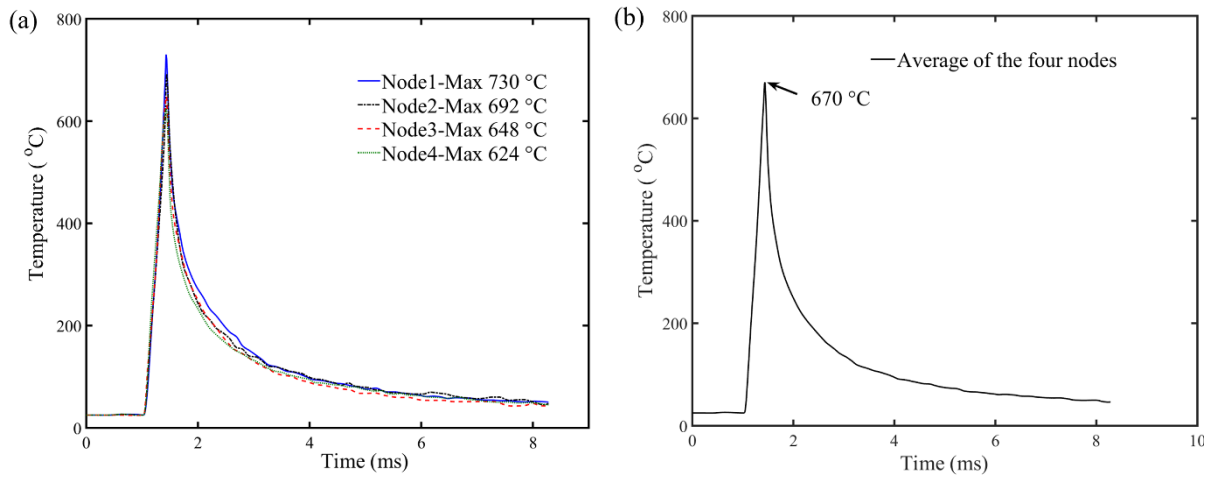

Fig. 5.8 (a) The temperature evolution with time in the rail surface of the four nodes in Fig.5. 7; (b) The average temperature variation with time of the four nodes.

The highest temperature occurring at node 1 is 730 °C. This temperature is higher than both the Ae_1 for steel under atmosphere pressure, which is 700 °C (cf. Fig. 5.2(a)) and the Ae_1 of steel under hydrostatic pressure of 1.8 GPa, which is 670 °C (cf. Fig. 5.2(b)). The average maximum temperature of the four nodes is 670 °C. It is 30°C lower than the Ae_1 for steel under atmospheric pressure (700 °C), but it is the same as Ae_1 of steel under hydrostatic pressure of 1.8 GPa (670 °C). Hence, it is possible that the heat generation in the wheel/rail contact increases the rail surface temperature above the critical one for austenite formation.

Using the data plotted in Fig. 5.8(b), one can estimate the average heating and cooling rate in the rail during wheel passage. The average heating rate is estimated to be 1.5×10^6 °C/s. The cooling rate between 700 °C and 400 °C, which is the temperature zone for pearlite and bainite formation, is estimated to be 1.7×10^6 °C/s. This cooling rate should be sufficient to prohibit the formation of pearlite or bainite. The cooling rate between 300 °C and 46 °C, within which martensite transformation is expected for the studied rail composition, is around 3.9×10^4 °C/s. Martensite can then form when the surface is cooled to the ambient temperature.

It needs to be emphasized that a high frictional coefficient, 0.6, is needed in the FE modeling, in order to reach the required austenitization temperatures for the pearlite to austenite transformation to occur during the wheel/rail contact. Such high frictional coefficient corresponds to quite extreme operation conditions such as during train brake/acceleration. In addition, other sources, which are not considered in the FE modeling in this chapter, can lead to a similar temperature increase as well. For example, the presence of contaminations on the rail track, such as water, fallen leaves and etc. is a typical problem in Dutch railway network [20]. Accordingly, very slippery films can form on the rail surface and can subsequently lead to the wheel spinning on the rail track. Such wheel spinning can further *1)* introduce a significant temperature increase at rail surface, which can even be high enough to cause local melt on

the rail surface [20]; *2)* lead to the occurrence of the local flattening on wheel perimeters, the so-called wheel flat [21]. A substantial increase in the friction coefficient due to the presence of wheel flat can arise and can lead to the extensive temperature increases both on rail and wheel surfaces. Finally, the microstructure characterizations in Chapter 4 form a strong indication of such significant temperature increases at the rail surface.

5.4.3. Thermodynamic interpretation

The observed microstructures in the laboratory specimens can be interpreted from thermodynamic and kinetic theories. As discussed in the previous section, a mixture of martensite and pearlite is identified in laboratory specimens $S_{730\text{-}020}$ till $S_{830\text{-}020}$, using hardness measurements and SEM. This means that the initial pearlite has partially transformed to austenite and martensite forms because of the subsequent quenching during the laboratory experiments. When a specimen was heated to a temperature of 880 °C and higher, cementite was not observed and a possible single martensite is detected by hardness measurements, Fig. 5.3(d). Comparing with the calculated Fe-C phase diagram in Fig. 5.2(a), the specimens with mixed martensite and pearlite microstructure must have been heated to the temperatures within the three-phase region in Fig. 5.2(a). For temperatures above the three-phase region, no cementite is expected.

The theory of phase transformation kinetics should be applied in the interpretation. The changes of the upper limit temperature can be the result of a local non-equilibrium condition due to the fast heating [22]. The equilibrium carbon concentration in austenite formed in the three-phase region is calculated with Thermo-Calc to be nearly constant at 0.69 wt%. As a result, carbon partitioning is needed for austenite to form, through a diffusional process. Carbon diffusion from cementite to the austenite/ferrite phase front is required for austenite to grow. The increasing heating rate shortens the diffusion time, thus the diffusion distance, of carbon in austenite for the same austenitizing temperature. As a result, the complete transformation of cementite to austenite will be delayed, leading to the observation of lamellae or the line traces in martensite, c.f. Fig. 5.4(d). This also matches well with the observed smaller fraction of martensite formed in heat treatment with the higher heating rate.

Similar arguments can also be used to interpret the observed microstructure of the studied rail WEL. As discussed in the previous sections, the studied rail WEL is probably martensite on the basis of comparison with the literature and comparison with the laboratory simulate WEL. The temperature calculations also support the WEL formation through martensite phase transformation in the studied rails. As a result, the rail WEL forms most probably due to phase transformation and the interpretation for the observed microstructure in the laboratory specimens can also be used for the observations in rail WEL.

For the diffusional transformation of pearlite to austenite, the diffusion of alloying elements in austenite determines the growth kinetics of austenite. Therefore, an estimation of the diffusion distance of alloying elements will be made. According to the current FEM simulation, the rail surface is unlikely to be heated

up to 900 °C or higher, below which the diffusivity of manganese and silicon in the austenite is low [23]. Therefore, only carbon diffusion will be evaluated and only the diffusion distance of carbon in the austenite will be estimated. The diffusivity, *D*, of carbon in austenite is expressed as:

$$D = D_0 \times \exp^{(-\frac{Q}{RT})}, \qquad (1)$$

where D_0 = 0.234×10^{-4} m^2/s, is the pre-coefficient, Q = 147.81 kJ/mol is the activation energy, R is the gas constant, T is the temperature at which the interstitial element diffuses [24].

The average diffusion distance, L, is then approximated by

$$L = \sqrt{Dt} \quad , \qquad (2)$$

where t is the diffusion time within the austenitizing temperature zone which is calculated by:

$$t = \frac{(T - T_{Ae1})}{v} \qquad (3)$$

where T_{Ae1} is the A_{e1} temperature and v is the heating rate.

It has been shown that the hydrostatic pressure of 1.8 GPa leads to a reduction of 30 °C in A_{e1} , from the one calculated at atmospheric pressure. The equilibrium A_{e1} of atmospheric pressure will be used for calculating the diffusing time, *t*. Since carbon can diffuse into ferrite from the two neighboring cementite plates for a lamellar pearlite microstructure the maximum diffusion distance for the carbon from cementite to ferrite then equals half the cementite interlamellar distance, namely 75 nm. Using equation (1) – (3), a maximum temperature of 1034 °C is required for carbon to diffuse for such distance in one single heating cycle using the heating rate of 1.7×10^6 °C/s, estimated from previous FEM simulation. This temperature is much higher than the calculated temperature in Figs. 5.8(a) and (b). At lower temperature, the diffusivity *D* and diffusion *t* reduce, leading to shorter diffusion distance. It is thus can be speculated that multiple cycles will be needed for the pearlite to be fully austenitized.

The hydrostatic pressure of 1.8 GPa also leads to a shift of the eutectoid point, from 0.7 wt% C under atmospheric pressure to 0.48 wt% C, cf. Figs. 5.2(a) and (b). This means that during the wheel/rail contact, the rail composition will become hypereutectoid if the generated hydrostatic pressure is high enough. This will cause the cementite to be stable at higher temperatures than for a hypo-eutectoid composition. After load release, the rail composition returns to be hypo-eutectoid and the microstructure is expected to consist of martensite and cementite. As a consequence, detection of cementite in the martensite WEL, c.f. [8], can be either due to the shift of eutectoid point due to the external load or due to the pearlite being heated to the three-phase region in the phase diagram in Fig. 5.2(a).

It is shown in this study that WEL formation through martensite phase transformation is supported by laboratory simulations, numerical temperature simulations and thermodynamic calculations. The additional contribution from the simultaneous deformation during heating is to promote the formation of austenite, which subsequently transforms to martensite. In addition, the martensite formed from combined deformation and heating is also harder than that formed only by heating. The causes for the promoted austenite formation due to combined deformation and heating can be: *(i)* cementite lamellae

breakage, which increases the surface area of cementite and provides extra sites for austenite nucleation; *(ii)* generation of dislocations, which enhances the carbon diffusion and consequently facilitates the austenite growth.

5.5. Conclusions

Martensitic WEL is simulated in the laboratory by fast-heating treatments, using heating rates of 20 ºC/s and 200 ºC/s. Characteristics of the transformed martensite are analyzed by microhardness, optical microscopy, scanning electron microscopy and electron backscatter diffraction. Microstructures of WEL from the studied rail surface are also investigated and compared with the microstructures of simulated martensite. The main results can be summarized as follows:

1. Rail WEL is martensite.
2. White etching areas form in the laboratory simulations.
3. Mixed microstructures of martensite and pearlite are both identified in samples heated to temperatures of 730 °C to 830 °C. This can be interpreted by the deviation from the equilibrium condition in the three-phase region of ferrite, cementite and austenite in the calculated iron-carbon phase diagram due to fast heating rates.
4. The hydrostatic pressure of 1.8 GPa leads to a 30 °C reduction in the austenite start temperature and a significant shift of the eutectoid carbon concentration. Due to the high external pressure the eutectoid carbon concentration shifts from 0.7 wt% C to 0.48 wt% C and the corresponding A_1 temperature changes from 700 °C to 670 °C.
5. Simultaneous deformation and heating significantly promote martensite formation in rail steels.
6. On the basis of comparison with the observed WEL in rails and the simulated WEL and WEL from literature, it is shown that the investigated WEL in rail is most likely martensite. The observations find good support by the thermodynamic and kinetic simulations and numerical frictional heat simulations.

References

[1] Dikshit V, Clayton P, Christensen D. Investigation of rolling contact fatigue in a head-hardened rail. Mechanics and Fatigue in Wheel/rail contact, 1990; 89-102.

[2] Steenbergen M, Dollevoet R. On the mechanism of squat formation on train rails – Part I: Origination. Int J Fatigue 2013;47:361–72.

[3] Clayton P, Allery MBP. Metallurgical Aspects of Surface Damage Problems in Rails. Can Metall Q 1982;21:31–46.

[4] Lojkowski W, Djahanbakhsh M, Bürkle G, Gierlotka S, Zielinski W, Fecht HJ. Nanostructure formation on the surface of railway tracks. Mater Sci Eng A 2001;303:197–208.

[5] Österle Rooch, H., Pyzalla, A., Wang, L. Investigation of white etching layers on rails by optical microscopy, electron microscopy, X-ray and synchrotron X-ray diffraction. Mater Sci Eng A 2001;303:150–7.

[6] Zhang HW, Ohsaki S, Mitao S, Ohnuma M, Hono K. Microstructural investigation of white etching layer on pearlite steel rail. Mater Sci Eng A 2006;421:191–9.

[7] Takahashi J, Kawakami K, Ueda M. Atom probe tomography analysis of the white etching layer in a rail track surface. Acta Mater 2010;58:3602–12.

[8] L. WÖRHPAW. Investigation of white etching layers on rails by optical microscopy, electron microscopy, X-ray and synchrotron X-ray diffraction. Mater Sci Eng A 2001;303:150–7.

[9] E. A. LWPASWW. Microstructure features on rolling surfaces of railway rails subjected to heavy loading. Mater Sci Eng A 2003;359:31–43.

[10] Newcomb SB, Stobbs WM. A transmission electron microscopy study of the white-etching layer on a rail head. Mater Sci Eng 1984;66:195–204.

[11] Baumann G, Fecht HJ, Liebelt S. Formation of white-etching layers on rail treads. Wear 1996;191:133–40.

[12] Wu J, Petrov RH, Naeimi M, Li Z, Sietsma J. A Microstructural Study of Rolling Contact Fatigue in Rails. Proc. Second Int. Conf. Railw. Technol. Res. Dev. Maintenance, Ajaccio, Fr. 8-11 April 2014, Civil-Comp Press; 2014.

[13] Rovira A, Roda A, Marshall MB, Brunskill H, Lewis R. Experimental and numerical modelling of wheel–rail contact and wear. Wear 2011;271:911–24.

[14] Porter DA, Easterling KE, Sherif M. Phase Transformations in Metals and Alloys, (Revised Reprint). CRC press; 2009.

[15] Tsuji N, Maki T. Enhanced structural refinement by combining phase transformation and plastic deformation in steels. Scr Mater 2009;60:1044–9.

[16] Fischer FD, Werner E, Yan W-Y. Thermal stresses for frictional contact in wheel-rail systems. Wear 1997;211:156–63. doi:http://dx.doi.org/10.1016/S0043-1648(97)00108-7.

[17] Ertz M, Knothe K. Thermal stresses and shakedown in wheel/rail contact. Arch Appl Mech 2003;72:715–29.

[18] Naeimi M. Computation of the flash-temperature at the wheel-rail contact using a 3D finite element model and its comparison with analytical methods. 10th Int. Conf. Contact Mech. (CM 2015), 2015.

[19] Wu J, Petrov RH, Naeimi M, Li Z, Dollevoet R, Sietsma J. Laboratory simulation of martensite formation

of white etching layer in rail steel. Int J Fatigue 2016;91:11–20.

[20] Arias-Cuvvas O., Ph.D. thesis, Low Adhesion in the Wheel-rail COntact. Delft University of Technology, 2010.

[21] Ahlström J, Karlsson B. Microstructural evaluation and interpretation of the mechanically and thermally affected zone under railway wheel flats. Wear 1999;232:1–14.

[22] Meshkov YY, Pereloma E V. 17 - The effect of heating rate on reverse transformations in steels and Fe-Ni-based alloys. In: Pereloma E, Edmonds D V, editors. Phase Transform. Steels, vol. 1, Woodhead Publishing; 2012, p. 581–618.

[23] Savran V., Ph.D. thesis, Austenite formation in C-Mn steel. Delft University of Technology; 2009.

[24] Wever H. H. Mehrer (Ed.): Landolt-Bornstein, Numerical Data and Functional Relationships in Science and Technology, New Series, Group III: Crystal and Solid State Physics, Vol. 26, Diffusion in Metals and Alloys, Springer-Verlag, Berlin, 1990, ISBN 3-540-50886-4, . Berichte Der Bunsengesellschaft Für Phys Chemie 1993;97:952.

Chapter 6 Phase-field modeling of white etching layer formation in rail steels via thermally induced phase transformation

Abstract:
In this chapter, the pearlite – austenite transformation during (ultra-)fast heating is simulated by the phase-field approach to provide insight into the white etching layer formation (WEL) in rail steels. The ferrite and cementite lamellae in the pearlite microstructure are individually resolved and martensite is included to represent the process occurring during the repeated wheel passages. The insight into the WEL formation was obtained by studying the pearlite to austenite transformation with heating rates of 10 °C/s and 2000 °C /s. It is concluded that pearlite to austenite transformation occurring during WEL formation is most probably an interface-controlled process, related to the extremely high heating rate. The carbon concentration and the corresponding mechanical properties of martensite in a single WEL block can be significantly heterogeneous, depending on the heating rate during the wheel passages.

6.1. Introduction

As discussed in chapters 4 and 5, the white etching layer (WEL) in the studied Dutch R260Mn grade rail steel forms predominantly via the pearlite to austenite transformation and the subsequent martensitic transformation. This conclusion is consistent with microstructure characterizations of WELs in rail steels in the literature, e.g. [1,2]. Moreover, a similar white color martensite layer forms in the rail's counterpart wheel steels [3,4], which have a similar pearlitic type microstructure as rail steels. The high temperature required for such transformation to take place is due to frictional heat during the wheel/rail contact, e.g. more than 700 °C, and has been shown to be conceivable from numerical simulations [5]. As a result, thermal induced phase transformation is concluded to be the dominant mechanism for the WEL formation.

The formation of martensite mainly introduces the following detrimental effects to the rail lifetime: *(i)* The martensite in the WEL is much harder, typically 2 – 3 times, than the matrix pearlite microstructure. The martensite in the WEL can thus lead to premature brittle fracture during the in-track service or can cause extensive plastic deformation of surrounding pearlite at the WEL edges [6]. The pearlite corresponding to the latter locations can accumulate more plastic strain and consequently lead to the premature crack formation, comparing with pearlite areas without the presence of WEL. The above facts can contribute, partially or fully, to rolling contact fatigue (RCF) damage initiation at the WEL, e.g. [7–9]. *(ii)* The austenite to martensite phase transformation introduces residual tensile stress on the rail (sub)surface, which will facilitate the propagation of the initiated cracks at the WEL and the adjacent pearlite [10,11]. As a result, the formed RCF cracks can grow quickly towards the rail center, necessitating increasing maintenance frequency or more extensive rail material removal [9]. The latter can lead to earlier rail replacement. Therefore, it will be of economic and safety importance to reduce/eliminate WEL formation in rail steels. This requires a profound understanding of mechanisms and the dominant characteristics of WEL formation.

WEL is typically observed in rail steels after a certain service period. This indicates that multiple train passages, i.e. phase transformation cycles, are necessary for the WEL to grow to the dimension which can be resolved by the laboratory facilities. The virgin pearlite microstructure first transforms to austenite, when the rail surface is heated above the starting temperature for austenite to form, i.e. the A_1 temperature. The austenitization procedure is generally accepted as a diffusional process and requires carbon redistribution between the parent ferrite, cementite and the product austenite phases. Such a procedure is time and temperature dependent [12,13]. The formed austenite tends to transform to martensite after the train wheel leaves the heated rail portion and WEL forms, due to the high cooling rate [14]. Whether austenite fully transforms to martensite depends on its chemical composition, since retained austenite can be present in the WEL [5,15].

However, the pearlite-austenite-martensite phase transformations for the WEL formation in rail steels can be extremely complex, due to the complicated cyclic thermal and stress conditions imposed by the

passing wheels. The wheel/rail contact conditions can affect the WEL formation mainly via the following aspects: *(i)* The extremely short contact time during one single wheel passage, especially for the diffusional pearlite to austenite transformation. A single wheel/rail contact is estimated to be typically on the order of 10^{-4} – 10^{-3} seconds [1,5]. Such short contact duration indicates the limited time for the alloying elements, mainly carbon [12], to diffuse and redistribute between the austenite and pearlite, for the austenite to grow. As a result, the pearlite to austenite transformation can be incomplete and the carbon concentration in the austenite can be heterogeneous, depending on the temperature and time reached in rail surface; *(ii)* The strongly varying temperatures reached, even at a single rail surface position, due to the dynamic wheel/rail contact. The variations in the temperatures can affect the completeness of pearlite to austenite formation [12]; *(iii)* The varying hydrostatic pressure from the running trains. The hydrostatic pressure can change the equilibrium, e.g. iron-carbon, state of the material. An estimation using the Thermo-Calc® software shows that hydrostatic pressure of 1.8 GPa only slightly lowers the critical austenitization temperature for the steel composition of the R260 Mn grade rail steel in [5], namely from 700 °C to 670 °C. A more significant consequence, due to such high hydrostatic pressure, in changing the eutectoid carbon concentration is instead predicted, i.e. from 0.7 wt% to 0.48 wt%; *(iv)* Deformation-induced crystal defects. Besides the temperature increase, plastic deformation can also occur in the rail steel. The dislocations generated due to the plastic deformation can: *(1)* increase the free energy state of the ferrite and thus facilitate ferrite to austenite transformation; *(2)* enhance the carbon diffusion from cementite to ferrite. An increase in the grain boundary area, due to grain refinement by the possible recrystallization, offers extra sites for austenite to nucleate.

The formed austenite tends to transform to martensite, i.e. the WEL, during the quenching, and the carbon concentration in the austenite will be inherited by the product martensite via the diffusionless transformation mechanism [14]. The local mechanical properties of the WEL are related to the carbon concentration in the previous austenite. As a result, the details of the austenitization are directly influencing the WEL formation and the final characteristics of the WEL.

The pearlite to austenite transformation can be modeled by phase field modeling (PFM). There are numerous studies on PFM about the diffusional solid-solid phase transformation process in steels, see for example the review by Militzer et al. [16]. The most common examples are the simulations of austenite to ferrite transformation during continuous cooling [17–19]. There are, in the meantime, examples of the reverse ferrite/pearlite to austenite transformations [12,20]. For example, Savran [12] studied the austenitization process from a pearlitic type microstructure in a commercial steel by PFM, during continuous heating and isothermal treatments. Azizi-Alizamini [21] simulated austenite formation from pearlitic microstructures with an ultra-fine grain (UFG) structure of a Fe-C system. They both reach a good match between the simulated microstructure and the experimental observations. In addition, they have been able to identify detailed characteristics of the transformations, e.g. the different transformation kinetics of ferrite and cementite to austenite.

Additionally, (semi-) quantitative insight into WEL formation via martensite phase transformation is possible by using the PFM. The austenite to martensite transformation, i.e. the formation of WEL, is diffusionless and the martensite can be considered to inherit the compositional features of the parent austenite [14]. As a result, insight into the characteristics during austenite formation is considered to be crucial for martensite formation, indicating the suitable application of the PFM for the purpose. In this chapter, the WEL formation via austenite and martensite phase transformation was studied by PFM. Due to the above discussed complex conditions for the WEL formation in rails, it can be expected that it will be difficult to reproduce the WEL formation procedure in all detail. Instead, the current simulations aim to provide semi-quantitative insight into the WEL formation, during ultra-fast heating conditions. Based on the simulation results, possible routes to reduce the WEL occurrence in rail steels are discussed.

6.2. Modeling concept

6.2.1. The microstructure model

Building a representative pearlitic microstructure model of rail steel is complex. On the one hand, a sufficient number of pearlite grains/colonies must be included in order to have a realistic representation. The pearlite grains in rails are typically tens of micrometers in diameter and a representative microstructure model thus should cover a dimension range of 10^{-5} – 10^{-4} m. On the other hand, the pearlite consists of fine lamellae of ferrite and cementite, which are typically10^{-8} -10^{-7} m in thickness. The lamellae thickness depends on the steel chemistry and the thermo-mechanical production processes. Accordingly, a very fine mesh size is required so that the lamellae can be adequately resolved for the PFM calculations. Expectably, a significant calculation time, in addition to the requirement of large memory size [12], will be crucial for a large-scale modeling with a resolution that is sufficient to account for the lamellae.

Pearlite has been modeled by different strategies and is adopted depending on the applications. Simplifying the pearlite microstructure as a single phase, to which a eutectoid carbon concentration is assigned, can be useful for large-scale simulations, see Savran [12]. This simplification enables a representatively large pearlite microstructure while without requiring very fine mesh size and the correspondingly extensive computing time. General agreements of austenite formation kinetics and the microstructure morphology are achieved. However, closer observations of austenite formation, especially under non-equilibrium conditions like fast heating conditions, frequently identify a cementite to austenite transformation lagging the ferrite to austenite transformation [12,21,22]. This aspect cannot be modeled by the above simplification for pearlite and the ferrite and cementite must be resolved separately [16].

Alternatively, Savran et al [12] and Militzer et al. [23] performed separate high-resolution PFM, in which ferrite and cementite lamellae are treated individually. In their simulations, a significantly refined

microstructure domain, typically $10^4 – 10^5$ nm^2, is used, for a sufficient insight into the transformation characteristics of individual phases without extensive computing time. In addition, a very small grid size is used to sufficiently resolve the fine lamellae in the pearlite, e.g. 23 nm comparing with 330 nm for the large-scale simulations, both in [12]. Moreover, the pearlite to austenite transformation kinetics can be semi-quantitatively represented, despite the small simulation scale. In the present study, the pearlite microstructure in the R260 Mn grade rail steel is built by following the high-resolution PFM modeling of Savran in [12]. However, a much higher heating rate is used in the current simulation, relating to the actual situation during train passage.

The 2D microstructure model in Fig. 6.1 is used for the simulations in the current study. The primary focus of this study is the characteristics of chemical composition evolution in the austenite phase during the pearlite to austenite transformation. In addition, the carbon diffusion path in a microstructure with a planar lamellar morphology can be assumed to be isotropic, justifying the simplifications in this study. As a result, the 2D microstructure in Fig. 6.1 is considered to be suited to represent the realistic 3D microstructure in the studied rail steel.

The alternating gray ferrite lamellae and the white cementite lamellae, in two adjacent pearlite colonies, represent the observed lamellar pearlite microstructure in the studied R260Mn grade rail steel. The small-scale microstructure in Fig. 6.1 can be used to represent the local microstructures along the rail depth. The characteristics of phase transformation along rail depth, due to varying temperature caused by the passing wheels, can be studied by subjecting the microstructure model in Fig. 6.1 to different temperature cycles.

The phase and grain boundaries are represented by the dark lines in Fig. 6.1. In order to sufficiently resolve the fine cementite, a small grid of 20 nm is used and the cementite width is assigned to be ten grid points, i.e. 200 nm. The interface thickness is 4 times the grid size.

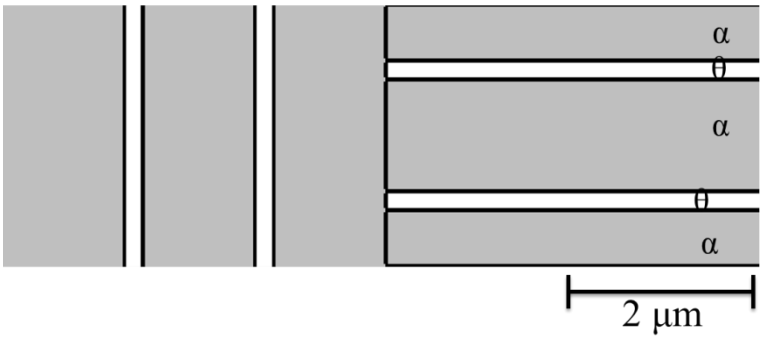

Fig. 6.1: The microstructure model used to represent the initial full pearlite in the R260 Mn grade rail steel. The gray component is α-ferrite and white is θ-cementite. The dark lines are the grain/phase boundaries.

6.2.2. Phase field model concept

The phase field simulations in the current study were done with the multi-phase-field software MICRESS®, which is based on the work of Steinbach et al. [24]. The phase transformation kinetics is described by a phase field parameter, $\emptyset_i$ (i=1…N) and for grain i, $\emptyset_i = 1$ inside the grain, and $\emptyset_i = 0$ elsewhere. At the grain junctions, e.g. before each grain i and j, the following applies: $\emptyset_i + \emptyset_j = 1$, and $0 < \emptyset_i < 1, 0 < \emptyset_j < 1$. For the whole system, the relation $\sum_{i=1}^{N} \emptyset_i\ (\boldsymbol{r}, \boldsymbol{t}) = 1$ applies everywhere, in which N is the total number of grains and i is the grain number, r and t are the location and time.

The transformation kinetics is described as the change of each phase field parameter with time, since gradients in $\emptyset_i$ are only formed at the interface, changes take place only at interface according to::

$$\frac{d\emptyset_i}{dt} = \sum_j \mu_{ij}\left[\sigma_{ij}\left(\emptyset_i\nabla^2\emptyset_j - \emptyset_j\nabla^2\emptyset_i + \frac{\pi^2}{2\eta_{ij}^2}\left(\emptyset_i - \emptyset_j\right)\right) + \frac{\pi}{\eta_{ij}}\sqrt{\emptyset_i\emptyset_j\Delta G_{ij}}\right] \quad (6.1)$$

in which i and j are the grain numbers; σ_{ij} is the interfacial energy; μ_{ij} is the interfacial mobility; η_{ij} is the interface thickness; ΔG_{ij} is the driving pressure.

The interfacial mobility, μ_{ij}, is considered to be temperature dependent and is described as:

$$\mu_{ij} = \mu_{ij}^0 \exp\left(\frac{-Q_{ij}}{kT}\right), \quad (6.2)$$

where Q_{ij} is the activation energy for interface motion, k is the Boltzmann constant, T is the temperature, μ_{ij}^0 is the pre-factor and can be calculated by:

$$\mu_{ij}^0 = \frac{d_{ij}^4 . v_D}{kT}, \quad (6.3)$$

where v_D is the Debye frequency, d_{ij} is the average interatomic distance :

$$d_{ij} = 0.5 * \left(V_i^{\frac{1}{3}} + V_j^{\frac{1}{3}}\right), \quad (6.4)$$

where V_i and V_j are the atomic volumes of the crystal structure of the neighboring grains i and j.

It is worth pointing out that the interfacial energy and the mobility are usually used as fitting parameters and are adjusted accordingly to match the experimental observations in different simulations [12,20,21]. However, the experimentally observed 'finger-type' microstructure during pearlite to austenite transformations are reported separately by simulations in the same papers [12,21], despite significantly different interfacial energies used. A full laboratory reproduction of the heating-quenching cycles is impractical, so the interfacial energies used in [12] are adopted in the current simulation for the purpose of a semi-quantitative insight into the process. Accordingly, Table 6.1 lists the calculated and adopted interfacial energies and activation energies for the current simulations.

Table 6.1 The adopted interfacial energy and activation energy for mobility from [12], used for the current simulations.

Phase interactions	γ:γ	γ:α	γ:θ	α:α	α:θ	θ:θ
σ_{ij} (J m^{-2})	0.076	0.039	0.0904	0.05	0.105	0.125
Q_{ij}(kJ mol^{-1})	185	150	150	150	215	215

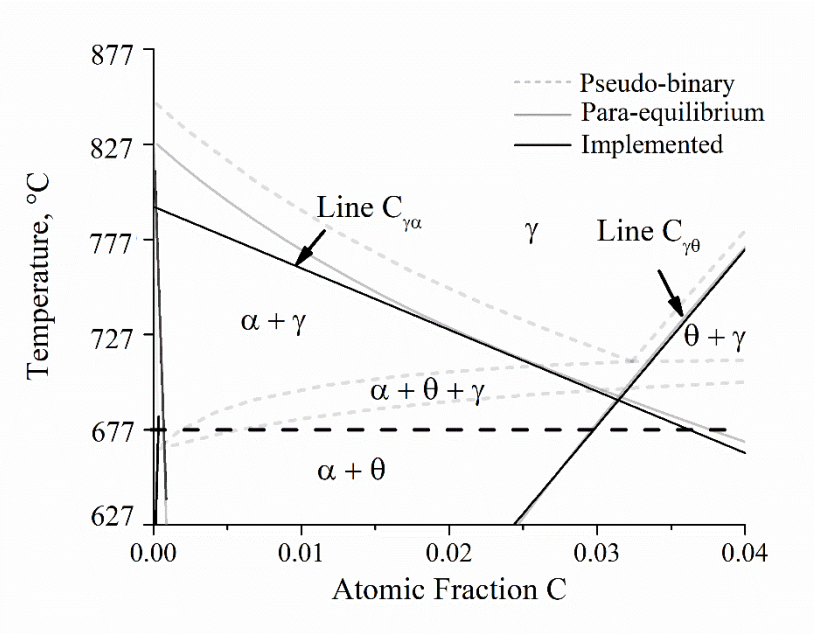

Fig. 6.2: The phase equilibria for the studied rail steel. An equilibrium pseudo-binary Fe-C diagram is plotted in light gray. The para -binary Fe-C diagram is shown as dark gray lines. The dark solid lines represent the implemented phase diagram in the phase field simulation, which is linearized from the phase para- binary Fe-C diagram. The horizontal dotted line indicates the reference temperature of this simulation at 677 °C.

The driving pressure ΔG_{ij} in equation 6.1 depends on the temperature of the system and the local composition at position ***r*** and time ***t***. The evolution of phases' compositions and the required phase diagram can be derived by combing MICRESS® with a thermodynamic database, Thermo-Calc® in this case. In the current study, the driving pressure for the phase transformation was calculated by using linearized phase diagrams. Under the fast heating conditions as occurring in rail steels, diffusion of alloying elements other than carbon is very limited [12]. As a result, a para-equilibrium quasi-binary iron-carbon phase diagram was used as the phase diagram for the simulations. The driving pressure can be obtained via:

$$\Delta G_{ij}(x^c, T) = \Delta S_{ij}\left(T^{Ref} + 0.5\left[m_i^{Fe-C}\left(x_i^C - x_i^{C^{ref}}\right) + m_j^{Fe-C}\left(x_j^C - x_j^{C^{ref}}\right)\right] - T\right) \quad (6.5)$$

T^{Ref} is the reference temperature, m_i^{Fe-C} and m_j^{Fe-C} are the slopes of lines separating the two phase regions in the equilibrium phase diagram from the single phase region of the phases of grain *i* and *j* , x_i^C and x_j^C are the local carbon content in grain *i* and *j*, $x_i^{C^{ref}}$ and $x_j^{C^{ref}}$ are the equilibrium carbon content in the grain *i* and *j* at the reference temperature.

6.2.3 Austenite nucleation

Austenite will form when the initial pearlite is heated to temperatures above the critical temperature, A_1. The austenitization process from a pearlitic type microstructure typically consists of nucleation and growth stages [12]. Experimental findings, e.g. synchrotron X-ray diffraction, commonly identify preferred austenite nucleation at α/α grain boundaries, ferrite/cementite phase boundaries and pro-eutectoid ferrite and pearlite boundaries, if they are present. In the phase field modeling, the nucleation rate is expressed by the Classical Nucleation Theory (CNT) [12,20]:

$$\dot{N} = N_n \beta^* Z \exp\left(\frac{-\Delta G^*}{kT}\right) \quad (6.6)$$

where N_n is the density of potential nucleation sites, $\beta^*$is the frequency factor (the rate at which single atoms are added to the critical nucleus), Z is the Zeldovich non-equilibrium factor, which corrects the equilibrium nucleation rate for nuclei that grow beyond the critical size, ΔG^* is the activation barrier and is related to the chemical Gibbs free energy difference, ΔG, by :

$$\Delta G^* = \frac{\psi_i}{(\Delta G)^2} \quad , \quad (6.7)$$

where ψ takes into account the geometric effects and the interfacial energies of the newly generated interfaces during nucleation. ΔG is the driving pressure for the nucleation.

The nuclei density input to the phase field simulation usually requires validation from experimental observations. However, the accurate nuclei density of austenite during ultra-fast heating cannot be obtained through experiments, since an in-situ or interrupted measurement is almost impossible. Instead, this study focuses on the compositional characteristics of the microstructure under continuous heating. In the MICRESS® software, the nuclei density can be set by setting parameters of 'shielding distance' and 'shielding time', which are set to be 0.5 μm and 2 s respectively in this study. This corresponds to a nucleus density of 0.08 μm^{-2}.

6.2.4. Martensite

The heating and cooling occurring at an identical rail surface site during wheel passages are cyclic and the heating and cooling rates are extremely high, e.g. [1,5]. The pearlite may partially or fully transform to austenite, depending on the temperature-time path. During the subsequent fast quenching, the austenite, partially or fully, transforms to martensite.

The difficulty of introducing a martensite phase into the PFM is the scarce kinetic data for the martensite to austenite transformations [20]. Thiessen et al. introduce an artificial martensite phase to represent the martensite-ferrite microstructure mixture in their dual phase steel [20]. They treated the martensite as a BCC-ferrite phase with the eutectoid carbon concentration. The introduction of supersaturated carbon in the modeled martensite has consequences. Figs. 6.3 (a) and (b) show schematically the Gibbs energy curves of different phases below and above A_1 temperatures. When the temperature is below A_1, the excess carbon will precipitate in carbides, with a driving pressure of $\Delta G(Fe_3C)$. When the temperature

reaches above A_1, the martensite has an additional driving pressure, $\Delta G(\gamma)$, for austenite formation, comparing that for ferrite to austenite transformation.

The carbide precipitation is, however, very unlikely for the WEL formation, due to the exerted extremely high heating rates, typically $10^5 – 10^6$ °C /s. In [25], cementite precipitation is experimentally shown not to occur when the heating rate is over 15 °C/s in Fe-(5-9)Mn-0.005C (in wt%). Hence, carbide precipitation during heating will be excluded from the current simulations.

In this study, the route of introducing martensite in [20] is adopted while its chemical composition was treated differently. Instead of assigning a uniform eutectoid carbon content to the martensite, the grain structure and the carbon concentration in the formed austenite during the previous heating cycle is assigned to martensite.

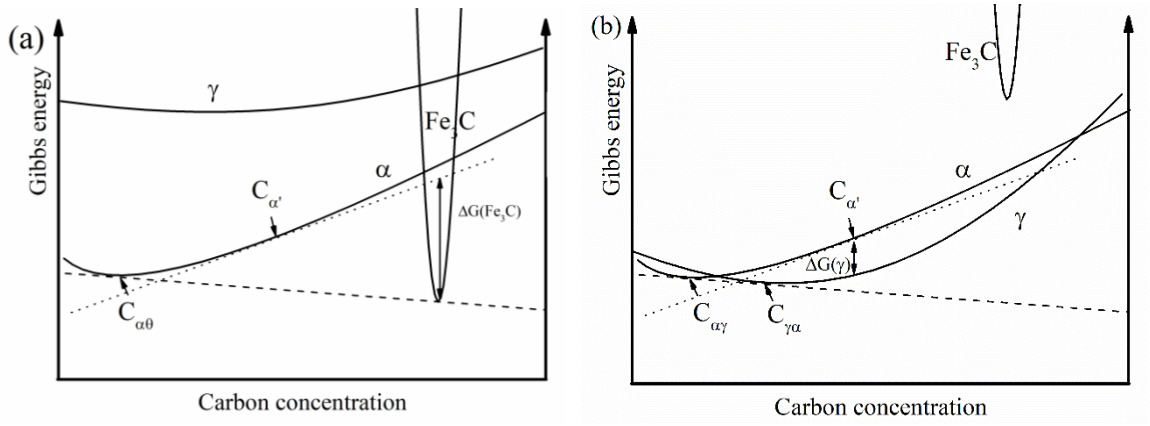

Fig.6.3: Schematic diagram of Gibbs energy of the phases below A_1 in (a) and above A_1 in (b). $C_{a'}$ represents a martensite with carbon supersaturation. $\Delta G(Fe_3C)$ and $\Delta G(\gamma)$are the additional Gibbs energy to form carbide and austenite respectively.

6.2.5. Simulation conditions and experimental settings

The pearlite to austenite and the pearlite + martensite to austenite transformation are simulated under continuous heating conditions and martensite forming during cooling is considered to fully inherit the structure and composition of the formed austenite. The austenite is set to nucleate at α/θ boundaries. It has been predicted [26] that, with a train speed of 140 km/h, the identical rail surface portion tends to be heated to a similar temperature during different wheel passages, if the loading conditions and the rail profile are unchanged during the train passages. It is also shown that the previous wheel pass has limited influence on the temperature change due to the arrival of a subsequent wheel. As a result, the starting temperature is considered to be identical for all simulations.

It was found that a very high heating rate, 10^5 °C/s and above, does not lead to transformation with MICRESS®, probably due to the fact that the nucleation of austenite is not able to occur because of the very high heating rate. Instead, the current simulation uses a relatively high heating rate, 2000 °C /s, in a combination with simulations at a lower heating rate of 10 °C /s, in order to gain insight into the effect of the heating rate on the austenite formation. The microstructure model in Fig. 6.1 has periodic

boundaries in the vertical direction and the horizontal boundaries were set to be isolated. The cementite phase is set to be stoichiometric and no carbon diffusion will occur in the cementite during the simulation. For the heating rate of 10 °C /s, a dilatometry curve was experimentally obtained under the same heat treatment in a DIL-805 A/D dilatometer. The austenite fraction can be extracted by analyzing the dilatometric curve during continuous heating, by lever rule after [12]. Fig. 6.4 shows the quantified austenite fraction and the output from the phase field modeling, with the heating rate of 10 °C /s. The good match was obtained by adjusting the nucleation density as a fitting parameter. It should be noted that recrystallization is not considered in the current simulation.

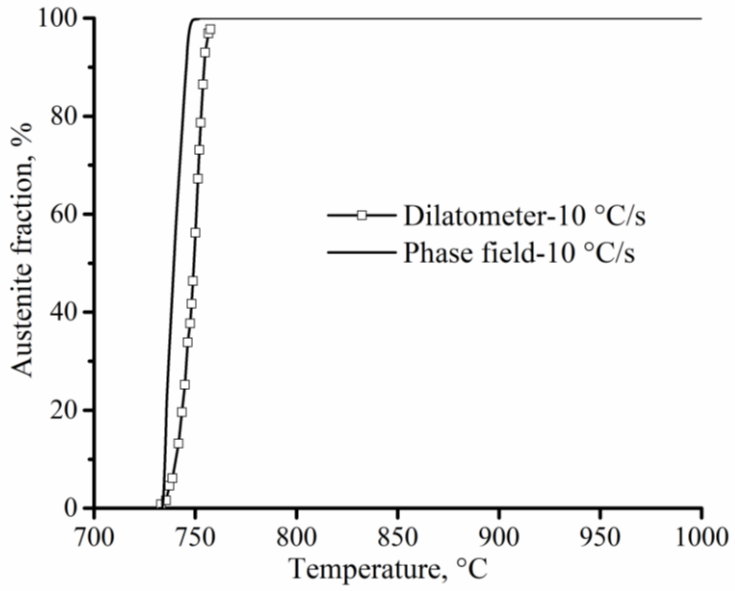

Fig. 6.4: Comparison of austenite fraction between experimental measurement and simulation result during heating at 10 °C /s.

The γ → α or the reverse transformation is typical to have mixed mode characteristics, rather than a pure diffusional or an interface controlled character [28]. A mode parameter, *S*, is frequently used to indicate the transformation characteristics of γ → α or α → γ transformation, the details about which are represented in e.g. [28,29]. In ref [29], pearlite microstructure is introduced as part of the initial microstructures to study the characteristics during pearlite + ferrite → austenite transformation. The pearlite is, however, treated as a single phase with an average eutectoid carbon concentration in the simulations. As a result, the transformation kinetics from pearlitic ferrite and cementite is not resolved separately and is consequently different from the simulated transformation in this chapter. Furthermore, the continuous cementite dissolution during the austenitization provides extra carbon into the existing austenite/ferrite system, making the calculation of the *S* parameter unrealistic. Alternatively, pure diffusion-controlled and interface-controlled phase transformation during the pearlite to austenite transformation was realized by modifying the pre-factor of the interface mobility $\mu_{\alpha\gamma}^{0}$ of γ/α interface in

equation (6.2): (1) μ_{ij}^{0} is multiplied by 100, so that the transformation is close to the diffusion-controlled process, (2) μ_{ij}^{0} is multiplied by 0.01 so that the transformation is close to the interface-controlled process. The transformation characteristics of the pearlite to austenite reaction for the WEL formation is indicated by comparing the carbon concentration in austenite at the γ/α interface with austenite carbon concentration in the above two extreme cases and the case of the original parameters.

6.3. Results and discussion

It should be pointed out first that a full representation of the thermal conditions for the pearlite to austenite transformation at a given rail surface point is impossible. The wheel/rail contact is dynamic and the actual thermal cycles during the wheel passages are constantly varying. Instead, the current simulation provides a semi-quantitative insight into the characteristics of austenite formation, under the fast heating process. During subsequent cooling, the formed austenite transforms to martensite via a diffusionless process and the composition of the parent austenite is considered to be inherited by the martensite product phase. In the subsequent sections, first comparisons with experimental results of the pearlite to austenite transformation will be made, to verify the used parameters, with a heating rate of 10 °C/s. The insight into the consequence of heating rates in WEL formation will be discussed, based on comparisons of results from the higher heating rate of 2000 °C/s and the lower rate of 10 °C/s.

6.3.1. Pearlite to austenite transformation at a low heating rate, 10 °C /s

Figs. 6.4(a-d) show the carbon maps of the microstructure, after being heated to different temperatures above the A_1 temperature, with a heating rate of 10 °C /s. The initial ferrite and cementite lamellae can be recognized by the lamellar morphology. The austenite can be identified by the different grayscale, due to the carbon concentration being distinctly different from the ferrite and cementite. The austenite is set to nucleate at the α/θ and α/α boundaries, Figs. 6.5(a) and (b). As temperature increases, the austenite grows faster into ferrite than into cementite, Figs. 6.5 (b–d), and a slower cementite to austenite transformation can be noticed in Figs. 6.5. In Fig. 6.5 (d), the ferrite lamellae are nearly completely transformed to austenite, while untransformed cementite remains. Such finding is in accordance with the experimental observations of Savran in [12] and can be contributed to the required limited carbon redistribution between cementite and austenite and the inadequate diffusion time of carbon in the austenite.

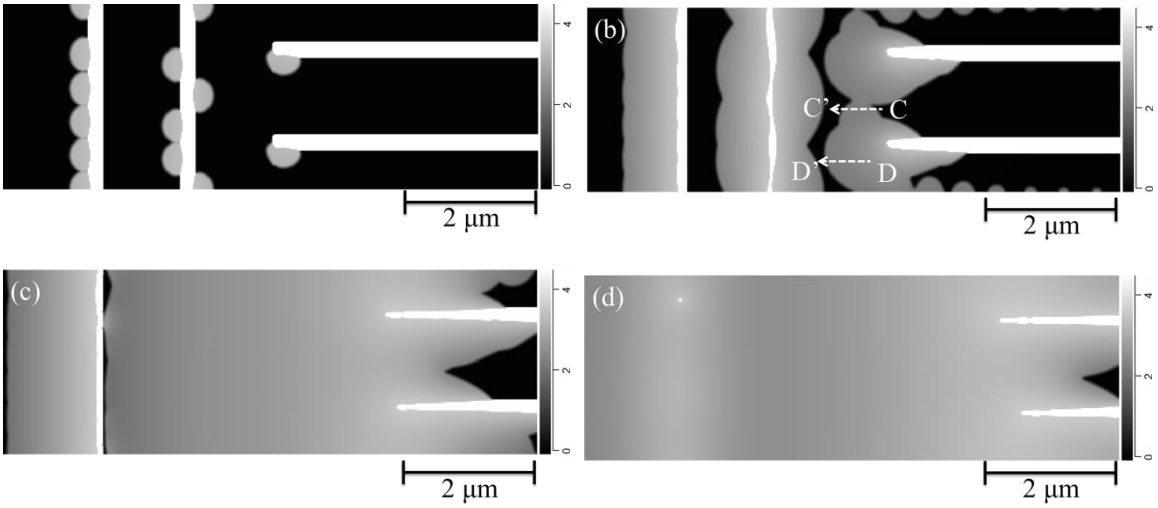

Fig. 6.5: Carbon distribution map of microstructure after being heated to austenitizing temperatures: (a) 735 °C; (b) 739 °C; (c) 746 °C; (d) 748 °C, with a heating rate of 10 °C/s. The vertical scale bar is in at%.

The carbon concentration in the austenite in equilibrium with ferrite, $C_{\gamma\alpha}$, and cementite $C_{\gamma\theta}$, can be estimated from the implemented phase diagram in Fig. 6.2, along the line between the (α + γ)/γ and (γ + θ)/γ phase region boundaries respectively. Following Fig. 6.2, $C_{\gamma\alpha}$ reduces as temperature increases, while $C_{\gamma\theta}$ increases in line with temperature and is significantly higher than $C_{\gamma\alpha}$. Only if the transformation is complete, the carbon concentration equals to the average carbon concentration in austenite in the steel. For the studied R260Mn grade rail steel, the overall carbon concentration is 3.04 at%.

The carbon in the formed austenite can be seen to be heterogeneous, by looking at the gray scales in the carbon maps in Figs. 6.5 (a-d). The austenite grains formed at α/α boundary is darker, i.e. has a lower carbon concentration, than austenite formed at α/θ boundary. Figs. 6.6(a) and (b) show two separate examples of carbon concentrations in the austenite formed at the α/α and α/θ boundaries. The equilibrium carbon concentration in austenite in equilibrium with cementite and ferrite at the plotted temperatures are added as references.

Fig. 6.6(a) shows the carbon concentration evolution in the austenite, nucleated at an α/θ boundary in line with temperature, along line D-D' in Fig. 6.5(a). Carbon in the austenite at temperature 1007.2 K corresponds to the slightly grown austenite. The carbon concentrations in austenite at all plotted temperatures are lower than the plotted equilibrium carbon concentrations. As temperature increases, the austenite further grows away from the cementite and the carbon concentration reduces. A carbon concentration gradient in the austenite can be observed. Fig. 6.6(b) shows another example of carbon evolution in austenite, nucleated at an α/α boundary, along the line C-C' in Fig. 6.5(b). The carbon concentrations in austenite at all plotted temperatures are higher than the equilibrium concentrations.

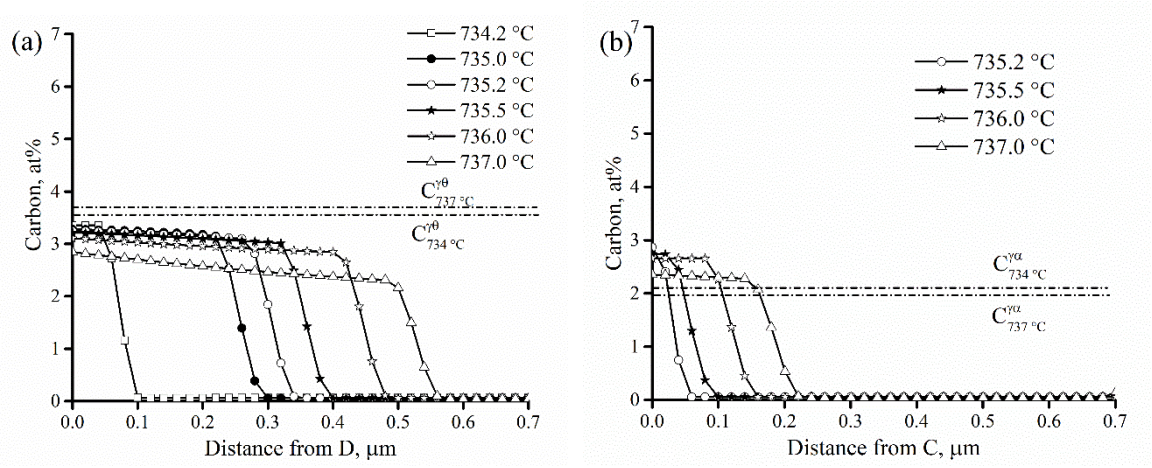

Fig. 6.6: Carbon distribution in austenite during continuous heating at 10 °C/s: (a) along line D-D' and (b) line C–C' in Fig. 6.5 (a) and (b) respectively.

6.3.2. Pearlite to austenite transformation at a high heating rate, 2000 °C /s

Figs. 6.7(a–c) show the carbon map of the microstructure heated to different temperatures above the A_1 temperature, with a heating rate of 2000 °C/s. Austenite was set to start nucleating at 774 °C, which is higher than the temperature for the heating rate of 10 °C/s in Fig. 6.5, due to the higher heating rate [27]. The lamellar ferrite and cementite and the newly formed austenite can be recognized by the morphology and the gray scale due to different carbon concentrations of the three phases. Alike the simulation with a heating rate of 10 °C/s, the austenite nucleates at the α/θ and α/α boundaries, e.g. Figs. 6.7(a) and (b). As the temperature increases, austenite grows faster into the ferrite than into the cementite, Fig. 6.7 (b–c).

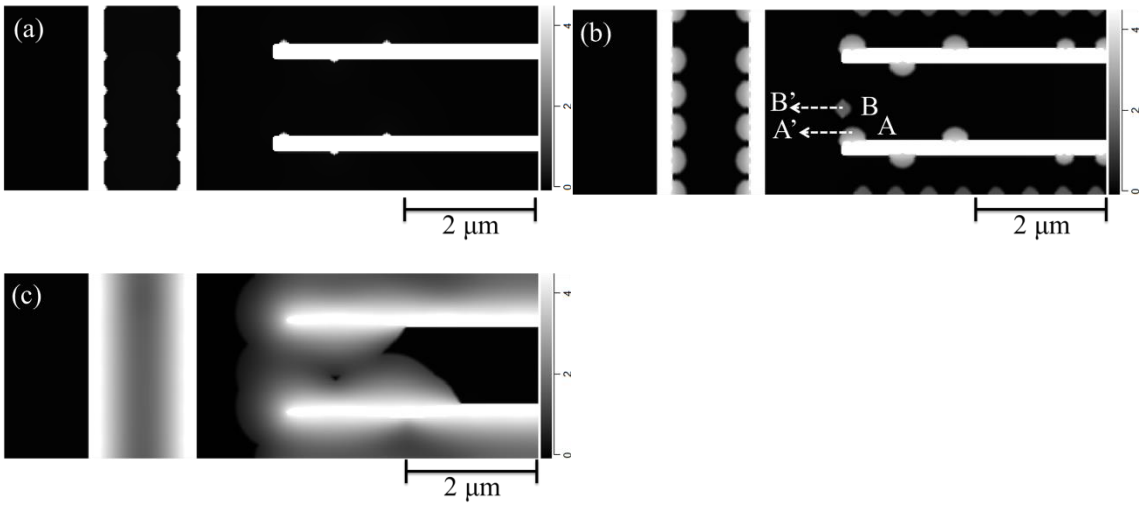

Fig. 6.7: Carbon distribution map of microstructure after being heated to austenitizing temperatures: (a) 778 °C; (b) 806 °C; (c) 862 °C, with a heating rate of 2000 °C/s.

Figs. 6.8 (a) and (b) show the carbon profiles along A-A' and B-B' lines in Fig. 6.7(b) at different temperatures, to show the different carbon concentration profile of austenite nucleated at the α/θ

boundary and the α/α boundary respectively. Alike the case of 10 °C/s in Fig. 6.6 (a) and (b), the austenite formed at an α/θ boundary has a higher carbon than that nucleated at an α/α boundary, whereas the difference is more significant in the case of 2000 °C/s than at 10 °C/s.

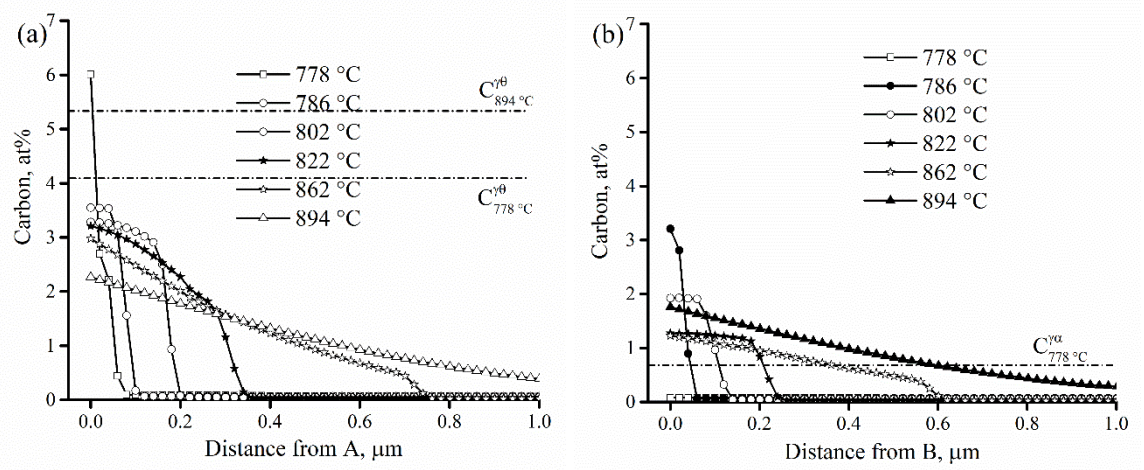

Fig. 6.8: Carbon distribution in austenite: (a) along line A-A' and (b) line B – B' in Fig. 6.8 (b), during heating at 2000 °C /s.

Transformations from ferrite (α) and cementite (θ) in the initial pearlite to austenite (γ) require simultaneous crystal lattice reconstruction, e.g. body-centered cubic (α) to face-centered cubic (γ), and carbon partitioning. It can be well expected that the carbon content in austenite nucleated at an α/θ boundary, Fig. 6.6(a) and Fig. 6.8(a), is higher than in that nucleated at an α/α boundary, Fig. 6.6(b) and Fig. 6.8(b), following the phase diagram in Fig. 6.2. When temperature further increases, austenite grows predominantly into the ferrite, Fig. 6.5 and Fig.6.7.

Austenite formed at the α/θ boundary grows faster than the austenite nucleated at the α/α boundary, for example by comparing Fig. 6.5(a) and (b): heating from 735.2 °C to 737.0 °C, the austenite in Fig. 6.6(a) grows 260 nm, while it grows 161 nm in Fig. 6.6(b) within the same temperature intervals. Austenite first nucleates at a relatively lower temperature during continuous heating. The carbon concentration in austenite nucleated at an α/θ boundary is expected to be significantly higher than austenite formed at an α/α boundary, Fig. 6.2. As temperature increases, the α/γ interface proceeds predominantly into ferrite region and the carbon concentration within the interface is expected to be in equilibrium between ferrite and austenite. As a result, a more pronounced carbon concentration gradient, Δx, in the austenite formed at cemenite formes builds up, than austenite nucleate in ferrite, providing a higher interface movement velocity [28]:

$$v = M\omega\Delta x \qquad (6.8)$$

in which M is the interface mobility and ω is a thermodynamic proportionally factor.

Figs. 6.9(a) and (b) show the carbon concentration profiles along line D – D' at 10 °C/s and line A–A' at 2000 °C/s respectively. The open and filled circles in both figures are the carbon concentrations in austenite at the γ/α interface, predicted by diffusion-controlled and interface-controlled kinetics

respectively. It can be seen that at the heating rate of 10 °C/s, the austenite carbon concentration is in between the two extreme cases, Fig. 6.9(a). The carbon concentration in the austenite at the heating rate of 2000 °C/s is closer to interface-controlled conditions, Fig. 6.9(b). This indicates that the increased heating rate can shift the pearlite to austenite formation closer to the interface-controlled characteristics.

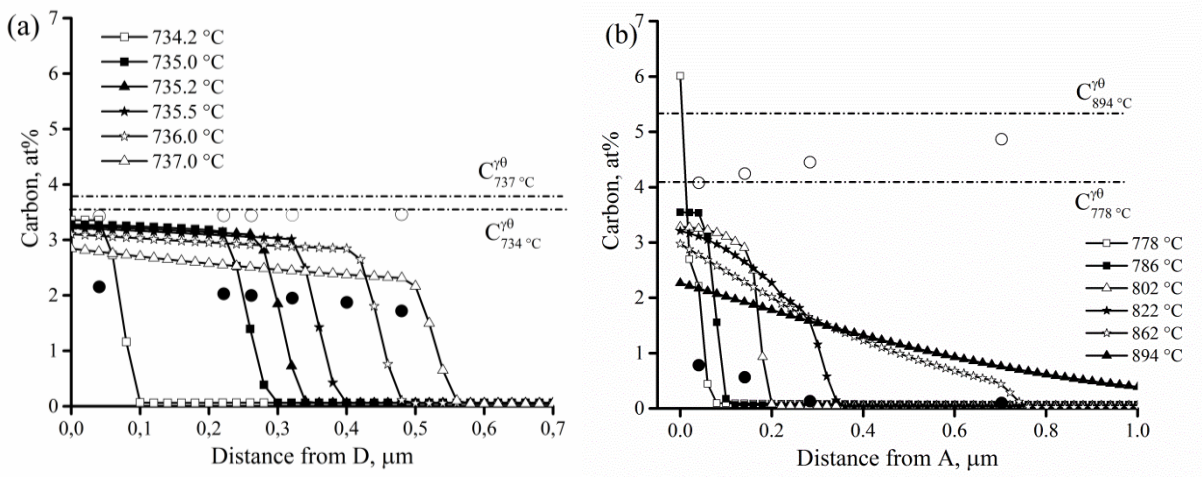

Fig.6.9 Comparisons of carbon concentration in austenite with predicted carbon concentration in austenite at γ/α interface due to diffusion-controlled (open circle) and interface-controlled transformation (filled circle) along line D – D' at 10 °C/s in (a) and along A–A' at 2000 °C/s.

6.3.3. Martensite to austenite transformation

The martensite is considered in the current phase field simulations as a BCC phase with the carbon concentration of the prior austenite, which causes the BCC phase to be supersaturated. The martensite substructure, e.g. high dislocation density [30], lath/twinning structures [14,31], cannot be included in the MICRESS® software. The substructures may have some effects on the formation of austenite, and the martensite to austenite transformation kinetics during heating in a subsequent wheel passage may be underestimated in the current simulation. However, similar simplifications, e.g. by Thiessen et al. [20], are shown to be able to establish a reasonable match between the simulation and experimental results.

Figs. 6.10 (a – f) show the carbon concentration map and the distribution of the phases in the microstructure, with the heating rate of 2000 °C/s during a second wheel passage. The grain structure and carbon concentration of α' martensite are inherited from the simulations in Section 6.3.2, heated to 762 °C, and are shown in Fig. 6.10(a). The carbon in the martensite diffuses into the adjacent ferrite when the temperature increases, if martensite is not transformed to austenite, Fig. 6.10(b), in spite of the instability caused by the carbon supersaturation. The carbon of the austenite that forms in the martensite has a very high concentration, exceeding 10 at%, Figs. 6.10(c-e). The austenite further grows and the carbon diffuses when the individual austenite grains interact. The carbon concentration in the austenite in Fig. 6.10(f) is 3–5 at%.

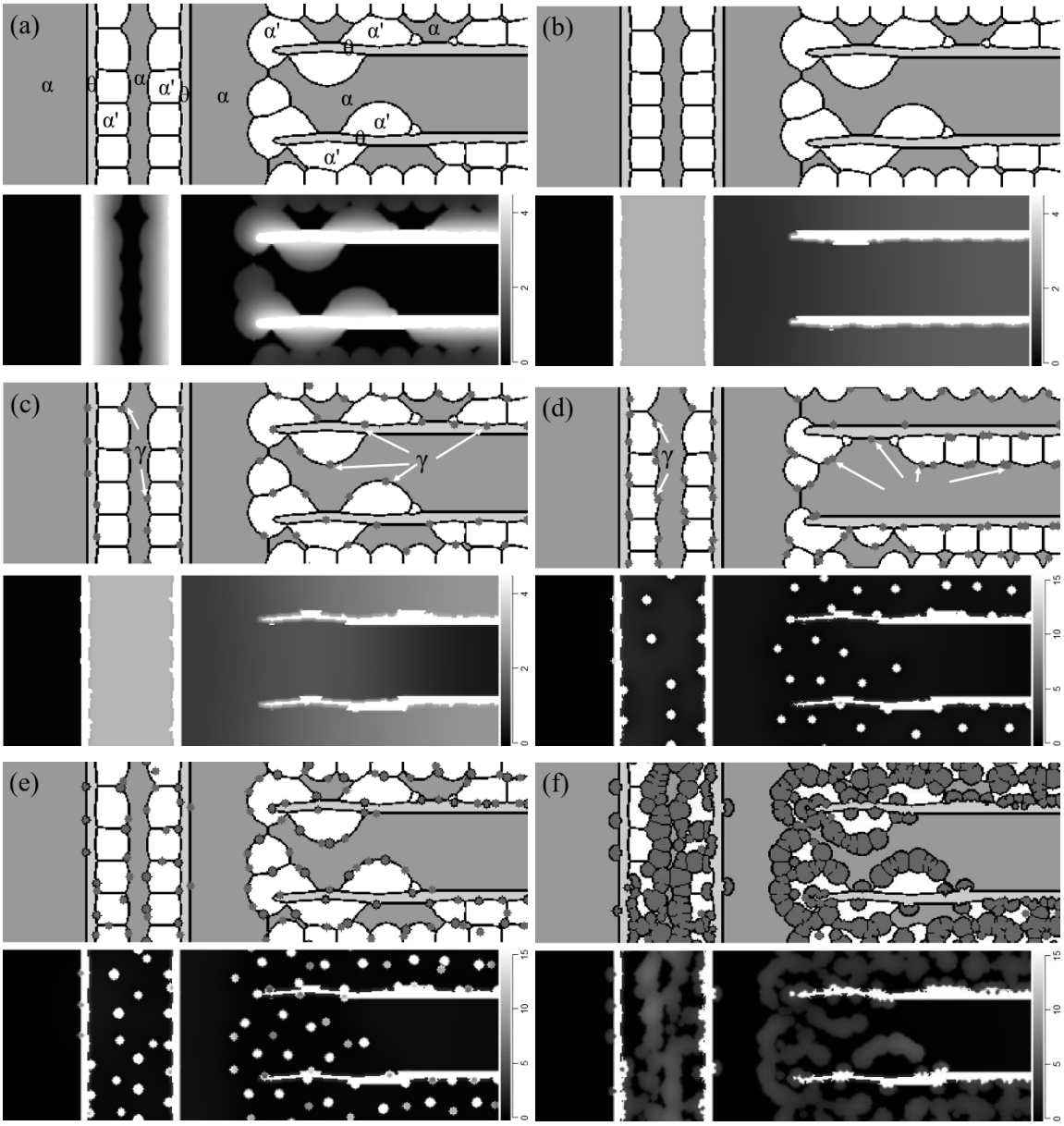

Fig. 6.10: Carbon concentration and phase distribution map of microstructure after being heated to temperature below austenitizing temperatures: (a) 762 °C; (b) 766 °C and temperatures above the austenitizing point during the second wheel passage: (c) 774 °C; (d) 776 °C; (e) 778 °C and 794 °C (f), with a heating rate of 2000 °C/s.

The major insight resulting from including the martensite in this study is that the austenite formed from martensite will have a higher carbon concentration than austenite forming from ferrite. Such conclusions can be drawn by looking at the calculated Gibbs free energy curve of a Fe – C system at temperature 1016 K in Fig. 6.11, which is above the A_1 temperature. The austenite, formed at ferrite with an equilibrium carbon concentration, $C_{\alpha\gamma}$ is expected to have a carbon concentration of $C_{\gamma\alpha}$. With a BCC phase supersaturated carbon in carbon, e.g. $C_{\alpha'}$ in Fig. 6.11, the according carbon concentration in the formed austenite should be $C_{\gamma\alpha'}$, which is higher than $C_{\gamma\alpha}$. Martensite transformed from the austenite

with $C_{\gamma\alpha'}$, will be harder than that formed from austenite with $C_{\gamma\alpha}$. This will also lead to formation of martensite with heterogeneous mechanical properties.

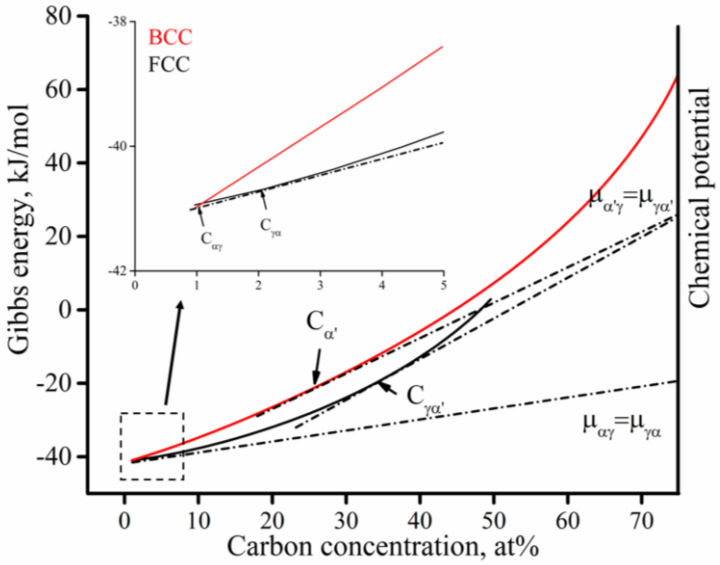

Fig. 6.11: Calculated Gibbs energy curves of BCC-ferrite and FCC-austenite at 1016 K of a Fe-C system, which is above the A_1 temperature. $C_{\alpha\gamma}$ and $C_{\gamma\alpha}$ corresponding to the equilibrium carbon concentration in ferrite and austenite when they have same chemical potential. $C_{\alpha'}$ represents the carbon concentration of martensite and $C_{\gamma\alpha'}$ is the carbon concentration in equilibrium with $C_{\alpha'}$.

6.3.4. Insight into the formation of WEL in rails

The current simulations provide the following insight into the formation of WEL via the mechanism of the thermally-induced martensitic phase transformation. By comparing the results of heating rates of 10 °C/s and 2000 °C/s, it can be concluded that the accelerated heating rate can have the following consequences: *(i)* A slower austenite formation rate with increased heating rate in line with temperature. The higher heating rate increases the A_{c1} temperature [27] and limits the carbon diffusion distance in the austenite, leading to delayed austenite formation. As a result, only a minor fraction of the pearlite transforms to austenite and the full austenitization requires a higher temperature or longer time for the austenite to grow. The WEL is observed only after certain loading history after implementation and is most probably due to the extremely short contact time during a single wheel passage, i.e. limited fraction of austenite and subsequently martensite. *(ii)* A more significant heterogeneity of carbon concentration in the WEL after final heating, both in WEL at different rail surface portions and in WEL at different rail depth, e.g. [1]. As discussed above, such differences must be related to the previous temperature and loading history for the formation. *(iii)* The subsequent heterogeneous mechanical properties within a single WEL block. This can be due to the significant variations in carbon concentration in the formed austenite during pearlite to austenite and also martensite to austenite formations.

6.4. Summary and conclusions

White etching layer in rail steels, formed due to thermally-induced martensitic phase transformation mechanism, has been (semi) quantitatively studied by a phase-field modeling approach. A validation of the used nucleation density, mobility and interfacial energy was firstly done by comparing with the dilatometric measurement with a heating rate of 10 °C/s. The subsequent insight into WEL formation is mainly gained from simulation results of pearlite to austenite transformation at a heating rate of 2000 °C/s and its comparison with that of 10 °C/s. Simulation with both heating rates shows faster ferrite to austenite transformation, than cementite to austenite transformation. The simulation results indicate a switch from diffusion-controlled to the interface-controlled pearlite to austenite transformation, as heating rate increases significantly. The carbon concentration and the corresponding mechanical properties in a single WEL block can be significantly different and depends on the loading condition.
The unfavorable WEL formation via this formation mechanism can be reduced both by optimizing the wheel/rail contact condition and metallurgical design. The wheel/rail contact optimization appears to be more advantageous since it also minimizes the undermined RCF in pearlite due to the thermal softening. The metallurgical design mainly delays WEL formation by raising the A_1 temperature and possibly reduces the austenite/ferrite interface mobility.

References

[1] Takahashi J, Kawakami K, Ueda M. Atom probe tomography analysis of the white etching layer in a rail track surface. Acta Mater 2010;58:3602–12.

[2] L, Wang L, Pyzalla A, Stadlbauer W, Werner EA. Microstructure features on rolling surfaces of railway rails subjected to heavy loading. Mater Sci Eng A 2003;359:31–43.

[3] Ahlstroem J. Residual stresses generated by repeated local heating events - Modelling of possible mechanisms for crack initiation. Wear 2016;366–367:180–7.

[4] Ahlström J, Karlsson B. Microstructural evaluation and interpretation of the mechanically and thermally affected zone under railway wheel flats. Wear 1999;232:1–14.

[5] Wu J, Petrov RH, Naeimi M, Li Z, Dollevoet R, Sietsma J. Laboratory simulation of martensite formation of white etching layer in rail steel. Int J Fatigue 2016;91:11–20.

[6] Carroll RI, Beynon JH. Rolling contact fatigue of white etching layer: Part 1. Crack morphology. Wear 2007;262:1253–66.

[7] Ishida M. Rolling contact fatigue (RCF) defects of rails in Japanese railways and its mitigation strategies. Electron J Struct Eng 2013;13:67–74.

[8] Steenbergen M, Dollevoet R. On the mechanism of squat formation on train rails – Part I: Origination. Int J Fatigue 2013;47:361–72.

[9] Daniel W, Kerr M, Daniel AW. Final Report on the Rail Squat Project R3-105. 2013.

[10] Carroll RI, Beynon JH. Rolling contact fatigue of white etching layer: Part 2. Numerical results. Wear 2007;262:1267–73.

[11] Seo J, Kwon S, Jun H, Lee D. Numerical stress analysis and rolling contact fatigue of White Etching Layer on rail steel. Int J Fatigue 2011;33:203–11.

[12] Savran V. Austenite formation in C-Mn steel. Ph.D. thesis. Delft University of Technology, 2009.

[13] Porter DA, Easterling KE, Sherif M. Phase Transformations in Metals and Alloys, (Revised Reprint). CRC press; 2009.

[14] Krauss G. Martensite in steel: strength and structure. Mater Sci Eng A 1999;273–275:40–57.

[15] Zhang HW, Ohsaki S, Mitao S, Ohnuma M, Hono K. Microstructural investigation of white etching layer on pearlite steel rail. Mater Sci Eng A 2006;421:191–9.

[16] Militzer M. Phase field modeling of microstructure evolution in steels. Curr Opin Solid State Mater Sci 2011;15:106–15.

[17] Huang CJ, Browne DJ, McFadden S. A phase-field simulation of austenite to ferrite transformation kinetics in low carbon steels. Acta Mater 2006;54:11–21.

[18] Militzer M, Mecozzi MG, Sietsma J, van der Zwaag S. Three-dimensional phase field modelling of the austenite-to-ferrite transformation. Acta Mater 2006;54:3961–72.

[19] Mecozzi MG, Sietsma J, Zwaag S, Apel M, Schaffnit P, Steinbach I. Analysis of the $\gamma \rightarrow \alpha$ transformation in a C-Mn steel by phase-field modeling. Metall Mater Trans A 2005;36:2327–40.

[20] Thiessen RG, Sietsma J, Palmer TA, Elmer JW, Richardson IM. Phase-field modelling and synchrotron validation of phase transformations in martensitic dual-phase steel. Acta Mater 2007;55:601–14.

[21] HAMID A-A. Ph.D. thesis. THE UNIVERSITY OF BRITISH COLUMBIA, 2010.

[22] Castro Cerda FM, Sabirov I, Goulas C, Sietsma J, Monsalve A, Petrov RH. Austenite formation in 0.2%

C and 0.45% C steels under conventional and ultrafast heating. Mater Des 2016;116:448–60.

[23] Militzer M, Azizi-Alizamini H. Phase Field Modelling of Austenite Formation in Low Carbon Steels. Solid-Solid Phase Transform. Inorg. Mater., vol. 172, Trans Tech Publications; 2011, p. 1050–9.

[24] Steinbach I, Pezzolla F, Nestler B, Seeßelberg M, Prieler R, Schmitz GJ, et al. A phase field concept for multiphase systems. Phys D Nonlinear Phenom 1996;94:135–47.

[25] Han J, Lee YK. The effects of the heating rate on the reverse transformation mechanism and the phase stability of reverted austenite in medium Mn steels. Acta Mater 2014;67:354–61.

[26] Naeimi M, Li Z, Dollevoet R, Wu J, Petrov R, Sietsma J. Thermo-mechanical effects in the formation mechanism of rail squats. Third Int Conf Railw Technol Res Dev Maint 2016;110:1–14.

[27] De Knijf D, Puype A, Föjer C, Petrov R. The influence of ultra-fast annealing prior to quenching and partitioning on the microstructure and mechanical properties. Mater Sci Eng A 2015;627:182–90.

[28] Sietsma J, van der Zwaag S. A concise model for mixed-mode phase transformations in the solid state. Acta Mater 2004;52:4143–52.

[29] M.G.Mecozzi. Ph.D. thesis, Phase field modelling of the austenite to ferrite transformation in steels. TU Delft, 2007.

[30] Morito Tanaka, H., Konishi, R., Furuhara, T., Maki, T. S. The morphology and crystallography of lath martensite in Fe-C alloys. Acta Mater 2003;51:1789–99.

[31] Miyamoto G, Iwata N, Takayama N, Furuhara T. Quantitative analysis of variant selection in ausformed lath martensite. Acta Mater 2012;60:1139–48.

Chapter 7 Investigation of brown etching layer: an additional insight

Abstract:
White etching layer (WEL) is a frequently observed structural change in rail surface and can cause rolling contact fatigue damage. WEL is named after its white appearance in the light microscope after revealing with Nital etchant. The two prevalent proposed formation mechanisms of white etching layer are either the martensitic phase transformation hypothesis or the severe plastic deformation mechanism. The controversy can be due to the different loading conditions of the rails, from which WEL specimen was extracted. In this chapter, a differently etched layer from WEL, named as brown etching layer (BEL), is reported. Unlike the classical WEL, the BEL has a brownish color under light microscope and is distinctly softer than WEL. The cracks associated with BEL can grow deeper into the rail, compared with the cracks caused by WEL in the literature. This indicates that the presence of BEL can be more dangerous than WEL to the rail lifetime. Electron backscatter diffraction identifies retained austenite and the kernel average misorientation mapping reveals deformation characteristics both in the BEL and the pearlite immediately underneath. The comparison of morphology and hardness of BEL with WEL indicate that BEL can be correlated to the WEL. The formation mechanism of BEL is proposed from the observed microstructure and is further correlated to the WEL.

Keywords: white etching layer; brown etching layer; electron backscatter diffraction; retained austenite; martensite; deformation; kernel average misorientation[3]

[3] This chapter is partly based on a scientific paper:
Li S, Wu J, Petrov RH, Li Z, Dollevoet R, Sietsma J. "Brown etching layer: A possible new insight into the crack initiation of rolling contact fatigue in rail steels?", Eng Fail Anal 2016;66:8–18.

7.1. Introduction

This chapter characterizes a different type of WEL, the brown etching layer (BEL) [1]. The BEL is named after its brownish color observed in the optical microscope after etching with Nital, e.g. the one in Fig. 7.1, and is in analogy to the naming of WEL in literature. The observed BEL exhibits most of the morphological features as the classical WEL in literature, such as a clear interface with the bulk material and the shape of isolated or continuous distributed "islands". Similar to the WEL [2,3], BEL is observed in rail surface and is subsequently considered to be another important source for rolling contact fatigue (RCF) initiation, as cracks are closely associated to the BEL, e.g. the ones in Fig. 7.1. Moreover, cracks associated with BEL, e.g. the top left big crack in Fig. 7.1, have been found to grow considerably deeper towards the rail depth, compared with the literature in which cracks caused by the WEL mostly propagate at a more limited depth only or cause spalling [2,3]. This indicates the possibly more detrimental role of BEL in the RCF development in rails than WEL. Consequently, more extensive rail grinding is expected for completely removing the cracks caused by BEL, leading to premature rail removals and more frequent rail replacements. Therefore, the study of the formation mechanism of the BEL is of practical concern and importance.

To the authors' knowledge, similar BELs as in this chapter were reported [4,5] but did not attract substantial attention. The BELs in the aforementioned publications and the present chapter are observed in rails with different traffic conditions, e.g. train speeds and annual axle load. This indicates that BEL is not related to a specific traffic condition. Furthermore, there is insufficient evidence in the existing publications to correlate the BEL to a specific rail steel grade. The observed BEL in the present chapter is shown with different features from those reported in the literature and will be elaborated in subsequent sections. In addition to the microstructural morphology, the mechanical characteristics of the BEL, measured by a micro-hardness test, is shown to be different from that of the well-known WEL. Considering that the mechanism for WEL formation in the literature remains controversial and depends on the loading conditions for the WEL formation, the discovery of the BEL arouses the questions as follows: Could an investigation of the BEL provide a possible additional insight into the formation of the WEL? To this end, microstructural features of the BEL were studied using micro-hardness tests, optical microscopy (OM), scanning electron microscopy (SEM) and electron backscatter diffraction (EBSD). This study is expected to provide an understanding of: 1) the microstructural features and mechanical properties of the BEL, 2) correlations between the WEL and the BEL, and 3) the possible formation mechanism of the BEL. The microstructural features of the BEL were compared with the WEL reported in the literature.

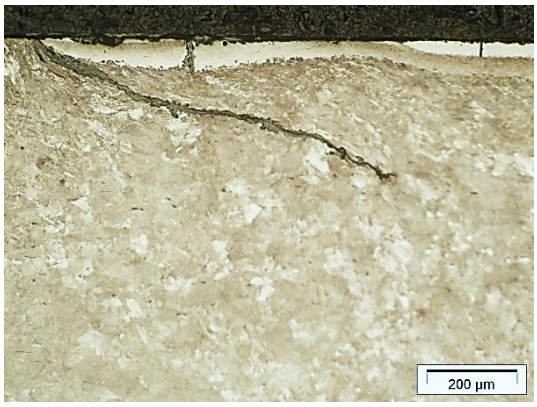

Fig.7.1 An example of brown etching layer observed in rail surface. Cracks are frequently observed to be associated with BEL.

7.2. Materials

The rail used for this investigation is an R260 Mn grade rail steel and was removed from a straight track in the Dutch railway network between Meppel and Leeuwarden in 2007. The track is a main passenger line, with a highest operating speed of 140 km/h. The line on average carried approximately 10,000 tons of loads per day. The period from the last grinding maintenance was estimated to have been more than 1 year. Therefore, the total tonnage is greater than 3.65 MGT.

The studied rail track had problems with corrugation on the rail surface, showing wave pattern with periodic shiny peaks and dark valleys when still in service, see for example the image in Fig. 7.2(a) which was taken while the rail was in-field. Such wave patterns are not visible anymore after removal of surface corrosion during the storage in open air for a long time. However, the wave patterns can be still recognized by using the RAILPROF measurement device. The measured surface profile of the rail track in Fig. 7.2(a) is superimposed in the same figure to show the original corrugation crests and valleys before removal. The surface profile in Fig. 7.2(a) was used as guidance for the subsequent sampling for metallographic analysis and Fig. 7.2(b) is the resembled rail piece after cutting. Longitudinal-vertical rail specimens with dimensions of $20\ \text{mm} \times 2\ \text{mm} \times 10\ \text{mm}$ in the longitudinal, lateral and vertical directions were cut for the characterizations. BELs are identified as being at the corrugation crest. The notations of RD, TD, and ND refer to the traffic/rolling direction, transfer direction and direction perpendicular to the rail surface respectively. These notations are kept through the rest of the chapter.

The microstructure of the specimens was first investigated with an Olympus BH-2 optical microscope and then in a JSM 6500F scanning electron microscope with field emission gun (FEG-SEM). Moreover, micro-hardness tests were performed using a Durascan 70 (Struers), with a load of 0.49 N and a loading duration of 10 s, to quantify the mechanical properties of the BEL. The hardness distribution along the depth within the BEL was measured. At each depth, minimum of 4 indentations were made.

The EBSD measurements in the BEL and pearlite beneath were done in a FEI Quanta-450 SEM equipped with a field emission gun (FEG) and the experimental settings were explained in Chapter 3.

In short, the EBSD measurements were done with a step size of 50 nm and a hexagonal scan grid mode and a working distance of 16 mm. The grains were defined as regions containing minimum of 4 pixels with an internal misorientation less than 5°, unless specifically mentioned otherwise.

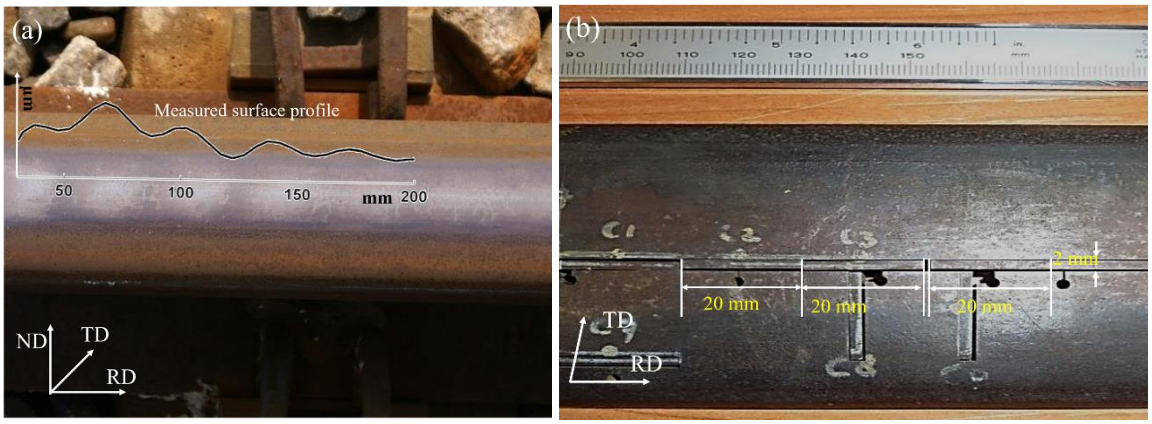

Fig. 7.2 (a) Photo of surface corrugation while the studied rail was in in-track in June 2007. The superimposed wave pattern was measured after the rail removal and storage in the open air for ~ 7 years; (b) Photo of specimens after cutting and resembling.

7.3. Results

7.3.1. Micro-hardness test

It should be first pointed out that, unlike the uniform contrast of WEL in the optical microscope (OM), Nital chemical reveals BEL as an alien structure with inhomogeneous color, e.g. Figs. 7.3 (a) and (c). A featureless white color zone is observed in some of the BEL islands, which is within the first few microns from the rail surface. Such white color zone is separated from the underneath brown color region in the BEL by a sharp boundary, for example as delineated by the red solid line in Fig. 7.3(a). In addition, this white zone has significantly different mechanical properties than that in the immediate beneath brown color zone, as identified by hardness measurements in this section. Accordingly, this zone is considered to be different from the underneath brown color zone and is named as white sublayer in the chapter, e.g. notations in Fig. 7.3(a). The white sublayer in Fig. 7.3(c) appears not as dominant as that in Fig. 7.3(a), because only part of the white sublayer is included in the viewed micrograph. This is due to the limited observed area under the adopted magnification for taking the picture. The white sublayer continues to the adjacent area in the same specimen.

The underneath brown color zone consists of the rest of the BEL and the bottom is separated from the matrix pearlite area by a clear boundary, for example as indicated by the dotted black line in Fig. 7.3(a). Furthermore, a whitish zone is observed at the bottom of the brown color area and is near the BEL/matrix boundary. However, the hardness in the brown color area, to be shown in this section, changes gradually along the rail depth and no abrupt hardness change is identified in the region. Consequently, this whitish zone is considered to belong to the main brown color zone and the notations in Figs. 7.3(a) and (c) will

be used throughout this chapter in which: *(i)* the white sublayer only refers to the topmost white area, which has a distinct boundary with the beneath brown color zone; *(ii)* the brown sublayer refers to the area below the white sublayer, including the area appearing whitish at the bottom of the BEL.

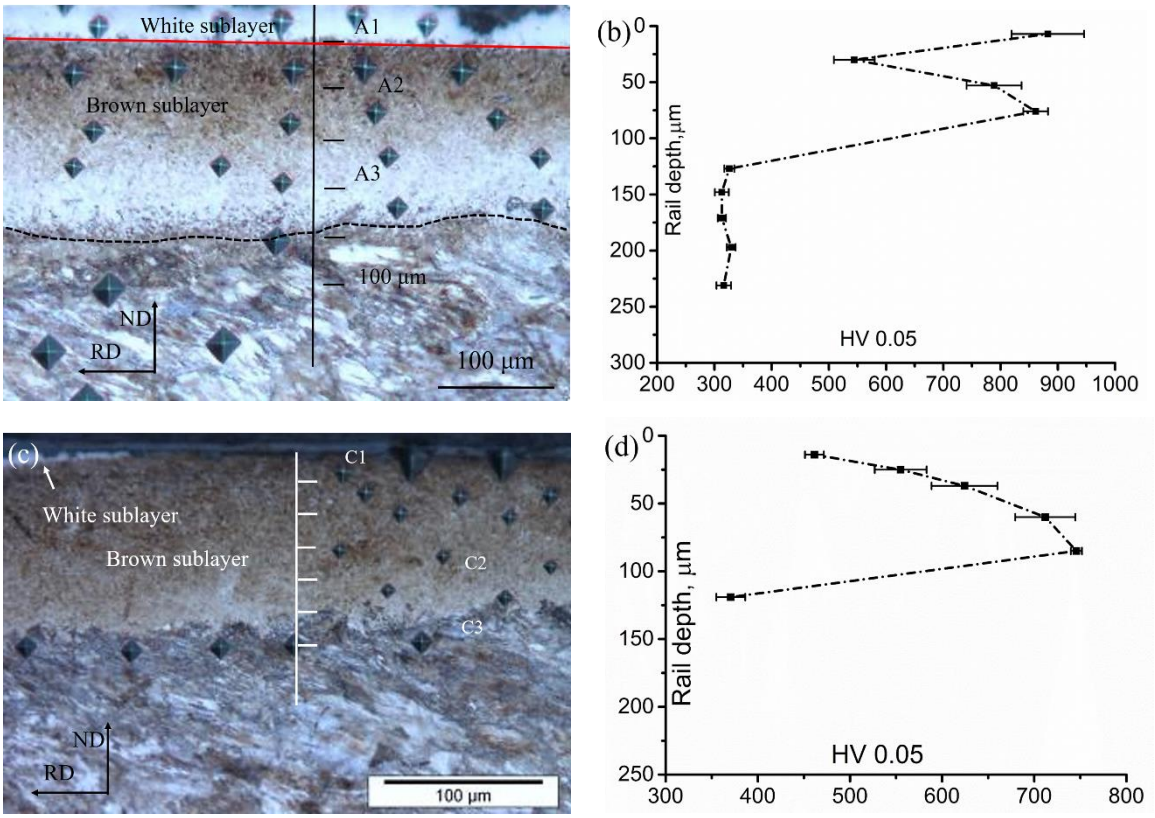

Fig. 7.3 (a) and (b) are optical micrographs and the hardness distribution plot of a BEL consisting of mixed sublayers; (c) and (d) are optical micrograph and the hardness distribution plot of a newly single-layer BEL.

The hardness distributions along rail depth in Figs 7.3(a) and (c) are shown in Figs. 7.3(b) and (d). The schematic scales in Figs 7.3(a) and (c) are added to show the spatial distribution of indentations and their depth positions are indicated by the superimposed letters in the same figures. The topmost white sublayer in Fig. 7.3(a) is identified to have the highest hardness among all the measurements, 880 ± 60 HV in Fig. 7.3(b). An abrupt hardness drop down to 540 ± 30HV is observed in the brown sublayer immediately below the white sublayer, above position A2 in Fig. 7.3(a). A further hardness increase can be observed in the brown sublayer along the rail depth and a maximum hardness, 840 ± 30 HV, is recognized in the BEL sublayer close by the BEL/pearlite boundary, i.e. close by zone A3 in Fig. 7.3(a). The hardness in the pearlite immediately under BEL, showing materials flow, shows no significant differences from the undeformed matrix observed at ~ 12 mm beneath the rail surface. The zone with the highest hardness within the materials flow area is measured to be close to the BEL/pearlite boundary

with a hardness of 326 ± 9 HV and is slightly higher than the measurements in the undeformed zone with hardness of 307 ± 15 HV.

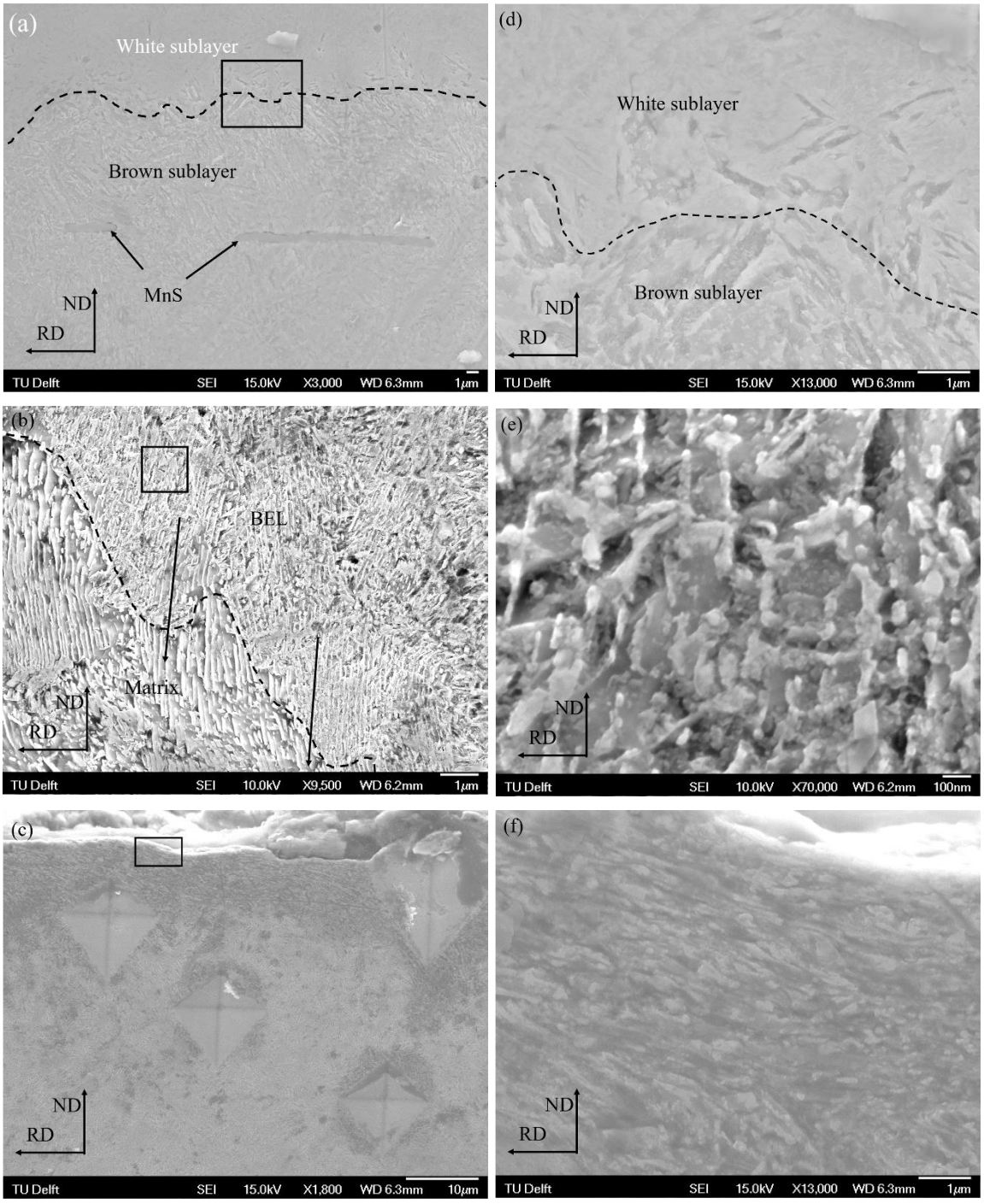

Fig. 7.4.SEM micrographs of areas: (a) close by positions A1 in Fig. 7.3(a); (b) close to position C3 in Fig. 7.3(c); (c) close to position C1 in Fig. 7.3(c); (d) – (f) are the magnified micrographs of areas within the empty black rectangles in (a) – (c) respectively.

The characteristics of hardness distribution in the surface brown sublayer in Fig. 7.3(c) (left top corner with a minor portion of white sublayer) are alike the brown sublayer in Fig. 7.3(a), after comparing the hardness profiles in Figs. 7.3(b) and (d): *(i)* the hardness of the brown color area decreases when approaching closer to the rail surface. The topmost layer is the softest, with a hardness as low as 450 ~ 470 HV; *(ii)* the highest hardness within the BEL appears near the BEL/matrix boundary. Hardness within this sub-region varies in the range of 740 ~ 752 HV, with an average hardness of 746 HV.

7.3.2. Morphological features of BEL in SEM

SEM observations were performed to characterize the microstructure within the BEL and to offer possible explanations of the hardness difference in BEL. The BELs consisting of the near single brown sublayer and mixed sublayers, Figs. 7.3(a) and (c), are both examined.

Figs. 7.4(a) and (d) are secondary electron images of BEL taken at the boundary of white color and brown color sublayer boundary, i.e. the red solid line in Fig. 7.3(a). The same boundary is again delineated by the black dotted line in Fig. 7.4(a) and (b). It can be seen that the topmost white sublayer is hardly influenced by the etching, showing a smooth surface topography in the secondary electron micrograph. On the contrary, the brown sublayer immediately beneath is more etched and has gully-like characteristics. Two elongated MnS inclusions, without any associated cracks, are observed to be parallel to the traffic direction and are indicated by the two black arrows in Fig. 7.4(a). Figs. 7.4(b) and (e) are SEM images taken close to area C3 in Fig. 7.3(c), in which part of the pearlite microstructure in the matrix is included and the BEL/matrix boundary is indicated by the dotted black line in Fig. 7.4(b). A lamella-type microstructure is observed in the BEL and is representative for the microstructures within the brown sublayers, e.g. zones A2 – A3 in Fig. 7.3(a) and zones C2 – C3 in Fig. 7.3(c). Continuation of some lamellae from the matrix into the BEL can be seen, for example as indicated by the arrows across the interface in Fig. 7.4(c). Finally, the microstructure in the topmost brown sublayer in Fig. 7.3(c), ~10 μm from the rail surface, is different from the other areas in the BEL. The SEM images in Figs. 7.4(c) and (f) show fiber-like features within the zone and are flattened in the traffic direction.

7.3.3 EBSD results

EBSD characterizations were done on the brown sublayer in Fig. 7.3(c), in order to reveal the microstructures and the possible microstructural differences in the layer. Figs. 7.5(a – c) show the grey scale image quality (IQ) maps of: (1) the topmost BEL (position C1 in Fig. 7.3(c)); (2) the subsurface BEL, which is around 80 μm beneath the rail surface (position C2 in Fig. 7.3(c)); (3) the pearlite area immediately beneath the BEL, respectively (position C3 in Fig. 7.3(c)).

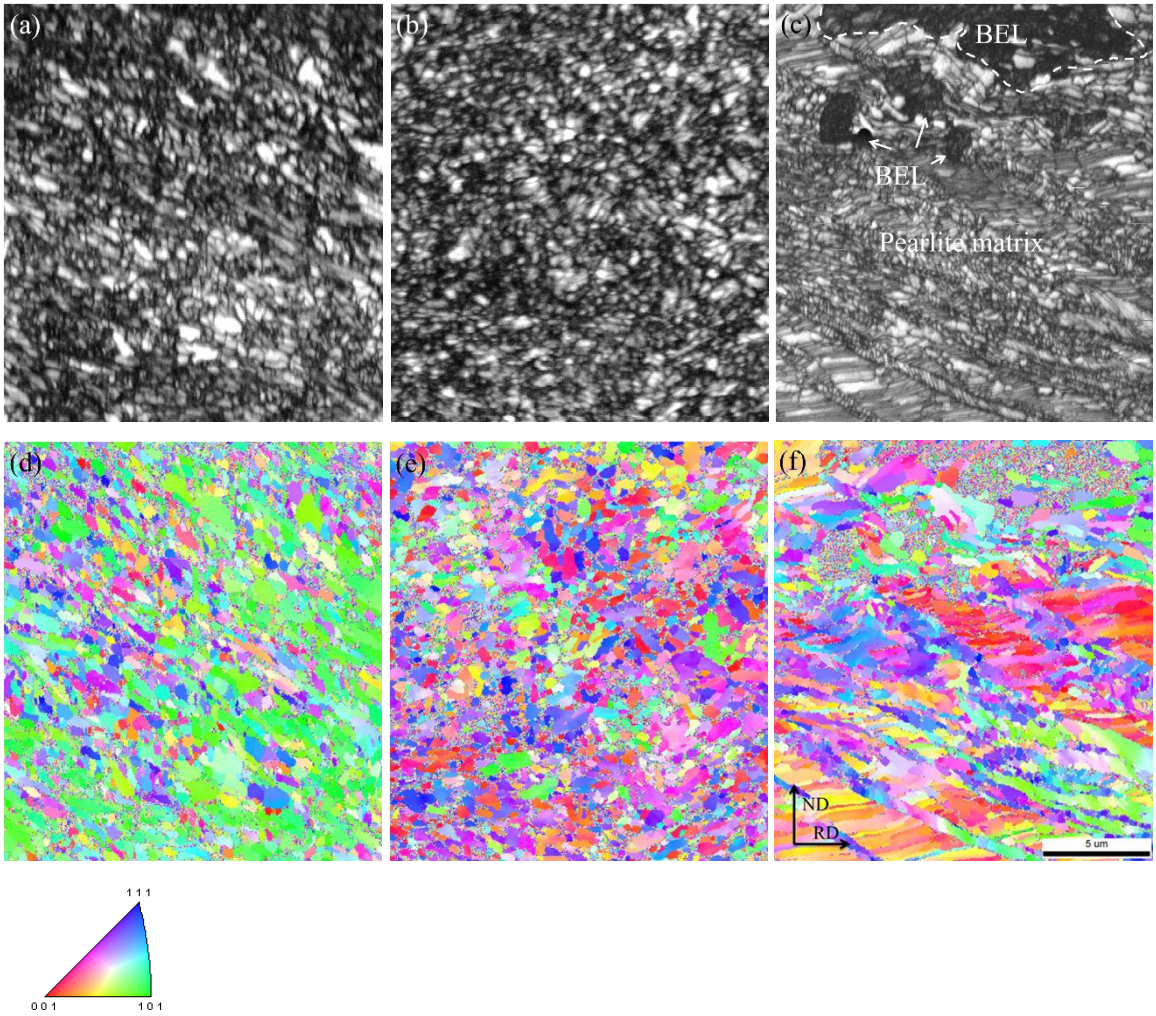

Fig. 7.5 The IQ maps of (a) surface area, (b) BEL zone 80 μm beneath the rail surface and is slightly above the BEL/pearlite boundary, (c) is the pearlite area underneath the BEL block and part of the BEL is included for the mapping. The corresponding IPF images relating to the ND directions of the three areas are shown in (d-f). The scale bar in (e) applies for all figures.

Two main grain morphology groups within the BEL are observed and can be summarized as follows, by relating to the external loading direction: *(i)* grains aligned toward the traffic direction (RD), approximately within the topmost 25 μm from rail surface, e.g. the IQ map in Fig. 7.5(a); and *(ii)* grains with random morphology representing the areas beneath the surface aligned zone and a representing example is shown by the IQ map of the subsurface BEL area in Fig. 7.5(b). The IQ map of pearlite immediately below the BEL is shown in Fig. 7.5(c), in which part of the BEL is included for the mapping. The boundary of the main BEL/matrix boundary is delineated by the white dotted line. The ferrite grains in the pearlite can be seen to be fragmented and aligned. Localized thin deformation bands are recognized in the pearlite zone. Some separated BELs, identified by lower IQ than pearlite and indicated by white arrows in Fig. 7.5(c), can be observed in the pearlite zone. This indicates the growing pattern of BEL towards the rail center during the service time.

The IPF of the corresponding zones in Figs. 7.5(a-c) are shown in Figs. 7.5(d-f) respectively, referring to the external ND direction. The grains of the topmost BEL, Fig. 7.5(d), show the likely preferred alignment of $\{1\ 0\ 1\}_{\alpha}$ along the ND direction of the rails. The grains of the unaligned subsurface area in BEL do not reveal preferred orientation, Fig. 7.5(e). The IPF of pearlite area immediately beneath the BEL is shown in Fig. 7.5(f). Only part of the included BEL was successfully indexed in this mapping and the unindexed areas are mapped as pixels with random crystal orientations. A significant difference in the orientation of the fragmented grains, rotated grains and the thin deformation bands can be seen. This indicates the deformation history in the characterized pearlite area.

Fig. 7.6(a) shows the differences of length fractions of high angle grain boundary (HAGB), defined with misorientations of 15 – 180°, and low angle grain boundary (LAGB), with misorientation between 5 - 15°, in areas along the rail depth. The data pixels with CI less than 0.1 were discarded for the quantification. The boundary position between BEL and matrix is indicated by the vertical dotted line in Fig. 7.6(a). The HAGB in BEL ranges from 48 % - 70 %, while the fraction of LAGB rarely exceeds 15 %. In general, both HAGB and LAGB fractions in BEL reduce through the rail depth. When reaching the pearlite area, LAGB length fraction increases from 6 % in the subsurface BEL zone to 27% in the pearlite while the HAGB fraction decreases from 48 % to 39 %.

Fig. 7.6(b) shows the grain equivalent diameter distributions in zones measured in Fig. 7.6(a). It can be seen that the grain size in the BEL scatters significantly and is not uniform and area with smallest average grain size is close to the BEL/pearlite boundary. The grain diameter in the pearlite immediately below the BEL can be seen to be comparable with the BEL. The average grain sizes in the zones within BEL are 314 ± 197 nm, 315 ± 238 nm, 401 ± 317 nm, 349 ± 229 nm, 307 ± 210 nm and an average size of 309 ± 297 nm is quantified in the measured pearlite zone.

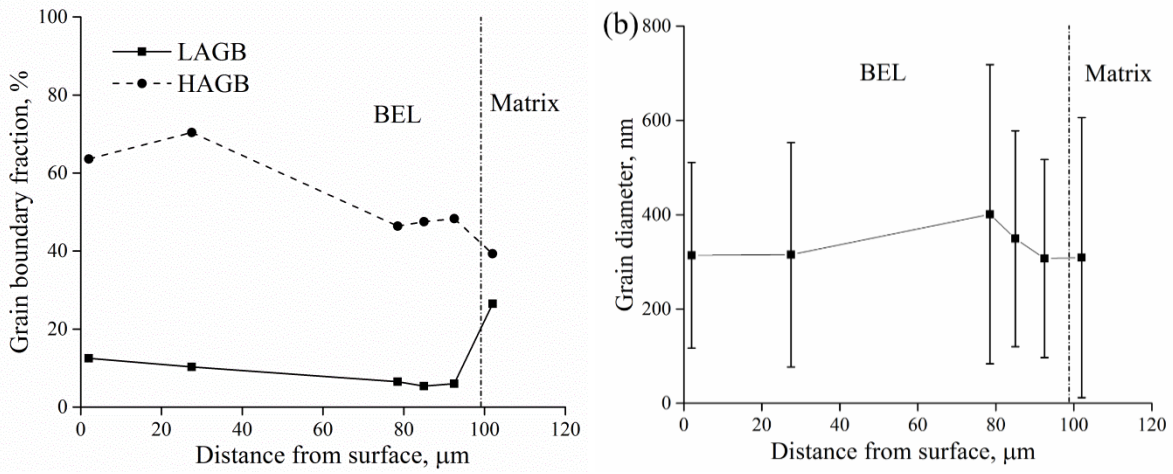

Fig. 7.6 (a) Distribution of grain boundary fraction along the rail depth; (b) the distribution of average grain diameter along the rail depth.

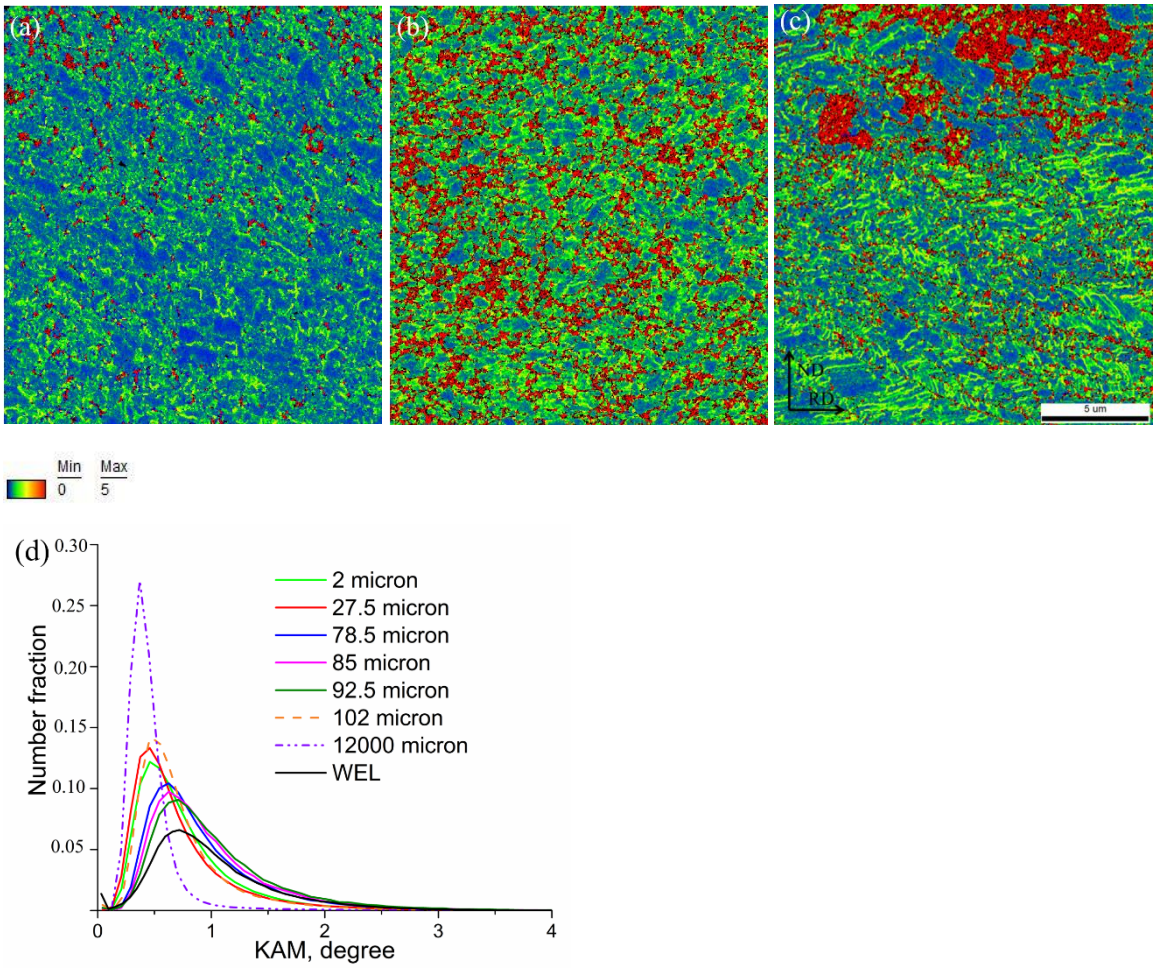

Fig. 7.7 The KAM maps of (a) surface BEL area, (b) BEL zone 80 μm beneath the rail surface and slightly above the BEL/pearlite boundary. (d) The KAM plot of areas in the BEL, deformed pearlite and the undeformed pearlite region. KAM plot of WEL in [6] is added for comparison.

Figs. 7.7(a-c) show the KAM maps of scanned areas in Figs. 7.5(a - c), using the 1st neighbor and cut-off angle of 5°. The clusters of red pixels represent 5° KAM and are due to the poorly indexed pixels which fail to be assigned to a proper neighboring grain by the used clean-up procedures. Dense green lines, representing misorientation 1 – 3° can be observed in all maps. The KAM distribution of areas along the rail depth is shown in Fig. 7.7(d) and the KAM measurement of WEL in [6], chapter 4, is included as a comparison. The KAM measurement from the undeformed zone, ~ 12 mm beneath the rail surface, is used as a reference for all measurements. The KAM plot of area at a depth ~ 102 μm corresponds to the deformed pearlite area closest to the BEL/pearlite boundary. It can be seen that the peaks of KAM distributions in the BEL and deformed pearlite shift to higher angle range, comparing with the reference undeformed pearlite. The KAM in the BEL increase along the rail depth and the KAM in the bottom of BEL, e.g. the zone at ~ 92.5 μm below the rail surface, is comparable with KAM of

WEL in [6]. The KAM profile of deformed pearlite immediately beneath the BEL is higher than the topmost BEL and is close to the ones for the area within the ~27 μm from rail surface.

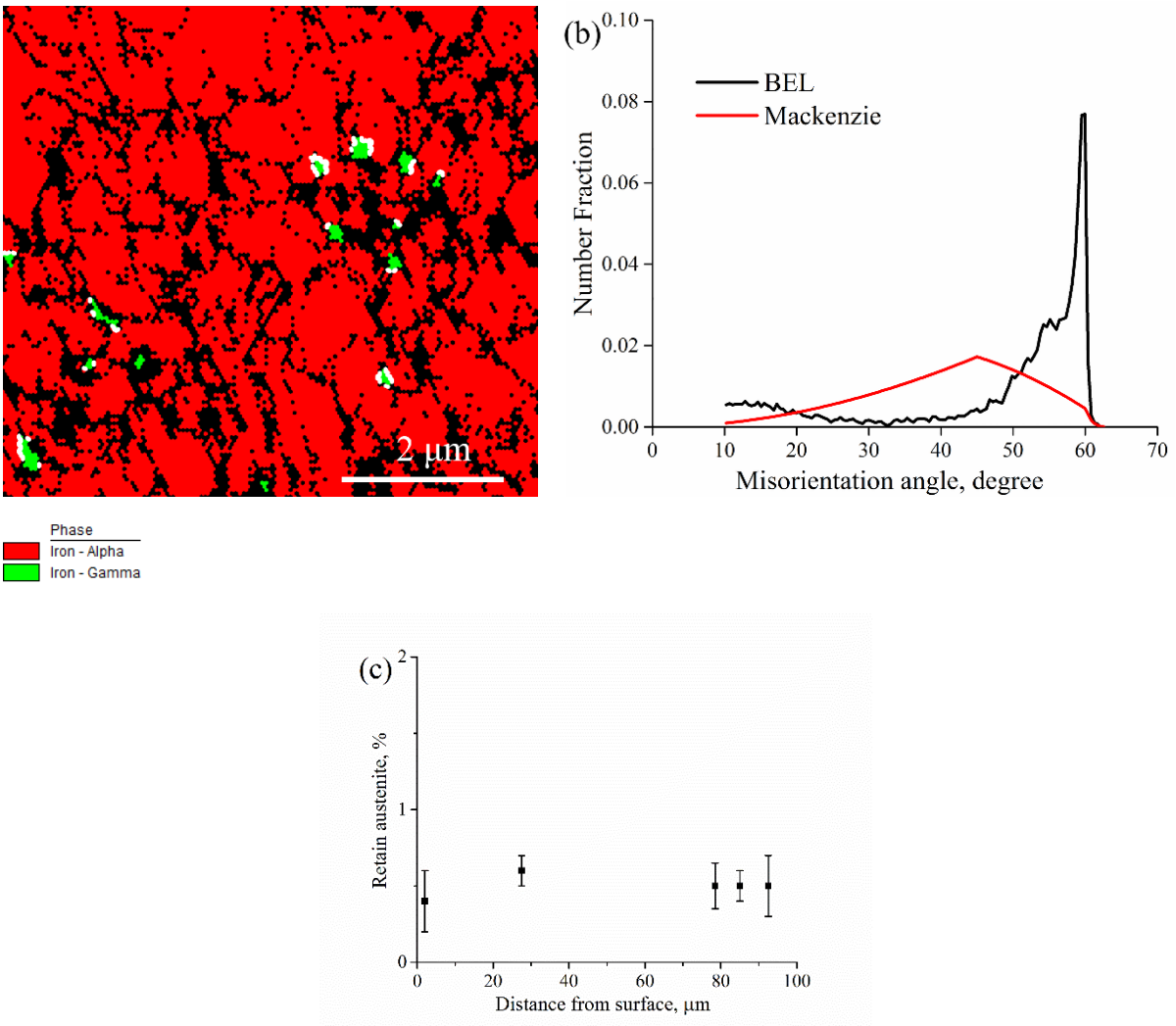

Fig. 7.8 (a) An example of the phase map revealing retained austenite in the BEL. The dark parts were due to the discarding of unreliable pixels with CI less than 0.1. The white lines decorate rotation boundaries of $90° < 112 >$, representing the K-S orientation relationship; (b) characteristics misorientation angle distribution in the BEL and the MacKenzie plot for random orientation distribution; (c) fraction of retained austenite in BEL along rail depth.

Retained austenite is frequently identified in the BEL and an example is shown in Fig. 7.8(a). The ferrite and austenite phases are decorated with green and red respectively in the phase map. The dark parts are due to the discarding of unreliable pixels with CI less than 0.1. The white lines in Fig. 7.8(a) delineate the boundaries satisfying axis/angle rotation of $90° < 112 >$, representing the K-S orientation relationship between martensite and austenite. The retained austenite is distributed heterogeneously and correlating the distribution to specific rail depth is impossible. Fig. 7.8(b) shows a representative misorientation angle distribution chart of ferrite grains in the BEL and the random MacKenzie distribution is included. The two maxima, at misorientation angles of 0 ° and ~60 °, assemble the

characteristic misorientation angles of martensite formed by normal heat treatment. Fig. 7.8(c) is the plot of retained austenite fraction in the BEL. The fraction of retained austenite in all measurements is very low, less than 1%, and there is no clear relation between austenite fraction and the rail depth of the characterized areas.

7.4. Discussion

7.4.1 Characteristics of BEL

Based on the current investigations, the presented BEL is found to have the following characteristics in general:

1) The BEL consists of heterogeneous sublayers with white and brown colors, Figs. 7.3(a) and (c), in contrast to the single uniform white layer in the WEL.

2) The hardness of the white sublayer in BEL is comparable to that of the WEL in [6–9], whereas the brown sublayer is significantly softer. The minimum measured hardness of the brown sublayer is 450 HV in Fig. 7.3(d) in this study, whereas the hardness of the WEL is rarely below 700 HV [7,8]. This indicates the possible different microstructure of the two types of layers.

3) The SEM observation of the brown sublayer reveals significant lamella-type morphology. Note that in Fig. 7.4(b) there is a continuation of the lamellae of BEL to the cementite lamellae in the bulk material immediately beneath. The continued lamellae may facilitate crack propagation from BEL into the bulk material, due to the low growth resistance of pearlite to cracks parallel with the lamellar direction [10].

4) The SEM observation of fibre-like and flattened morphology, Figs. 7.4(c) and (f), and the grain alignment in EBSD, Figs. 7.5(a) and (d), towards the traffic direction in the topmost surface region of the nearly single-layer BEL in Fig. 7.3(c), indicates a history of considerable plastic deformation of the rail material (see Fig. 7.4(c)).

5) Retained austenite is commonly identified through the whole brown sublayer in Fig. 7.3(c).

6) There is no significant difference in grain size in the BEL and the deformed pearlite area beneath, Fig. 7.6(b).

7) The KAM in the characterized BEL is higher than that of the undeformed pearlite area, Fig. 7.7(d). The KAM in the BEL increases toward the rail center.

7.4.2. Comparison and correlation BEL to WEL

To better understand the BEL, its microstructural features are compared to those of the WEL reported in the literature. A commonly pearlite-like microstructure is frequently revealed by SEM in the characterized brown sublayer in the BEL, e.g. Figs. 7.4(b) and (e). A more interesting observation can be the continuation of the cementite-like traces in the BEL, which cross the BEL/pearlite boundary in Fig. 7.4(b). The SEM work in [6,8] recognizes a similar pearlite-like feature at the bottom of WEL and the observed lamellar traces are identified as cementite by electron diffraction method in TEM. The interlamellar distance of the cementite in WEL measures 30 - 40 nm and is significantly finer than the

spacing of 80 - 120 nm in the undeformed matrix area [8]. Consequently, they propose that refined distance between lamella traces in the WEL is due to plastic deformation.

A similar pearlite-like morphology is identified at the bottom of the characterized WEL in chapter 4 of this thesis as well. The similar fragmented like cementite lamellae in ref[8] was recognized in TEM. However, refined cementite interlamellar distance is absent in this case as the measured interlamellar distance in the WEL is close to the one measured in the undeformed zone. Furthermore, the diffusive manganese compositional profile in the WEL, identified by the APT measurements, indicates that the investigated WEL forms predominantly via martensite phase transformation. The fragmented-like cementite was consequently considered to be due to partial dissolution of cementite as a result of extremely limited time for the alloying element to diffuse in the austenite during austenitization. Furthermore, an alike lamellar-like feature is expected in martensite formed via non-equilibrium heat treatments, due to the partial dissolution/transformation of cementite [6,11]. Consequently, extra evidence is necessary to clarify the microstructure in the BEL.

Based on the EBSD results, the studied BEL is unlikely to form predominantly via plastic deformation as the hypothesis proposed for the formation of WEL reported in [8]. Firstly, the ferrite grains refine as plastic strain increases in a pearlitic microstructure, e.g. after different high pressure torsion cycles [12]. Accordingly, the grains in the topmost BEL should be the finest, due to the expected maximum and mostly accumulated plastic strains in this region. In addition, up to 50 vol% of the grains in the WEL in ref[13] are characterized to be ~ 20 nm. Such grain size is beyond the spatial resolution of EBSD technique, typically 50 - 100 nm, and should consequently lead to failure in indexing of such fine grains. Moreover, most of the grains in the BEL are quantified to be more than 300 nm, which is much coarser than that in ref[13]. Secondly, the hypothesis of BEL formation via plastic deformation will fail to interpret the significant hardness decrease in the white sublayer and the immediately beneath brown sublayer in Figs. 7.3(a) and (b). A gradually reduced hardness is more reasonable for the hypothesis of plastic deformation [12]. The further increasing hardness in the brown sublayer along the rail depth in Figs. 7.3(b) and (d) is in contrast to the expected hardness changes with decreasing plastic strains in pearlite microstructure after deformation.

Instead, EBSD characterizations indicate that BEL forms dominantly via temperature induced martensite phase transformation. Firstly, the detection of retained austenite in the BEL in Figs. 7.8(a) and (c) is a strong indication of significant temperature increases up to austenitization temperature to transform the original pearlite to austenite [14,15]. Besides, the misorientation angle plot in Fig. 7.8(b) is a representative plot for martensite [16]. Secondly, the observation of isolated BEL in the pearlite region in Fig. 7.5(c) reveals the growing pattern of BEL during the loading history. The similar growth characteristic in WEL is observed by EBSD, which is proposed to form mainly via the martensite transformation mechanism in chapter 4. Such features can readily be interpreted by thermodynamic and kinetic theories [6]. As a result, BEL can be related to WEL in this case. Furthermore, the reduced KAM in the topmost BEL, Fig. 7.7(d), can also be explained due to recrystallization in this region.

In addition, the hardness distribution and the etching resistance to Nital chemical in the BEL, in Figs. 7.3(b) and (d), can be interpreted by the changes in martensite hardness after tempering at different temperatures. According to the prediction from finite element simulation [6], the maximum temperature, generated during frictional contact with the wheels, is expected to occur at the rail surface. The decreasing hardness in the brown sublayer approaching to the rail surface in Fig. 7.3 (c) can then be interpreted to be due to the softening by increasing extent of tempering [17]. Furthermore, the hardness difference in the white and brown sublayers in Fig. 7.3(a) can be explained by the softening in the martensite and the repeated martensite-austenite-martensite phase transformation cycles. The brown sublayer in Fig. 7.3(a) can correspond to the zone that is heated to temperatures below the lower critical temperature for austenite to occur, namely, the Ae_1 temperature. The martensite within this zone will not transform to austenite, while it will be tempered due to the high temperature. As a result, martensite closest to rail surface in Fig 7.3(c), while not transforming to austenite during heating, will be tempered to the greatest extent and consequently become the softest. The martensite in the white sublayer in Fig. 7.3(a) will repeatedly transform to austenite during heating and subsequently transform to martensite during cooling. The tempering reduces the etching resistance of martensite to Nital chemical, leading to the brownish appearance observed in this study.

It should, however, be pointed out that the above-mentioned hypothesis is based on the assumption that a single martensite WEL forms before the tempering occurs to form the observed white and brown sublayers in Fig. 7.3 (a) and (c). This can be possible since the unstable frictional heat is generated during the wheel/rail contact, which is a very complicated subject and is affected by different factors. Nevertheless, a reversed sequence for a BEL formed via martensite phase transformation is unlikely to occur, i.e. the brown sublayer forms prior and is the precursor for the white martensite sublayer. According to the quasi-binary phase diagram in Fig. 7.9, reproduced from chapter 5, a mixture of pearlite and martensite (transformed from austenite) is expected at temperatures below full austenitization. An increasing fraction of martensite will form at higher temperatures and will improve the hardness, if the rail steels is heated to the temperature range with mixed microstructures. Accordingly, this should lead to the observation of increasing hardness in the BEL when approaching the rail surface. However, an opposite hardness distribution is observed in Figs. 7.3(b) and (d) in this work

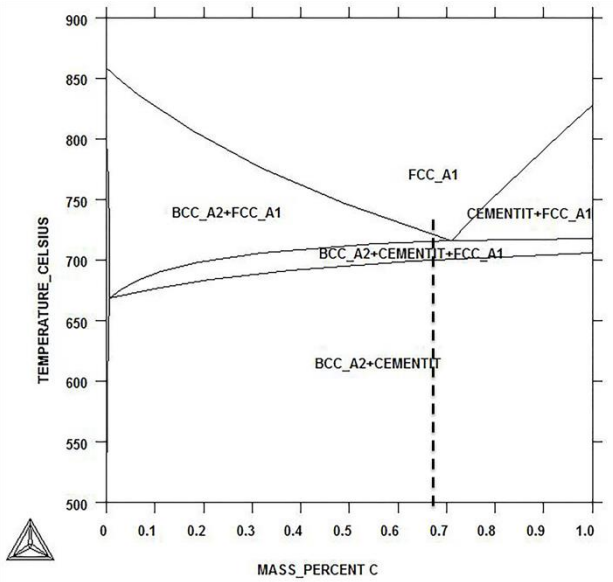

Fig. 7.9 The quasi-binary Fe – C phase diagram, reproduced from chapter 5 from this thesis.

Meanwhile, evidence of plastic deformation history in the studies rail specimen can be identified. This is indicated by: *(i)* the fiber-like morphology in the BEL, Figs. 7.4(c) and (f), and the observed materials flow in Figs. 7.3(a) and (c); *(ii)* the alignment of grain morphology towards the ND direction in the topmost BEL, Fig. 7.5(a), *(iii)* the higher KAM in the BEL and the pearlite immediately underneath the BEL, compared with that of the undeformed matrix pearlite, Fig. 7.7(d); *(iv)* the grain fragmentation and the deformation bands in pearlite beneath the BEL/pearlite boundary, Fig. 7.5(c). As a result, the studied BEL forms via combined contribution of plastic deformation and thermally induced phase transformation.

7.5. Conclusions

This chapter characterizes a different type of WEL, the BEL, in a rail sample showing RCF damage. The BEL is characterized by optical microscopy, microhardness, scanning electron microscopy and EBSD. The findings are compared with WEL reported in the literature. The following conclusion can be drawn:

(1) BEL consists of white and brown sublayers with distinctly different mechanical properties.
(2) BEL forms via combined martensite phase transformation and plastic deformation.
(3) The white sublayer is proposed as martensite and the brown sublayer is martensite that is tempered below the critical austenite transformation temperature.

References:

[1] S. Li, J. Wu, R.H. Petrov, Z. Li, R. Dollevoet, J. Sietsma, “Brown etching layer”: A possible new insight into the crack initiation of rolling contact fatigue in rail steels?, Eng. Fail. Anal. 66 (2016) 8–18.

[2] P. Clayton, M.B.P. Allery, Metallurgical Aspects of Surface Damage Problems in Rails, Can. Metall. Q. 21 (1982) 31–46.

[3] R.I. Carroll, J.H. Beynon, Rolling contact fatigue of white etching layer: Part 1: Crack morphology, Wear. 262 (2007) 1253–1266.

[4] W. Lojkowski Djahanbakhsh, M., Bürkle, G., Gierlotka, S., Zielinski, W., Fecht, H. J., Nanostructure formation on the surface of railway tracks, Mater. Sci. Eng. A. 303 (2001) 197–208.

[5] M. Steenbergen, R. Dollevoet, On the mechanism of squat formation on train rails – Part I: Origination, Int. J. Fatigue. 47 (2013) 361–372.

[6] J. Wu, R.H. Petrov, M. Naeimi, Z. Li, R. Dollevoet, J. Sietsma, Laboratory simulation of martensite formation of white etching layer in rail steel, Int. J. Fatigue. 91 (2016) 11–20.

[7] E. Wild Wang, L., Hasse, B., Wroblewski, T. , Goerigk, G., Pyzalla, A., Microstructure alterations at the surface of a heavily corrugated rail with strong ripple formation, Wear. 254 (2003) 876–883.

[8] H.W. Zhang, S. Ohsaki, S. Mitao, M. Ohnuma, K. Hono, Microstructural investigation of white etching layer on pearlite steel rail, Mater. Sci. Eng. A. 421 (2006) 191–199.

[9] J. Seo, S. Kwon, H. Jun, D. Lee, Numerical stress analysis and rolling contact fatigue of White Etching Layer on rail steel, Int. J. Fatigue. 33 (2011) 203–211.

[10] F. Wetscher, R. Stock, R. Pippan, Changes in the mechanical properties of a pearlitic steel due to large shear deformation, Mater. Sci. Eng. A. 445–446 (2007) 237–243.

[11] L.E. Samuels, Light Microscopy of Carbon Steels, ASM International, 1999.

[12] Y. Ivanisenko, W. Lojkowski, R.Z. Valiev, H.J. Fecht, The mechanism of formation of nanostructure and dissolution of cementite in a pearlitic steel during high pressure torsion, Acta Mater. 51 (2003) 5555–5570.

[13] W. Lojkowski, Y. Millman, S.I. Chugunova, I. V Goncharova, M. Djahanbakhsh, G. Bürkle, et al., The mechanical properties of the nanocrystalline layer on the surface of railway tracks, Mater. Sci. Eng. A. 303 (2001) 209–215.

[14] W. Österle Rooch, H., Pyzalla, A., Wang, L., Investigation of white etching layers on rails by optical microscopy, electron microscopy, X-ray and synchrotron X-ray diffraction, Mater. Sci. Eng. A. 303 (2001) 150–157.

[15] L. Wang Pyzalla, A., Stadlbauer, W., Werner, E. A., Microstructure features on rolling surfaces of railway rails subjected to heavy loading, Mater. Sci. Eng. A. 359 (2003) 31–43.

[16] L. Ryde, Application of EBSD to analysis of microstructures in commercial steels, Mater. Sci. Technol. 22 (2006) 1297–1306.

[17] B.L. Bramfitt, B.S. Corporation, Structure / Property Relationships in Irons and Steels, Met. Handb. Desk Ed. Second Ed. (1998) 153–173.

Chapter 8 General conclusions and recommendations

8.1. Conclusions

The research presented in this dissertation focuses on the microstructural processes taking place during the wheel/rail contact in pearlitic railway steels. The most striking microstructural change is the formation of the White and Brown Etching Layers (WEL and BEL) at and just below the surface. The interpretation and analysis of the microstructural processes enable a semi-quantitative estimate of the mechanical and thermal conditions in the rail, which however was not the central issue of interest in this dissertation. The most significant findings from this research are summarized in this chapter:

1) The current dissertation convincingly shows that the thermally-induced pearlite to austenite transformation occurs at the rail surface during the wheel/rail interaction. The austenite at the rail surface transforms during cooling to twinned martensite with very high carbon content and fine microstructure. This thin surface layer of high carbon martensite appears white after etching with 2 to 5% nitric acid in ethanol and is known in the literature as WEL.
2) This finding is supported by the characterizations on the WEL and the BEL in the R260 Mn grade rail steel, which is often found underneath the WEL. It is generally accepted that a small fraction of austenite is retained during the martensitic transformation and can be identified in the microstructure at room temperature, e.g. [1]. The common identification of retained austenite in the WEL by XRD, EBSD and TKD is strong evidence of temperature rise above the austenitization temperature during the wheel loading, which leads to the transformation from the initial pearlite to austenite. It is very difficult to monitor the exact loading conditions of the rails and it is almost impossible to preform accurate temperature measurements on the rail surface at the moment of rail/wheel contact. The

majority of the data for temperature changes in rails are obtained via modeling approach. In this work not only the observation of retained austenite is evidence for the occurrence of very high temperatures, but also the manganese diffusion in the surface WEL. Evidence for manganese diffusion was derived by comparing with the manganese profile from the matrix pearlite. This is evidence for the high-temperature increase in the rail surface since the manganese diffusion is very sluggish at low temperatures. Accordingly, the WEL is identified to consist of martensite and retained austenite.

3) The structures in the WEL in rails can be simulated by ultrafast heating and cooling experiments under laboratory conditions. The martensite morphology in the WEL in rails was successfully reproduced by applying heating rates of 20 °C/s and 200 °C/s to different temperatures in the austenitization range, immediately followed by fast cooling. The retained austenite in the WEL, as found in rails, is also identified in the laboratory simulated WEL. This experiment showed that the WEL in rails can form by martensitic transformation, induced by attaining a high temperature, followed by fast cooling.
4) Phase field modeling (PFM) is used to study the characteristics of the pearlite to austenite transformation during continuous heating. Although the applied heating rate of 2000 °C/s in the PFM is not directly applicable to the actual condition at rail surface during the wheel passage, e.g. more than 10^5 °C/s, the PFM results reveal a clear tendency of shift towards the interface-controlled mechanism during the austenite growth as heating rate increases.
5) The study of the brown etching layer (BEL) indicates that the BEL forms most probably due to tempering of the martensite. Similarly to WEL, the identification of retained austenite through the whole BEL thickness is considered as strong evidence that the temperature increases above the austenitization temperature at the rail surface during the wheel/rail contact. The degradation of etching resistance to Nital and the reduced hardness in the brown sub-layer in the BEL can be interpreted to be due to the tempering of the martensite. Accordingly, the BEL is proposed to consist of tempered martensite.

8.2. Recommendations for future work

Besides the insight into the WEL and BEL formation presented in this dissertation, the following aspects are recommended to be further investigated for a better understanding of the WEL and BEL and their roles in the Rolling Contact Fatigue damage development:

1) Characterization of the BEL to further explore its formation mechanism. The formation mechanism of BEL in Chapter 7 in this dissertation is a first interpretation and is proposed based on the different etching response to Nital, the hardness profile along the rail depth and the EBSD scans through the BEL thickness. Characterization with more advanced techniques, like TEM and APT that allow revealing the fine microstructure of BEL and type of carbides formed, will lead to more profound

insight. Identification of carbide types and the fine structure of martensite, together with the carbon content of austenite, can be used as evidence for the tempering processes in the WEL that change its microstructure, properties and etching response towards BEL.

2) Quantitative study of the fracture and fatigue performance of the WEL and BEL. WEL is widely proposed to be an important cause to the initiation of rolling contact fatigue (RCF) cracks and its presence can cause RCF damage initiation. Similarly, the BEL can be another important cause of RCF damage. A more quantitative study on the fracture characteristics and fatigue properties of the WEL and the BEL and the comparisons with the martensite formed during fast heating and quenching heat treatments will be beneficial to confirm the role of WEL and BEL in the RCF crack formation. The fracture properties can be further used as more realistic input parameters for RCF formation in finite element simulations and micromechanical modeling, which will provide quantitative insight into the role in the RCF development in relation with the WEL and BEL.
3) Experimental validation of the compositional characteristics in the martensite (the austenite during high temperature), formed under the realistic conditions simulated in Phase Field Modeling. The chemical compositions in the martensite can be considered to be identical to the austenite before the transformation and can be quantitatively studied by Atom Probe Tomography. Such study can experimentally validate the conclusion that high heating rates shift towards the interface-controlled mechanism during austenite growth, predicted from the phase field modeling.
4) Study of the possible formation of WEL and BEL in bainitic rail steels and the role in the RCF evolution by in-field tests on the Dutch rail track and laboratory simulations with the recently developed railway test rig at the CiTG faculty of the Delft University of Technology. The bainitic rail steels have been shown to have advantages on the RCF performance over the pearlitic rail steels, e.g. the field tests [2] and from laboratory tests [3,4]. Whether WEL and BEL will form in the bainitic steel under the contact conditions on the Dutch rail track remains unclear. The test rig allows a precise control of the loading conditions to form the WEL and BEL in the bainitic steel.

References:

[1] Krauss G. Martensite in steel: strength and structure. Mater Sci Eng A 1999;273–275:40–57.

[2] Sawley K, Kristan J. Development of bainitic rail steels with potential resistance to rolling contact fatigue. Fatigue Fract Eng Mater Struct 2003;26:1019–29.

[3] Aglan HA, Liu ZY, Hassan MF, Fateh M. Mechanical and fracture behavior of bainitic rail steel. J Mater Process Technol 2004;151:268–74.

[4] Stock R, Pippan R. Rail grade dependent damage behaviour - Characteristics and damage formation hypothesis. Wear 2014;314:44–50.

Summary

The microstructural aspects of rolling contact fatigue in rails were studied. The rail track is a critical component of the railway system and its long-term performance contributes crucially to the sustainable development of the railway system. The increasing demands of trains with a higher speed/capacity impose more severe load conditions on the steel rail tracks. Steels with improved performance are needed to meet such demands because the current rail steels are reaching their limit. Moreover, the understanding of the root cause of damage in rails is still insufficient. This hinders the development of new rail steels that perform better.

The dominant damage in rails is rolling contact fatigue (RCF), the effects of which can cost the rail maintenance companies millions of euros a year. In order to reduce the rail track maintenance cycles, progress in numerical modeling to predict the RCF crack evolutions is continuously made. Simultaneously, numerous microstructure studies are being done on field loaded rail steels, to explore the cause of RCF by analyzing the rail steels' response to the loading from the passing wheels. The knowledge of the rail microstructure is essential in these cases, especially due to fact that the RCF crack initiation is mainly microstructurally related.

Premature RCF crack initiation in the pearlite rail steels occurs due to the formation of a peculiar surface (micro) structure change, classically called white etching layer (WEL). WEL is typically 2 – 3 times harder than the pearlite matrix. Metallographic studies in both field-loaded and laboratory simulated loadings of rail steels reveal frequently brittle fractures across the WEL, besides crack formations in the pearlite adjacent to the WEL. The numerical simulations identify a more extensive strain accumulation in pearlite close to the WEL, compared to that in pearlite without WEL.

The microstructure in the WEL is complex and extremely fine, making the characterization of WEL challenging. High-resolution techniques such as X-Ray Diffraction (XRD), Transmission Electron Microscopy (TEM) and Atom Probe Tomography (APT) have been successfully applied to establish the grain size, phases, and compositional characteristics of WEL respectively. However, controversy regarding the origin of the WEL remains, most probably because the WELs studied in the literature were generated in rails under various and not well-defined loading conditions. In summary, WELs are

generally proposed to be caused via either martensite phase transformation owing to a significant temperature increase during wheel passage(s) or via significant grain refinement due to severe plastic deformation.

In order to gain a comprehensive insight into the microstructure in the WEL, techniques at different resolution scales (from micrometer to nanometer), are used for characterizations in ***Chapter 4***. The WEL was firstly investigated by optical microscopy and microhardness measurements to reveal the morphology and hardness of WEL and the pearlite matrix. XRD is used to study the phase components in the WEL, by scanning the surface areas containing WEL. Secondary electron images are taken from a scanning electron microscope (SEM) to assess the WEL at an improved resolution level, compared with that in optical microscopy. EBSD measurements in SEM provide information about grain structure, phase component in the WEL, which are compared with those in the pearlite matrix immediately beneath the WEL. Kernel Average Misorientation (KAM) analysis was used to quantify the deformation level. In addition, TEM is used to study the microstructure in the WEL with a resolution of sub-nanometer and APT is used to determine the compositions of WEL at the same dimensional level. The results obtained are consistent with each other: *(i)* Both XRD and EBSD show the presence of retained austenite, indicating the martensite nature of WEL; *(ii)* TEM identifies a representative nano-twinning substructure of martensite and the presence of untransformed cementite; *(iii)* the APT results reveal a significant manganese redistribution between zones of previous cementite and ferrite, providing direct evidence of a temperature increase. The experimental findings are compared with those of the literature and they are in good agreement. The WEL in ***Chapter 4*** has the same white color as in the one reported in the literature, taken from optical microscopy and after being etched with the same chemical etchant. In addition, grain size quantification from EBSD measurements shows that the grains within the WEL can go up to micrometer size. This is much larger than that reported in the nanocrystalline ferrite WEL. Furthermore, the KAM comparison shows the absence of deformation in the pearlite matrix immediately beneath the WEL. Based on the microstructural investigations at different scales, it is suggested that the studied WEL has been formed via martensite phase transformation.

A laboratory simulation of WEL formation during continuous heating is described in ***Chapter 5***. This simulation provides supportive evidence for the conclusions drawn in ***Chapter 4***. Although it is impossible to fully reproduce real conditions for WEL formation, e.g. the extremely high heating rate, the well-controlled laboratory conditions will enable a (semi)quantitative insight into the WEL formation process and the outcome can further be used for verifying the theoretical simulations. In ***Chapter 5***, WEL formation during continuous heating was simulated in a thermo-mechanical simulator, under heating rates of 20 and 200 °C /s to different temperatures above the austenitization temperature. Simultaneous deformation and heating-quenching tests were done to assess the contribution of local plastic strain in the martensite formation. The microstructures after the tests were characterized by optical microscopy, microhardness, and EBSD. It is found that, with the applied heating rates, the generated martensite has a similar hardness and morphology as WEL observed in ***Chapter 4*** under real

exploitation conditions. EBSD measurements on both laboratory simulated and rail WEL identify similar grain sizes. Plastic deformation is shown to enhance the formation of martensite, compared with specimens tested under identical conditions without strain. The experimental findings can be interpreted by thermodynamic and kinetic calculations. Finally, FEM simulation of temperature changes during wheel/rail contact also confirms the possibility of a temperature increase in rails above the austenitization temperature.

In ***Chapter 6***, WEL formation due to pearlite to austenite and the subsequent martensite phase transformation is modeled using the phase field modeling approach, in order to obtain insight into the specifics of WEL formation. For the modeling, a 2D microstructure model was first built to represent the pearlite microstructure in 3D, from the consideration of the plate-like morphology of ferrite and cementite and the assumption that the carbon diffusivity is isotropic. The driving force of the ferrite and cementite to austenite transformations is obtained using the linearized iron-carbon phase diagram, whereby the transformation kinetics are taken into account by incorporating the phase interface mobility and diffusivity of carbon. Due to fact that WEL formation occurs most probably after many wheel passages, the martensite, which transforms from the austenite from the previous wheel passage, is included as the initial microstructure for the next wheel pass. Martensite is, however, a non-equilibrium phase and there is scarce quantitative information regarding the martensite to austenite transformation. Following the literature, carbon-supersaturated ferrite is used to represent the martensite. The simulation results show that transformation from ferrite to austenite is faster than that of the cementite to austenite transformation. The increased heating rate caused the carbon concentration in austenite to deviate more from the equilibrium concentration. Accordingly, there is more heterogeneity in the mechanical properties in the WEL, which inherit the carbon concentration of the austenite.

In ***Chapter 7***, a new type of surface damaged layer, named as BEL due to the brownish appearance, is discussed. BEL differs from WEL not only in its appearance in optical microscopy but also in its hardness. Measurements of crack lengths show that the RCF cracks associated to BEL are longer than those formed by the WEL. Characterization with hardness, optical microscopy, and EBSD shows a layered structure in the BEL. The brownish area within the BEL is significantly softer than the classical WEL, while its white colored area has a hardness similar to the WEL. EBSD measurements identify retained austenite in the BEL and grain refinement in the pearlite immediately beneath the BEL. The deformation features, in the BEL and the pearlite underneath are quantified by the KAM method from EBSD scans, by comparing with the measurement from deformation-free pearlite areas. As a result, BEL is considered to form via both plastic deformation and phase transformation. The white sublayer is proposed as martensite and the brown sublayer is martensite that was tempered below the critical austenite transformation temperature.

Samenvatting

De microstructurele aspecten van rollende contactmoeheid in rails worden in dit proefschrift beschreven De spoorstaven vormen een cruciaal onderdeel van het spoorwegsysteem en de lange duur prestaties hiervan dragen in hoge mate bij aan de duurzame ontwikkeling van het systeem. Treinen met steeds hogere snelheid / capaciteit leggen steeds zwaardere belastingscondities op aan de stalen railsporen. Staalsoorten met betere prestaties in spoorbanen zijn nodig om aan de toenemende eisen te voldoen, omdat de huidige railstalen hun limiet bereiken. Bovendien is het inzicht in de grondoorzaak van schade aan rails nog onvoldoende. Dit belemmert de ontwikkeling van nieuwe spoorstaafstalen met betere prestaties.

De dominante schade in rails is rollende contactmoeheid (RCF), waarvan de effecten de spoorwegonderhoudsbedrijven miljoenen euro's per jaar kunnen kosten. Om de onderhoudcycli van het spoor te verkorten, wordt continu vooruitgang geboekt in de numerieke modellering om de RCF-scheurontwikkeling te voorspellen. Gelijktijdig worden parallel daaraan tal van microstructuurstudies uitgevoerd op het belaste railstaal, om de oorzaak van RCF te onderzoeken door de respons van de spoorstalen op de passerende wielen te analyseren. De kennis van de railmicrostructuur is hierbij essentieel, vooral vanwege het feit dat de RCF-scheur initiatie hoofdzakelijk microstructureel gerelateerd is.

Voortijdige RCF-scheurinitiatie in het perliet-railstaal vindt plaats als gevolg van een bijzondere verandering van de (micro-) oppervlaktestructuur, klassiek aangeduid als witte etslaag (WEL). WEL is meestal 2 - 3 keer harder dan de perlietmatrix. Metallografische studies van railstaal, naar zowel in de praktijk belaste als laboratorium belaste railstaal onthullen vaak brosse breuken over de WEL, naast barstvorming in het perliet in de buurt van de WEL. De numerieke simulaties tonen een meer uitgebreide spanningsaccumulatie aan in perliet dichtbij de WEL, dan in het perliet zonder WEL.

De microstructuur in de WEL is complex en buitengewoon kleinschalig , waardoor de karakterisering van WEL uitdagend is. Hoge-resolutie technieken zoals X-Ray Diffraction (XRD), Transmission Electron Microscopy (TEM) en Atom Probe Tomography (APT) zijn met succes toegepast om respectievelijk de korrelgrootte, fasen en compositiekenmerken van WEL te karakteriseren.

Controversen met betrekking tot de oorsprong van de WEL bestaan echter nog steeds. Dit is hoogstwaarschijnlijk te wijten aan het feit dat de WEL's die in de literatuur worden beschreven , werden gegenereerd in rails onder verschillende en niet goed gedefinieerde bedrijfsomstandigheden . Samenvattend, WEL's worden over het algemeen gesteld te worden veroorzaakt via martensite fase transformatie als gevolg van een significante temperatuurstijging tijdens de wielpassage (s) of via aanzienlijke korrelverfijning als gevolg van sterke plastische vervorming.

Om een uitgebreid inzicht te krijgen in de microstructuren in de WEL, worden in Hoofdstuk 4technieken op verschillende resolutieschalen (van micrometer tot nanometer) gebruikt voor de karakterisering. De WEL werd eerst onderzocht door optische microscopie en microhardheidsmeting om de morfologie en hardheid van WEL en de perliet -matrix vast te stellen. XRD werd gebruikt om de fasecomponenten in de WEL te bestuderen door de oppervlakten te scannen die WEL bevatten. Secundaire elektronenbeelden werden genomen van een scanning-elektronenmicroscoop (SEM) om de WEL te analyseren met een verbeterd resolutieniveau, vergeleken met dat in optische microscopie. EBSD-metingen in SEM verschaffen informatie over de korrelstructuur, de fasecomponenten in de WEL. Deze worden vergeleken met die in de perlietmatrix onmiddellijk onder de WEL. Kernel Average Misorientation (KAM) -analyse werd gebruikt om het deformatieniveau te kwantificeren. Bovendien werd t TEM gebruikt om de microstructuur in de WEL vast te stellen met een resolutie van sub-nanometers en wordt APT gebruikt om de samenstellingen van WEL in hetzelfde dimensie –bereik waar te nemen . De verkregen resultaten zijn consistent met elkaar: *(i)* Zowel XRD als EBSD tonen de aanwezigheid van vastgehouden austeniet aan, wat de martensietaard van WEL aangeeft; *(ii)* TEM laat een representatieve nano-twinning substructuur van martensiet en de aanwezigheid van niet-getransformeerd cementiet zien; *(iii)* de APT-resultaten onthullen een significante herverdeling van mangaan tussen zones van eerder aanwezig cementiet en ferriet, wat een direct bewijs van temperatuurverhoging oplevert . De experimentele bevindingen worden vergeleken met die uit de literatuur en zijn in goede overeenstemming. De WEL in Hoofdstuk 4 heeft dezelfde witte kleur als die in de literatuur wordt vermeld.Zij werd vastgesteld met optische microscopie en werd geëtst met hetzelfde chemische etsmiddel. Bovendien laat kwantificering van de korrelgrootte van EBSD-metingen zien dat de korrels binnen de WEL tot micrometers groot kunnen zijn en dus veel groter zijn dan die gerapporteerd in het nanokristallijne ferriet WEL. Verder toont de KAM-vergelijking de afwezigheid aan van vervorming in de perlietmatrix direct onder de WEL. Op basis van de microstructurele karakterisering op verschillende schalen, wordt gesuggereerd dat de bestudeerde WEL-vormen worden gevormd via martensietfase-transformatie.

Een laboratoriumsimulatie van WEL-vorming tijdens continue verwarming wordt in Hoofdstuk 5 beschreven . Deze simulatie biedt aanvullend bewijs voor de conclusies in Hoofdstuk 4. Desondanks is het onmogelijk om reële omstandigheden voor WEL-vorming na te bootsen, b.v. de extreem hoge verwarmingssnelheid. De goed gecontroleerde laboratoriumomstandigheden geven echter wel een (semi) kwantitatief inzicht in het WEL-formatieproces . De uitkomst kan verder worden gebruikt voor

het verifiëren van de theoretische simulaties. In Hoofdstuk 5 wordt WEL-vorming tijdens continue verwarming gesimuleerd in een thermomechanische simulator, onder opwarmsnelheden van 20 en 200 °C /s tot verschillende temperaturen boven de austenitiseringstemperatuur. Gelijktijdige vervormings- en opwarm-afkoel proeven werden uitgevoerd om de bijdrage van plaatselijke plastische deformatie in de martensietformatie te bestuderen. De microstructuren na de tests werden onderzocht met optische microscopie, microhardheid en EBSD. Het is gebleken dat, met de toegepaste verwarmingssnelheid, het gegenereerde martensiet een vergelijkbare hardheid en morfologie heeft als WEL onder reële exploitatie-omstandigheden zoals waargenomen in Hoofdstuk 4. EBSD-metingen op zowel laboratorium-gesimuleerde als rail-WEL laten vergelijkbare korrelgroottes zien. Er wordt aangetoond dat plastische vervorming de vorming van martensiet versterkt , vergeleken met monsters die zonder spanning onder dezelfde omstandigheden zijn getest. De experimentele bevindingen konden worden geïnterpreteerd door thermodynamische en kinetische berekeningen. Tenslotte wijst FEM-simulatie van de temperatuurveranderingen tijdens contact tussen wiel en rail eveneens op de mogelijkheid van temperatuurverhogingen in rails boven de austenitiseringstemperatuur.

In Hoofdstuk 6 wordt WEL-vorming als gevolg van perliet tot austeniet en de daaropvolgende martensietfase-transformatie gemodelleerd met behulp van een faseveld-modelleringsaanpak, om zo inzicht te krijgen in de kenmerken van WEL-vorming. Voor de modellering werd eerst een 2D microstructuurmodel gebouwd om de perlite microstructuur in 3D weer te geven, uitgaande van de plaatachtige morfologie van ferriet en cementiet en de aanname dat de koolstof diffusie isotroop is. De drijvende kracht van de ferriet- en cementiet-tot-austeniettransformaties werd verkregen door gebruik te maken van het gelineariseerde ijzer-koolstof fasediagram waarbij de transformatiekinetiek in rekening wordt gebracht door integratie van fase-grenslaagmobiliteit en de diffusiviteit van koolstof. Vanwege het feit dat WEL-vorming hoogstwaarschijnlijk na veel wielpassages optreedt , wordt het martensiet, dat transformeert van het austeniet van de vorige wielpassage, opgenomen als de initiële microstructuur voor de daaropvolgende wielpassage. Martensiet is echter een niet-evenwichtsfase en er is nauwelijks kwantitatieve informatie over de martensiet-naar-austeniettransformatie. Volgens de literatuur wordt koolstof-oververzadigd ferriet gebruikt om het martensiet te representeren . De resultaten van de simulaties laten zien dat transformatie van ferriet naar austeniet sneller gaat dan de omzetting van cementiet naar austeniet. De verhoogde verwarmingssnelheid zorgt ervoor dat de koolstofconcentratie in austeniet meer afwijkt van de evenwichtsconcentratie. Dienovereenkomstig is er meer heterogeniteit in de mechanische eigenschappen in de WEL, die de koolstofconcentratie van het austeniet aannemen .

In Hoofdstuk 7 wordt een nieuw type oppervlakbeschadigde laag, BEL genoemd vanwege het bruine uiterlijk, beschreven . BEL verschilt van WEL, niet alleen qua uiterlijk onder optische microscopie maar ook qua hardheid. Metingen van scheurlengten tonen aan dat de RCF-scheuringen geassocieerd met BEL langer zijn dan die gevormd door de WEL. Karakterisering met hardheid, optische microscopie en EBSD toont een gelaagde structuur aan binnen de BEL. Het bruinachtige gebied binnen de BEL is

aanzienlijk zachter dan de klassieke WEL, terwijl het witgekleurde gebied een vergelijkbare hardheid heeft als de WEL. EBSD-metingen identificeren achtergebleven austeniet in de BEL en korrelverfijning in het perliet onmiddellijk onder de BEL. De vervormingseigenschappen in de BEL en het perliet daaronder werden gekwantificeerd door de KAM-methode van EBSD-scans, door deze te vergelijken met de meting van vervormingsvrije gebieden. Als gevolg hiervan wordt BEL beschouwd zich te vormen via zowel plastische vervorming als fasetransformatie. De witte sublaag wordt voorgesteld als martensiet en de bruine sublaag is martensiet dat werd getemperd onder de kritische austeniettransformatietemperatuur.

Curriculum vitae

Jun WU

Education/Research background

PostDoc researcher in Delft University of Technology 2017.06-

- Bosch project: Microstructure formation in high strength steels used in continuously variable transmission pushbelts
- The project aims to provide insight into the better control of precipitate formation in the maraging steels and the simultaneous nitriding process, in order to optimize their mechanical performance.
- Supervisor: Prof. Jilt Sietsma, Prof. Roumen Petrov

Ph.D. candidate in Delft University of Technology 2013.04-2017.03

- Thesis title: 'Microstructure damage in rail steels due to rolling contact fatigue'
- Supervisor: Prof. Jilt Sietsma, Prof. Roumen Petrov

Researcher in Vienna University of Technology, Austria 2010.12-2013.01

- Characterization and modeling of precipitation sequence in heat-treated aluminum alloys

M.Sc. in Materials Science and Engineering, Shanghai University, China 2007.09-2010.06

- Dissertation: 'Microstructure Control and Chemical Composition Optimization of Prehardened Plastic Mold Steel'

List of publications

A. International Peer-Reviewed journals

1) **J Wu**, S Li, R H Petrov, Z Li, R Dollevoet, J Sietsma, Electron backscatter diffraction characterization of surface structure change layers in rails. *Under review of supervisor*.
2) **J Wu,** R H Petrov, Jilt Sietsma, Phase field modelling of white etching layer formation in rails via martensite phase transformation, *under review of supervisor*.
3) **J Wu**, R H Petrov, S Kölling, P Koenraad, L Malet, S Godet, J Sietsma. Micro and Nanoscale Characterization of Complex Multilayer-Structured White Etching Layer in Rails. Met 2018;8.
4) **J Wu**, R H Petrov, M Naeimi, Z Li, R Dollevoet, J Sietsma. Laboratory simulation of martensite formation of white etching layer in rail steel. Int J Fatigue 2016;91:11–20.
5) S Li, **J Wu** , R H Petrov, Z Li, R Dollevoet, J Sietsma. "Brown etching layer": A possible new insight into the crack initiation of rolling contact fatigue in rail steels? Eng Fail Anal 2016;66:8–18.
6) R Petrov, **J Wu**, J Sietsma. Microstructure of whiteh ethcing layer of in-field loaded railway steel. Int Sci J "MACHINES Technol Mater 2017;11:453–6.
7) H K Danielsen, F G Guzman, K V Dahl, Y Li, **J Wu** , G Jacobs, R H Petrov. Multiscale characterization of White Etching Cracks (WEC) in a 100Cr6 bearing from a thrust bearing test rig. Wear 2017;370–371:73–82.
8) M Naeimi, Z Li, Z Qian, Y Zhou, **J Wu**, R Petrov, J Sietsma, R Dollevoet. Reconstruction of the rolling contact fatigue cracks in rails using X-ray computed tomography. NDT E Int 2017;92:199–212.
9) M Naeimi, S Li, Z Li, **J Wu**, R Petrov, J Sietsma, R Dollevoet. Thermomechanical analysis of the wheel-rail contact using a coupled modelling procedure. Tribol Int 2018;117:250–60
10) A Falahati, **J Wu** , P Lang, M R Ahamadi, E Povoden-Karadeniz, E Kozeschnik. Assessment of parameters for precipitation simulation of heat treatable aluminum alloys using differential scanning calorimetry. Trans Nonferrous Met Soc China 2014;24:2157–67
11) E Povoden-Karadeniz, P Lang, P Warczok, A Falahati, **J Wu** , E Kozeschnik. CALPHAD modeling of metastable phases in the Al-Mg-Si system. Calphad Comput Coupling Phase

Diagrams Thermochem 2013;43:94–104

12) Y Luo, **J Wu**, X Wu, Y Min, H Wang. Comparison on the Compositions, Microstructure and Hardness of Super Large Section Prehardened Steels for Plastic Mould Block. Adv Mater Res 2012;476–478:430–3.
13) **J Wu**, Y Min, X Wu, Q Zhou, W Xu, M Xu. Influence factors on the emergence of proeutectoid ferrite in low nickel-alloyed 718M steel[J].Transactions of Materials and Heat Treatment,2010,31(1)

B. International conferences

1) **J Wu**, R H Petrov, S Li, Z Li, S Godet, L Malet, J Sietsma. Characterization of structural change in rails surface using advance automatic crystallographic orientation microscopy. 15th Int. Conf. Railw. Eng. Des. Oper. (COMPRAIL 2016), vol. 162, Wessex Institute of Technology; 2016
2) **J Wu,** R H Petrov, L Malet, S Godeth, J Sietsma. Microstructure analysis in loaded railway steel, Poster presentation at Texture and Anisotropy symposium in Germany, 2016
3) R H Petrov, **J Wu,** L Malet, S Godeth, J Sietsma. Structural analysis of in-field loaded railway steel, oral presentation in TMS 2016 conference, USA, 2016
4) R Petrov, **J Wu**, J Sietsma. Microstructure of white etching layer of in-field loaded railway steel. Sci. Proc. XIV Int. Congr. "MACHINES. TECHNOLOGIES. Mater. 2017 - SUMMER Sess., 2017.
5) M Naeimi, Z Li, R Dollevoet, **J Wu**, R H Petrov, J Sietsma. Thermo-mechanical effects in the formation mechanism of rail squats. Civil-Comp Proc 2016;110
6) M Naeimi, Z Li, R Dollevoet, **J Wu**, R H Petrov, J Sietsma. Computation of the flash-temperature at the wheel-rail contact using a 3D finite element model and its comparison with analytical methods. C. 2015 - 10th Int. Conf. Contact Mech. Wheel / Rail Syst., 2015
7) **J Wu,** R H Petrov, M Naeimi, Z Li, J Sietsma. A Microstructural Study of Rolling Contact Fatigue in Rails. Proc. Second Int. Conf. Railw. Technol. Res. Dev. Maintenance, Ajaccio, Fr. 8-11 April 2014, Civil-Comp Press; 2014
8) E Povoden-Karadeniz, P Lang, K I Öksüz, **J Wu**, S Rafiezadeh, A Falahati, E Kozeschnik. Thermodynamics-Integrated Simulation of Precipitate Evolution in Al-Mg-Si-Alloys. Mater Sci Forum 2013;765:476–80

C. Patent

Wei-dong Dang, **Jun Wu**, Xiaochun Wu, Erxing Tu, Hongbin Wang, Yong-an Min. A method to produce large-scaled pre-hardened mold steel for plastic injection. China Patent, CN101736139B, filed Nov 26. 2009 and issued Jan 4, 2012

Acknowledgment

I would like to first thank my promotor Prof. dr. ir. Jilt Sietsma for offering me to the opportunity to work on the project. Thank you for encouraging me to perform the phase field modeling in **Chapter 6**. This thesis will be impossible without the contribution of my promotor and also the daily supervisor, Prof. dr. ir. Roumen Petrov. Roumen, thank you for guiding and inspiring me to the interesting field of EBSD, TKD, FIB, and ACOM-TEM, besides the fruitful discussions during our regular meetings.

I want to thank ProRail for starting this project. I want to especially thank Prof. dr. ir. Rolf Dollevoet for the continuous support in sharing the data and arranging access to ProRail.

This project had been carried out in close collaboration with colleagues in the faculty of Civil Engineering and Geoscience in the Delft University of Technology. During the project work, I had many interesting discussions with Prof. dr. ir. Zili Li and the Ph.D. student, Meysam Naeimi, who becomes my friend. Without their support, **Chapter 4** of this thesis, the temperature calculation in rail surface will be much more difficult. I want also to thank Prof. dr. ir. Zili Li for arranging and initializing the characterization work with his Ph.D. student, Shaoguang Li, on the brown etching layer in **Chapter 7** in this thesis.

I want to specifically thank my colleague and friend, Ankit Kumar, for his endless help with the APT data analysis and the kind arrangement during my experimental work in MPIE in Germany for my current postdoc project. Ankit, thank you also for sharing and recommending the interesting and enjoyable Indian movies.

I want to express my appreciation to Dr. M.G. Mecozzi, for the kind help in phase-field modeling. Thank you, Pina, for your patient guidance from the beginning about the concept and structure of the phase field modeling and your suggestions while I met problems. Without your contribution, **Chapter 6** should have taken me a much longer time to finalize it.

During my daily work in the department, I was able to work and talk to my dear colleagues: Qin, Alfonso, Bijna, Konstantinos, Tongky, Lie, Carola, Wei, Javier, Behnam, Ashwath, Gautam, Gao, Sepideth,

Farideh, Xiaojun, Zhiwei, Zilong. Thank you all. You make the work more interesting. Thank you, Prisca Koelman, for the kind and endless help.

The APT measurements were done at the Eindhoven University of Technology. Thanks, Dr. Sebastian Koelling for taking care of the specimen preparations and performing the measurements.

I am also registered as a joint Ph.D. student at Ghent University, Belgium. Thanks, An Verdiere for the kind introduction to TEM sample preparation using FIB and her important contribution to my current postdoc project. Thanks, Dr. F.M. Castro-Cerda for the discussion about pearlite to austenite transformation under ultrafast heating condition. Thanks, Mr. Vitaliy Bliznuk for the tutorial to the TEM facility in Ghent University and his kind help in obtaining the TEM results in **Chapter 4**.

I did some ACOM-TEM measurement on the WEL specimen in Université Libre de Bruxelles in Belgium. Thanks, Prof. Stephane Godet for allowing the collaboration and Dr. Loic Malet for assisting the data collections.

During the Ph.D. period, I also had the honor to work on a small project, relating to white etching crack in bearing steels. During the project, I had the pleasure to work with Prof. Hilmar Kjartansson Danielsen, Kristian Vinter Dahl, Hossein Alimadadi, from DTU in Denmark, Prof. Guzman, and Burghardt Gero in RWTH Aachen University in Germany, Dr. Yujiao Li and Dirk Raabe from MPIE in Germany.

I want to thank colleagues in the lab: Nico Geerlofs for performing the dilatometer measurements in **Chapter 6**; Hans Hofman for performing the Gleeble test in **Chapter 5**; Richard Huizenga for performing and analyzing the XRD data; Frans Bosman and Jurriaan van Slingerland for allowing me to use their sawing machine to cut the rail pieces for laboratory tests; Kees Kwakernaak for the support during my SEM work.

After finishing my Ph.D., I started my postdoc in the same department. Thank Bosch Transmission Technology BV and M2i for funding the project. Thanks, Duc Tran, Bert Pennings and Michel Derks from Bosch for their constant support.

Last, but not the least important, I want to thank my wife, Jie Zhang. You even quit your job in China to join me, firstly in Austria, and later in the Netherlands. Your laughter and the amazing cuisine soothe the pressure from the work and energize me. Without your love, constant support and encouragement, my pursuit will not become true.